Did galaxies reionize the universe?

Thesis by

Matthew A. Schenker

In Partial Fulfillment of the Requirements

for the Degree of

Doctor of Philosophy

California Institute of Technology

Pasadena, California

2015

(Defended June 18, 2014)

Acknowledgments

The past 5 years of graduate studies at Caltech have easily been both the most challenging, but also most fulfilling years of my life. I consider myself fortunate to have worked with my thesis advisor, Richard Ellis; for the last four of them after I discovered how tedious CMB cosmology in the lab can be. Studying under Richard has truly been a pleasure, and I have regularly told colleagues that I could hardly imagine a better advisor. Richard's passion for science and his work ethic are contagious, and I am sure that my thesis would not be half as good without his constant drive to uncover the truth. I'm also thankful that I can consider him a mentor, as well as a good friend.

Thanks to the others that have played the role of advisor during my time in graduate school: Brant Robertson, Dan Stark, and Andrew Lange. Whether it was a late night whiteboard session or watching Youtube clips of Rocky IV for inspiration, I never stopped learning while around these people. Chuck Stiedel, Nick Scoville, Gregg Hallinan, and Phil Hopkins are also owed gratitude for serving on my defense committee. It was a pleasure to share my years of research with such excellent scientists.

Of course, I never could have made it through five years without the support of the astronomy graduate student community. Thanks to Ryan and Sam (and Thinh) for putting up with me as a roommate and driving my carless self around LA for my first year and a half here. Gwen and Drew for always having us over for cultured events. Sirio for always having someone to rile up during an argument. Trevor for always having someone to discuss various circlon theories of physics with. Tucker for his companionship in outdoor adventure. Ben and Brandon for having friends to discuss the latest trends in credit card points and airline miles with (in addition to Richard, of course). Finally, thanks to Jason, Kat, Alex, Brian, Anna, Luke, and Brandon for all those 4 AM departures to Mammoth and the Sierra backcountry.

The support staff at Caltech has been truly phonemonal. I'm sure my computer would be smashed to pieces during a fit of rage many times over were it not for the help of Anu, Patrick, and Jose. Judy, Gita, and Gina helped my time here run as smoothly as possible. I'm also unbelievaly grateful for the hard work from the Keck crew, particularly Mark Kassis and Jim Lyke, who helped keep the instruments in top shape while observing.

Finally, I'd like to give thanks to Angie, Rob, and Amy for always supporting me in my academic

endeavors, even when they moved me to the other end of the country for the better part of a decade.

Abstract

The epoch of reionization remains one of the last uncharted eras of cosmic history, yet this time is of crucial importance, encompassing the formation of both the first galaxies and the first metals in the universe. In this thesis, I present four related projects that both characterize the abundance and properties of these first galaxies and uses follow-up observations of these galaxies to achieve one of the first observations of the neutral fraction of the intergalactic medium during the heart of the reionization era.

First, we present the results of a spectroscopic survey using the Keck telescopes targeting $6.3 < z < 8.8$ star-forming galaxies. We secured observations of 19 candidates, initially selected by applying the Lyman break technique to infrared imaging data from the Wide Field Camera 3 (WFC3) onboard the Hubble Space Telescope (HST). This survey builds upon earlier work from Stark et al. (2010, 2011), which showed that star-forming galaxies at $3 < z < 6$, when the universe was highly ionized, displayed a significant increase in strong Lyman alpha emission with redshift. Our work uses the LRIS and NIRSPEC instruments to search for Lyman alpha emission in candidates at a greater redshift in the observed near-infrared, in order to discern if this evolution continues, or is quenched by an increase in the neutral fraction of the intergalactic medium. Our spectroscopic observations typically reach a 5σ limiting sensitivity of < 50Å. Despite expecting to detect Lyman alpha at 5σ in 7-8 galaxies based on our Monte Carlo simulations, we only achieve secure detections in two of 19 sources. Combining these results with a similar sample of 7 galaxies from Fontana et al. (2010), we determine that these few detections would only occur in $< 1\%$ of simulations if the intrinsic distribution was the same as that at $z \sim 6$. We consider other explanations for this decline, but find the most convincing explanation to be an increase in the neutral fraction of the intergalactic medium. Using theoretical models, we infer a neutral fraction of $x_{HI} \simeq 0.44$ at $z = 7$.

Second, we characterize the abundance of star-forming galaxies at $z > 6.5$ again using WFC3 onboard the HST. This project conducted a detailed search for candidates both in the Hubble Ultra Deep Field as well as a number of additional wider Hubble Space Telescope surveys to construct luminosity functions at both $z \sim 7$ and 8, reaching 0.65 and 0.25 mag fainter than any previous surveys, respectively. With this increased depth, we achieve some of the most robust constraints on the Schechter function faint end slopes at these redshifts, finding very steep values of $\alpha_{z\sim7} =$

$-1.87^{+0.18}_{-0.17}$ and $\alpha_{z\sim8} = -1.94^{+0.21}_{-0.24}$. We discuss these results in the context of cosmic reionization, and show that given reasonable assumptions about the ionizing spectra and escape fraction of ionizing photons, only half the photons needed to maintain reionization are provided by currently observable galaxies at $z \sim 7-8$. We show that an extension of the luminosity function down to $M_{\rm UV}= -13.0$, coupled with a low level of star-formation out to higher redshift, can fit all available constraints on the ionization history of the universe.

Third, we investigate the strength of nebular emission in $3 < z < 5$ star-forming galaxies. We begin by using the Infrared Array Camera (IRAC) onboard the Spitzer Space Telescope to investigate the strength of Hα emission in a sample of $3.8 < z < 5.0$ spectroscopically confirmed galaxies. We then conduct near-infrared observations of star-forming galaxies at $3 < z < 3.8$ to investigate the strength of the [OIII] 4959/5007 and Hβ emission lines from the ground using MOSFIRE. In both cases, we uncover near-ubiquitous strong nebular emission, and find excellent agreement between the fluxes derived using the separate methods. For a subset of 9 objects in our MOSFIRE sample that have secure Spitzer IRAC detections, we compare the emission line flux derived from the excess in the K_s band photometry to that derived from direct spectroscopy and find 7 to agree within a factor of 1.6, with only one catastrophic outlier. Finally, for a different subset for which we also have DEIMOS rest-UV spectroscopy, we compare the relative velocities of Lyman alpha and the rest-optical nebular lines which should trace the cites of star-formation. We find a median velocity offset of only $v_{Ly\alpha} = 149$ km s^{-1}, significantly less than the 400 km s^{-1} observed for star-forming galaxies with weaker Lyman alpha emission at $z = 2-3$ (Steidel et al. 2010), and show that this decrease can be explained by a decrease in the neutral hydrogen column density covering the galaxy. We discuss how this will imply a lower neutral fraction for a given observed extinction of Lyman alpha when its visibility is used to probe the ionization state of the intergalactic medium.

Finally, we utilize the recent CANDELS wide-field, infra-red photometry over the GOODS-N and S fields to re-analyze the use of Lyman alpha emission to evaluate the neutrality of the intergalactic medium. With this new data, we derive accurate ultraviolet spectral slopes for a sample of 468 $3 < z < 6$ star-forming galaxies, already observed in the rest-UV with the Keck spectroscopic survey (Stark et al. 2010). We use a Bayesian fitting method which accurately accounts for contamination and obscuration by skylines to derive a relationship between the UV-slope of a galaxy and its intrinsic Lyman alpha equivalent width probability distribution. We then apply this data to spectroscopic surveys during the reionization era, including our own, to accurately interpret the drop in observed Lyman alpha emission. From our most recent such MOSFIRE survey, we also present evidence for the most distant galaxy confirmed through emission line spectroscopy at $z = 7.62$, as well as a first detection of the CIII]1907/1909 doublet at $z > 7$

We conclude the thesis by exploring future prospects and summarizing the results of Robertson et al. (2013). This work synthesizes many of the measurements in this thesis, along with external

constraints, to create a model of reionization that fits nearly all available constraints.

Contents

List of Figures

List of Tables

Statement of Originality

Sections of this thesis have been previously published as Schenker, M. A., Stark, D. P., Ellis, R. S., et al. 2012, ApJ, 744, 179 (Chapter 2), Schenker, M. A., Robertson, B. E., Ellis, R. S., et al. 2013, ApJ, 768, 196 (Chapter 3), Stark, D. P., Schenker, M. A., Ellis, R., et al. 2013a, ApJ, 763, 129 and Schenker, M. A., Ellis, R. S., Konidaris, N. P., & Stark, D. P. 2013a, ApJ, 777, 67 (Chapter 4), and Robertson, B. E., Furlanetto, S. R., Schneider, E., et al. including M.A. Schenker 2013, ApJ, 768, 71 (Section 6.2). The majority of the work presented in Chapter 5 has been submitted to *The Astrophysical Journal* as Schenker et al. (2014), while Section 5.6 will appear in an additional forthcoming paper (Stark et al., in preparation).

The work presented here has been a collaborative effort with significant contributions from numerous colleagues, described here. Ross McLure assisted with target selection in the ERS, HUDF, and EGS fields for the observations in Chapter 2. In Chapter 3, Brant Robertson implemented the fitting procedures for both the stepwise and Schechter luminosity functions, including accurate estimates of the errors due to cosmic variance. Dan Stark conducted the actual SED fitting and estimates of the characteristic Hα strength in Section 4.2, while I provided the nebular emission models using code modified from Brant Robertson's. Dan Stark also provided the revised stellar mass estimates detailed in Section 4.4.4, and conducted the majority of the DEIMOS observations and data reduction on which Chapter 5 is based. Finally, Brant Robertson constructed the reionization model presented in Section 6.2, based partly upon my results in Chapter 3.

Chapter 1

Introduction

Remarkably, our knowledge of the physical state of the universe in its earliest moments remains much more complete than that of the subsequent billion years. Until 380,000 years after the big bang, free electrons, nuclei, and photons were coupled to one another and smoothly spread throughout the universe along with an underlying distribution of dark matter. Once the universe had cooled enough that nuclei and electrons were able to recombine, the mean free path of photons dramatically increased. We observe this free streaming of photons today as the cosmic microwave background (CMB), and it is this decoupling of baryons and photons that also finally permitted baryonic structures to grow. Overdensities of dark matter, imprinted from primordial quantum fluctuations, provided the scaffolding upon which baryonic matter subsequently accreted. These collapsed structures, or halos, continued to grow, and by a redshift of perhaps $z \sim 20 - 30$ (100-200 Myr after the big bang), the largest had grown hot enough to radiate energy through molecular hydrogen. With the new-found ability for these baryonic structures to cool and therefore further collapse, the first stars then formed (Bromm 2013). Throughout the subsequent 800 Myr, these structures grew through both mergers and further accretion, eventually producing enough energetic photons to reionize the vast majority of the hydrogen gas that lay between galaxies in the intergalactic medium (IGM).

Although the hunt to find these first stars and galaxies continues, technical and observational breakthroughs in the preceding two decades have transformed our knowledge of galaxy formation and evolution in the first 2 billion years. Prior to the pioneering work of Steidel et al. (1995), there existed no functional method to detect "normal" star-forming galaxies in this era. Today, we have the first useful constraints on the star-formation rate density of the universe out to $z \sim 10$ (Ellis et al. 2013; Oesch et al. 2014), only 500 Myr after the big bang. Independent lines of evidence also now imply that reionization concluded at a redshift of $z \sim 6.5$ (e.g., Fan et al. 2006; Bolton et al. 2011; Konno et al. 2014).

However, despite this progress, we are still left with many questions regarding the early universe. Was reionization a gradual process, drawn out over hundreds of millions of years, or did it rapidly transform the IGM? Are there enough faint galaxies to provide the necessary ionizing photons to

drive this phase transition? How well do we really understand the properties of the high-redshift galaxies we discover? These are the questions that I have sought to answer over the previous five years at Caltech and in this thesis. In the following sections, I provide historical overviews of both the searches and characterization of high-redshift galaxies as well as measurements of reionization, concluding each with a summary of present day knowledge.

1.1 Star-forming galaxies

Dating back to the beginning of extragalactic astronomy with pioneering observations by Vesto Slipher and Edwin Hubble in the early 20th century, astronomers have been keenly interested in the study of distant galaxies. With the discovery of the CMB, and the firm establishment of big bang cosmology, these searches took on an even more important goal. By predicting that all matter in the universe originated at a single point in time, to understand conditions earlier in the universe, it was simply necessary to discover yet more distant objects. Indeed, the quasars discovered at cosmological distances by Schmidt (1965) provided our first glimpse at early structure formation in the universe and the intergalactic conditions at that time. The hunt for "normal" star-forming galaxies proved much more difficult.

From 1960 through the mid 1980s, the most distant confirmed galaxies were discovered almost exclusively as intense radio sources from the Cambridge 3C survey (Edge et al. 1959). While these sources helped to push back our redshift frontier, given the presence of an active galactic nucleus which leads to a luminous radio source, they could not be used to construct any kind of characteristic sample. The lack of detection of a population of distant star-forming galaxies without these central engines, however, was not for lack of trying.

Early work by Partridge & Peebles (1967) suggested that the rest-UV continuum and the Lyα emission line could be useful signposts for the discovery of primeval galaxies, with up to $\sim 6-7\%$ of the total flux emerging through Lyα emission. Subsequent attempts to discover these objects using direct detection through photographic plates (Partridge 1974) and fluctuations in the far-optical sky background measured through photometers (Davis & Wilkinson 1974) unfortunately proved unsuccessful.

Kron (1980) later carried out a comprehensive search using photometric plates which identified a population of dim blue galaxies that became systematically bluer with increasing faintness. Subsequent modelling using synthetic spectra and comparison of cosmological models with the observed color-magnitude relation indicated that at $B > 23$, a significant component of the galaxies, may be located at $z > 1$ and perhaps even further (Bruzual A. & Kron 1980; Tinsley 1980). Such conclusions would later be confirmed using K-corrections updated with the latest UV data in King & Ellis (1985). In the closed universe models that were currently favored, this corresponded to a time more

than halfway back to the beginning of the universe, making these excellent candidates for primeval galaxies.

The advent of CCDs in the 1980s brought even deeper surveys that confirmed this abundance of faint blue galaxies (Hall & Mackay 1984; Tyson 1988), as well as studies of infrared colors of brighter galaxies that pointed toward increased star formation at $z > 0.5$ (Ellis & Allen 1983). However, the distance of these could not be thoroughly investigated until the advent of multiobject spectrographs. The necessary samples were finally built up with FOCAP, LDSS, and Autofib at the Anglo Australian Telescope (Broadhurst et al. 1988; Colless et al. 1990; Ellis et al. 1996), as well as LDSS-2 on the William Hershel Telescope (Glazebrook et al. 1995). Unfortunately, these surveys found that the large majority of the faint blue galaxy population lay at $z < 1$, and did not consist of the $z > 2$ primordial galaxies initially expected (Colless et al. 1993; Ellis et al. 1996).

Narrowband searches for the Lyα emission line were also undertaken, but also had difficulty locating these early galaxies. Djorgovski et al. (1985) initially reported the discovery of a galaxy through Lyα emission nearby a $z \sim 3.2$ quasar. The authors imaged the field in both a narrowband filter at the expected wavelength of Lyα and a broadband filter longward of this wavelength, in order to distinguish objects with an excess in the narrowband, and thus strong Lyα emission. Unfortunately, this object was later found to be yet another active galactic nucleus through follow-up spectroscopy, but the path to discovery of these objects (known as Lyman alpha emitters, or LAEs) had been paved.

Attempts to recover primeval galaxies continued this technique in the coming years through further narrowband imaging (e.g., Pritchet & Hartwick 1987, 1990), slitless spectroscopy (Crampton et al. 1987), and longslit spectroscopy (Lowenthal et al. 1990), but were met with little success. Indeed, the first LAEs at $z > 3$ would not be discovered until the successful survey of Cowie & Hu (1998) at $z \sim 3.4$.

However, the breakthrough to open the door to discovery of star-forming, but otherwise normal, galaxies at high redshift was achieved by Chuck Steidel and collaborators with the successful application of the Lyman break technique (Steidel et al. 1995, 1996). This observational method used a custom set of broadband filters designed to identify the sharp cutoff in flux below the 912 Å Lyman limit in the rest frame of distant galaxies, due to both a combination of opacity in stellar atmospheres themselves and residual HI in the intergalactic medium. Spectroscopic follow-up observations of these galaxies with the Keck telescope then proved incredibly effective, with upwards of 70% confirmed to lie at $z \geq 3$ (Steidel et al. 1996).

In the years that followed, this photometric selection technique was generalized to search for star-forming galaxies at higher redshifts, with early searches at $z \sim 4$ in the Hubble Deep Field (Madau et al. 1996) and various other blank fields (Steidel et al. 1999). The installation of the Advanced Camera for Surveys (ACS) on the Hubble Space Telescope in 2002 brought about the

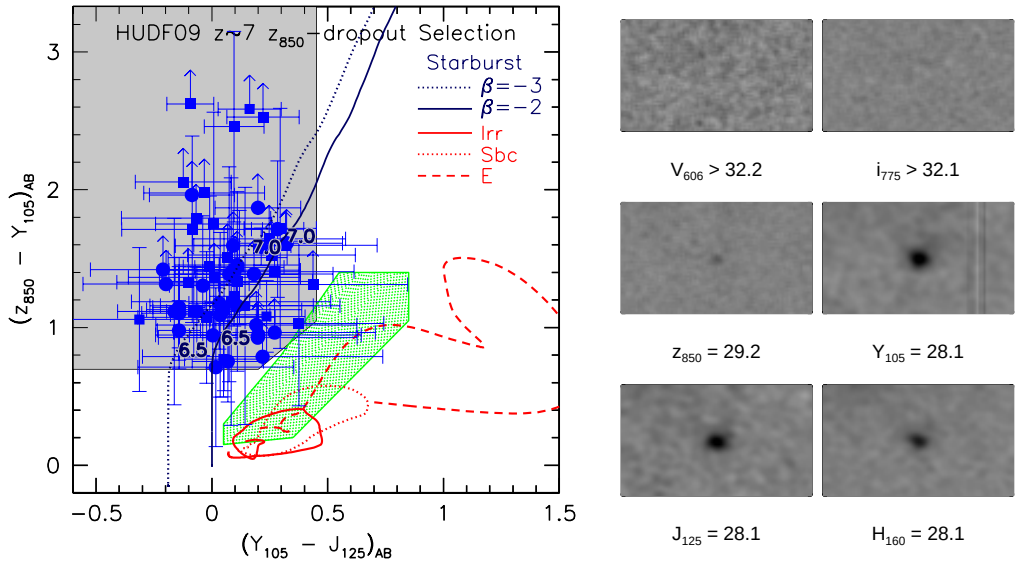

Figure 1.1 Demonstration of the color-color method used to select high-redshift star-forming galaxies pioneered by Steidel et al. (1995). Left: Demonstration of the technique at $z \sim 7$ in the HUDF from Bouwens et al. (2011). Vertical axis denotes the amplitude of the targeted spectral break, while the horizontal axis displays the color just longward of the break. $z \sim 7$ galaxies are selected in the grey region, where the break amplitude is large ($z_{850} - Y_{105} \geq 0.75$), and the color longward is only moderately red ($Y_{105} - J_{125} \leq 0.45$). In addition, all candidates have fluxes below the 2σ limits in all shorter wavelength filters. Blue data points denote high-redshift galaxies selected from the HUDF09, while black dotted and solid lines show evolution in the color-color plane with redshift for model spectra. Red lines and green region denote locations of potential low redshift contaminants. Right: Cutout of $z \sim 7$ galaxy from our HUDF12 campaign, discussed in Chapter 3, which also passes the selection criteria shown at left.

next breakthrough. Progress came from both the wide-area $320'^2$ GOODS fields (e.g., Giavalisco et al. 2004; Dickinson et al. 2004) and the $11'^2$ Hubble Ultra Deep Field (e.g., Bunker et al. 2004; Beckwith et al. 2006; Coe et al. 2006), both of which uncovered Lyman break galaxies out to $z \sim 6$. As before, spectroscopic follow-up of these candidates found that the majority of these populations indeed reside at high redshift (Bunker et al. 2003; Stanway et al. 2004; Stark et al. 2010).

With the discovery of such distant populations, an understanding of the evolution of galaxies in this early time began to come about. As at lower redshift, the UV-selected galaxy luminosity function closely resembles that originally proposed by Schechter (1976), with an exponential dropoff above a given brightness and a power law growth in the number density of galaxies below this brightness. The total star-formation rate density of the universe, as shown in Figure 1.2, was seen to steadily decline from its peak at $z \sim 2-3$ out to $z \sim 6$. Bouwens et al. (2007) showed that this decline was largely caused by a decrease in the characteristic luminosity with redshift, while the faint end slope remained consistent with $\alpha \sim -1.7$ between redshifts 3 and 6.

However, as the Hubble Space Telescope can only probe the rest-UV spectrum of these galaxies, it is primarily sensitive to the youngest and hottest stars, which comprise only a small component of a galaxy's stellar mass for any allowed initial mass function (Salpeter 1955; Kroupa 2001; Chabrier 2003). To effectively measure the stellar mass of these galaxies requires photometry that measures the rest-frame optical or longer wavelengths at which more numerous, low-mass stars output the majority of their light. Despite a primary mirror just 0.85 m in diameter, the Spitzer Space Telescope has excelled in providing these crucial measurements. Spitzer's Infrared Array Camera (IRAC) has enabled ultradeep exposures centered at 3.6 and 4.5 μm capable of providing stellar masses for individual galaxies out to $z \sim 6$, and now even beyond.

Initial measurements showed that even out to $z \sim 6$, many UV-luminous galaxies displayed strikingly red UV to optical colors, with observed breaks as great as ~ 1 mag. This was taken to indicate that these galaxies were both extremely massive, with $M_* \sim 10^{10} M_\odot$, and had ages ≥ 100 Myr at a time when then universe was less than 1 Gyr old (e.g., Eyles et al. 2005; Labbé et al. 2006). However, more careful work soon noted that as the observed equivalent width of an emission line increases with redshift, rest frame optical emission lines including Hα and [OIII] could be responsible for a significant fraction of the measured flux in the Spitzer bandpass (Schaerer & de Barros 2009). As we shall show in Chapter 4, however, Spitzer plays a valuable role in constrain the observed strength of these rest-optical emission lines. With the use of a carefully chosen spectroscopic sample, it is capable of both deriving both broadband photometric corrections for emission lines, and an estimate of the stellar mass density at high redshift. We note that even with our derived corrections, the stellar masses of $z \sim 6$ galaxies remain large enough ($M_* \sim 4 \times 10^9 M_\odot$ at $M_{UV} \sim -21$) to imply significant star formation at earlier times.

The new Wide Field Camera 3 infrared camera (WFC3) onboard HST has recently provided

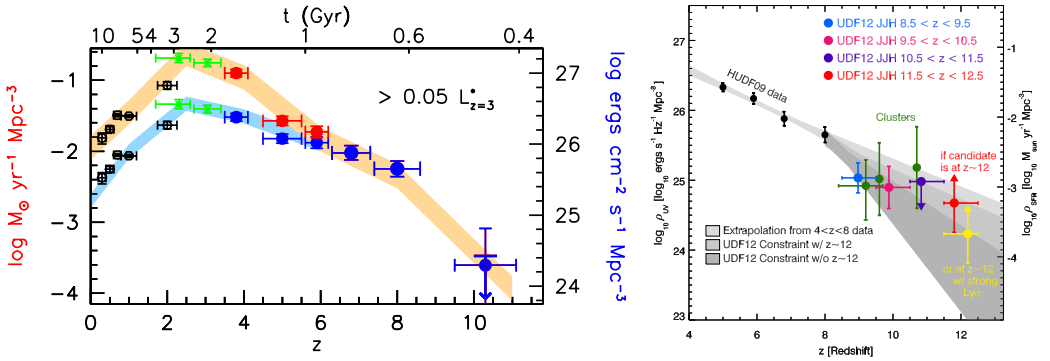

Figure 1.2 Left: Star-formation rate density vs. redshift adopted from Bouwens et al. (2011). Black data at $z < 2$ are from Schiminovich et al. (2005), green at $2 < z < 3$ from Reddy & Steidel (2009), with the remaining from Bouwens et al. (2007) and Bouwens et al. (2011). The upper data highlighted by the red curve includes a correction for star-formation obscured by dust, while the lower curve simply uses the star-formation rates derived from the UV continuum. There exists a clear peak in the cosmic star-formation rate density at $z \sim 2-3$, and a gradual drop-off toward higher redshift. Right: SFRD plotted against redshift at $z > 4$ showing the measurements from the UDF12 campaign out to $z \sim 12$. Adopted from Ellis et al. (2013).

a similar advance in our knowledge of star-forming galaxies at $z > 7$ as the ACS provided at $3 < z < 6$. With an increase in survey efficiency of $\sim$ 40x compared to the previous HST infrared camera, NICMOS, the field went from a handful of credible $z > 7$ candidates (Bouwens et al. 2008) to hundreds (e.g., McLure et al. 2010; Bouwens et al. 2011; Yan et al. 2011; Finkelstein et al. 2011). Simultaneously, advances in infrared detectors on the ground and large surveys have begun to provide robust measurements of the abundance of bright $z \sim 7$ Lyman break galaxies (e.g., Ouchi et al. 2010; Castellano et al. 2010; Bowler et al. 2012).

With these observations, luminosity functions have been constructed out to $z \sim 8$, and even rough measurements of the star-formation rate density out to $z \sim 12$. At the bright end, where observations come from wide area, ground-based surveys, it remains unclear whether the abundance follows a double power law form, indicating that feedback may not yet be in place at $z \sim 7$ (Bowler et al. 2014), or the characteristic exponential dropoff of the Schechter function (Ouchi et al. 2009; Castellano et al. 2010). At the faint end, where the majority of the UV luminosity density arises, there is no evidence for any departure from a power law slope. Before this thesis, measurements of the faint end slope were very unclear. Although there existed marginal evidence for a steepening of this slope from the -1.7 observed at $3 < z < 6$, Bouwens et al. (2012a) estimated that the measured uncertainty on the $z \sim 7$ slope in 2011 resulted in an uncertainty of $\sim 6\times$ in the integrated UV luminosity density. In order to understand the capability of galaxies to reionize the universe, an accurate measurement of this slope is crucial.

There is now great insight into the properties of these galaxies as well. The typical source at $z \geq 7$ is physically small, with a half-light radius $r \sim 0.35$ kpc, comparable to the sizes of giant

molecular associations in local star-forming galaxies (Ono et al. 2013). Much effort has been put in over the last few years to accurately measure the ultraviolet spectral slopes of these galaxies, parameterized as $f_\lambda \propto \lambda^\beta$, by comparing the fluxes measured in different WFC3 filters. Despite early claims of extremely young, metal-poor populations (Bouwens et al. 2010b), a general consensus has emerged that faint $z \sim 7$ galaxies have moderately blue slopes, with $\beta \sim -2.0$ to -2.3 (e.g., Finkelstein et al. 2012b; Bouwens et al. 2012b). These measurements are consistent with either solar metallicity populations with zero reddening, or moderately sub solar ($Z = 0.1 - 0.2 Z_\odot$) populations with moderate reddening (Dunlop et al. 2012). However, an added uncertainty is the source of this reddening; although dust within the galaxy is a likely origin, the reprocessing of ionizing photons into nebular continuum emission by hydrogen, if strong enough, can have a similar effect (Robertson 2010b).

1.2 Reionization

We now shift our focus from the galaxies to their influence on the surrounding IGM. As we previously noted, in the mid 1960s the near concurrent discoveries of primordial radiation from the cosmic microwave background (Penzias & Wilson 1965) and the first quasars (Schmidt 1965) revolutionized our view of the universe and provided unambiguous evidence in support of the big bang theory. Shortly afterward, Gunn & Peterson (1965) realized that a measurement of the spectrum shortward of the observed wavelength of Lyα could yield an estimate or upper limit on the neutral hydrogen density, x_{HI}, in the vicinity of the quasars and provide a first glimpse of the ionization history of the universe. At the time, the authors expected to uncover a large quantity of neutral hydrogen, which would provide the needed cosmic density to decelerate the universe. Instead, they discovered only an upper limit of $n_{HI} < 6 \times 10^{-11}$ atoms cm^{-3}, equivalent to 1 part in 10^5 of the required critical density. Interestingly, the authors assumed that a majority of the remaining matter was in the form of ionized hydrogen, with free-free emission from the intergalactic medium itself, and not star-forming galaxies, as the most likely source of ionization.

Since this first measurement, quasar spectroscopy has remained one of the most valuable probes for the ionization state of the IGM across its history. Steidel & Sargent (1987) provided an updated measurement of the Gunn-Peterson limit using a statistical study of the Lyα forest in high-resolution spectra of quasars. Because the Lyα forest is composed of many discrete clumps of neutral Hydrogen, it becomes difficult to directly measure the true continuum flux level originating from the quasar. Instead, Steidel & Sargent (1987) obtained spectra of moderate resolution with significant wavelength coverage longward of Lyα, which were then extrapolated to provide an estimate of the intrinsic continuum shortward. This resulted in a limit of $\tau_{GP} < 0.05$ at $z = 2.64$. Converting to a neutral fraction in the diffuse IGM using present day cosmology, this yields $x_{HI} < 3 \times 10^{-7}$.

In the following years, progress pushing out the known boundary of the ionized IGM continued using quasar spectroscopy, but the first evidence for a neutral IGM would not come until much later. Webb et al. (1992) infer a limit of $\tau_{GP} < 0.04$ at $z = 4.11$ through quasar spectroscopy and a similar extrapolation to that used in Steidel & Sargent (1987). The advent of the Sloan Digital Sky Survey (SDSS) allowed this technique to be pushed out even further. Songaila et al. (1999) and Fan et al. (2000) both report upper limits on the Gunn-Peterson optical depth of $\tau_{GP} < 0.1$ and 0.4, at $z \sim 5$ and 5.7, respectively, by measuring the continuum level between gaps in the Lyα forest. However, even these results still only traced neutral fractions in the diffuse IGM of $x_{HI} \ll 10^{-4}$.

The first substantial evidence for an uptick in the neutral hydrogen content of the universe came with the discovery of a complete Gunn-Peterson trough in the spectrum of a $z = 6.28$ quasar (Becker et al. 2001; Fan et al. 2001). More convincing evidence came from Fan et al. (2006), who used spectra of 19 quasars from SDSS to measure the evolution of the Gunn-Peterson optical depth, and thus neutral hydrogen fraction between $5.0 < z < 6.2$. They found a strong lower limit of $x_{HI} > 5 \times 10^{-4}$, nearly an order of magnitude greater than the fraction at $z \sim 5$. However, with such a strong increase in the optical depth, it has become impractical to expose any deeper with current facilities in order to further push up the lower limit of these measurements, thus requiring new techniques to continue to use this spectroscopy to probe IGM ionization.

One such promising measurement recently arose through the first discovery of a $z > 7$ quasar by Mortlock et al. (2011). As the Gunn-Peterson optical depth has already saturated at these redshifts, Bolton et al. (2011) used measurements of the Lyα damping wing and radiative transfer simulations to infer a neutral fraction of $x_{HI} > 0.1$. However, there are numerous drawbacks. The measurement only takes place along a single sightline, and could also be due to a damped Lyα system in close proximity to the quasar, which would obviate the need for such a large neutral fraction. To make further progress, a much larger sample of $z > 7$ quasars is needed.

1.2.1 Cosmic Microwave Background

In the era of precision cosmology, observations of the cosmic microwave background are also able to give us details about the epoch of reionization, as a small fraction of these photons are scattered between their emission at $z \simeq 1100$ and their observation. As charged free electrons are much more readily able to interact with microwave photons than neutral hydrogen through Thomson scattering, their presence is able to imprint a distinct signature on the CMB.

Most prominently, this scattering imparts a large-scale linear polarization signal through transforming the CMB temperature spectrum's quadrupole anisotropy, as first noticed by Rees (1968). To obtain a measurement of the Thomson optical depth, τ_e, and thus a measurement of the integrated path length through an ionized intergalactic medium, this measurement is combined with temperature data, as the optical depth is degenerate with the amplitude of the temperature anisotropy.

WMAP has provided measurements of this polarization signal, which can then be translated to an estimate for the redshift of reionization if it proceeded instantaneously, with the 9-year results indicating a redshift of $z_{reion} = 10.5 \pm 1.1$ (Hinshaw et al. 2013). However, since τ_e represents an integral measurement, if early star-formation maintains a low level of ionization, the 50% reionization redshift will be pushed further toward the present day (Fukugita & Kawasaki 2003). To disentangle this, there remain higher order statistics available in the large-scale polarization data, and Kaplinghat et al. (2003) showed that Planck measurements of the complete power spectrum may be able to discriminate between different reionization histories with the same optical depth.

In addition to polarization on large scales, temperature anisotropy measurements on small scales will also provide some insight into reionization. During reionization, the kinetic Sunyaev-Zel'dovich effect, or scattering of photons off of large-scale coherent velocity flows, can impart an imprint on the observed CMB. Although scatterings from gas falling into one side of a potential well are generally offset by scatterings from the opposite side, a patchy ionization structure in a partially neutral IGM will modulate this (Gruzinov & Hu 1998). McQuinn et al. (2005) show that the amplitude of these features in the CMB power spectrum is strongly dependent upon the duration of the patchy phase of reionization, providing a complementary measurement to the Thomson optical depth. Recent measurements from the SPT have claimed an upper limit of $\Delta z_{reion} < 7.2$ from searches for this effect on small scales (Zahn et al. 2012).

1.3 Goals of the thesis

Having outlined the territory, I now provide a brief introduction to the two main objectives of this thesis. Firstly, I have sought to provide a more comprehensive picture of the latter stages of reionization. Quasar spectroscopy has shown that the neutral fraction of the IGM increases sharply at $z > 6.0$, but these spectra are insensitive to $x_{HI} \gtrsim 10^{-3}$. To this end, we undertook a Keck survey designed to measure the ionization state of the IGM at $z \sim 7$ using star-forming galaxies themselves, the results of which are presented in Chapter 2. This work builds upon earlier spectroscopy of Lyman break galaxies at $4 < z < 6$, which showed that the incidence of strong Lyα emission, particularly among UV faint galaxies, steadily increases with increasing redshift. By searching for this emission in deep spectroscopic exposures at $z \geq 6.5$, we were thus able to probe the IGM neutrality at this time, as any increase in the presence of neutral gas can significantly decrease the visibility of Lyα. To create a quantitative prediction for the incidence of Lyα emission we expected to observe, we binned the control sample as a function of UV magnitude and redshift and extrapolated these trends.

This aim is continued with an updated application of the technique in Chapter 5. To improve our predictive model for Lyα emission, we make use of the new CANDELS infrared photometry to measure accurate UV slopes for our baseline $3 < z < 6$ sample, and use this as the basis for

the number of detections we expect at $z \geq 6.5$. This method has the advantage of being more physically based, as the UV slope represents a combination of the stellar population, age, and dust content, each of which are directly related to Lyα production and/or escape. This new methodology is presented in conjunction with a new MOSFIRE survey targeting Lyα emission at $z \sim 8$. Together with data from the literature, we update our earlier measurement at $z \sim 7$, and provide evidence for further evolution at $z \sim 8$.

The second component of this thesis seeks to determine whether star-forming galaxies themselves are able to drive the reionization process. As mentioned previously, a key quantity for answering this question is the faint end slope of the $z \geq 7$ Schechter UV luminosity function, as we are now confident that the necessary photons cannot arrive from the luminous ($L \simeq L_*$) galaxies alone (Bouwens et al. 2012a; Finkelstein et al. 2012a). Chapter 3 presents one of the key results from the UDF12 HST project (GO: 12498, PI: R. Ellis), which approximately doubled the near-infrared exposure time in the Hubble Ultra Deep Field and significantly expanded our view of $z \geq 7$ star-forming galaxies. I detail here the deepest measurement to date of the $z \sim 7$ and 8 UV luminosity functions, extending $\sim 0.65(0.15)$ mag deeper at $z \sim 7(8)$ than previous estimates, and providing evidence for evolution in the faint end slope.

In addition to directly probing early star-formation, I have also focused on obtaining an accurate measurement of the high-redshift stellar mass density, which provides a valuable integral constraint on prior activity. A complication arises from simply fitting SEDs to the rest-optical fluxes due to the possibility that the measured broadband filters may be contaminated by strong nebular emission lines. In Chapter 4, I detail our efforts to constrain the strength of these emission lines using carefully selected spectroscopic samples. We first achieve this by using a spectroscopic sample of galaxies chosen to lie between $3.8 < z < 5.0$, where the Hα line falls in the short wavelength Spitzer IRAC filter, while the adjacent photometric filters are free from strong lines. From this, we are able to derive the characteristic Hα equivalent width solely thorough broadband photometry and a spectroscopic redshift. We then attempt to verify this strength using direct spectroscopy from the ground at the highest redshifts possible ($3 < z < 3.8$) using the new multi-object infrared spectrograph MOSFIRE. In this range, [OIII] and Hβ fall into the K-band, allowing us to directly compare SED-derived and directly observed line fluxes and evaluate our earlier technique. These results then synthesized in Chapter 6 with a review of Robertson et al. (2013), and a look to future studies of the high redshift universe.

Chapter 2

A first measurement of X_{HI} using Lyman Break Galaxies

Abstract

Using deep Keck spectroscopy of Lyman break galaxies selected from infrared imaging data taken with the Wide Field Camera 3 onboard the Hubble Space Telescope, we present new evidence for a reversal in the redshift-dependent fraction of star forming galaxies with detectable Lyman alpha (Lyα) emission in the redshift range $6.3 < z < 8.8$. Our earlier surveys with the DEIMOS spectrograph demonstrated a significant increase with redshift in the fraction of line emitting galaxies over the interval $4 < z < 6$, particularly for intrinsically faint systems which dominate the luminosity density. Using the longer wavelength sensitivities of LRIS and NIRSPEC, we have targeted 19 Lyman break galaxies selected using recent WFC3/IR data whose photometric redshifts are in the range $6.3 < z < 8.8$ and which span a wide range of intrinsic luminosities. Our spectroscopic exposures typically reach a 5σ sensitivity of < 50 Å for the rest-frame equivalent width (EW) of Lyα emission. Despite the high fraction of emitters seen only a few hundred million years later, we find only 2 convincing and 1 possible line emitter in our more distant sample. Combining with published data on a further 7 sources obtained using FORS2 on the ESO VLT, and assuming continuity in the trends found at lower redshift, we discuss the significance of this apparent reversal in the redshift-dependent Lyα fraction in the context of our range in continuum luminosity. Assuming all the targeted sources are at their photometric redshift and our assumptions about the Lyα EW distribution are correct, we would expect to find so few emitters in less than 1% of the realizations drawn from our lower redshift samples. Our new results provide further support for the suggestion that, at the redshifts now being probed spectroscopically, we are entering the era where the intergalactic medium is partially neutral. With the arrival of more sensitive multi-slit infrared spectrographs, the prospects for improving the statistical validity of this result are promising.

2.1 Introduction

Determining when neutral hydrogen in the intergalactic medium (IGM) was reionized is an important question in observational cosmology and a precursor to understanding whether star forming galaxies provided the necessary UV photons (Robertson 2010b). One of the most practical probes of reionization with current facilities utilizes the frequency of occurrence of Lyα emission in star forming galaxies. As Lyα photons are resonantly scattered by neutral hydrogen, the abundance of Lyα emitters should decrease as observations probe into the era where there is neutral gas (e.g., Malhotra & Rhoads 2004; Ouchi et al. 2010; Kashikawa et al. 2011). The recent discovery of large numbers of candidate galaxies beyond $z \simeq 7$ through multi-color imaging undertaken with the infrared Wide Field Camera (WFC3/IR) onboard Hubble Space Telescope (HST) (e.g., Bouwens et al. 2010a; Bunker et al. 2010; Finkelstein et al. 2010; McLure et al. 2010) now makes it feasible to track the occurrence of Lyα line emission to interesting redshifts where neutral hydrogen may be present.

Of course, astrophysical factors other than a neutral IGM can also affect the presence of Lyα emission. Because of this, an alternative approach for gauging when reionization occurred, introduced by Stark et al. (2010) (hereafter Paper I), is to spectroscopically measure *the fraction of Lyα emission within color-selected Lyman Break Galaxy (LBG) populations.* Tracking the redshift-dependent fraction in a well-defined population avoids consideration of absolute changes in the host galaxy number density, such as has been the case in studies based on the luminosity function of narrow-band selected Lyman α emitters (LAEs). Furthermore, evolution in dust obscuration can be independently tracked via correlations seen with the colors of the rest-frame UV continuum. Paper I presented a comprehensive survey of over 600 LBGs with deep spectra, mostly undertaken with the DEIMOS instrument on Keck, but including published samples from the Very Large Telescope (VLT, Vanzella et al. (2009) and references therein). In that paper we demonstrated the utility of the method and discussed the paucity of line emission in gravitationally-lensed $z > 7$ candidates from the sample of Richard et al. (2008).

In Stark et al. (2011) (hereafter Paper II), through ultra-deep exposures with DEIMOS we significantly improved the line emission statistics at $z \simeq 6$, providing a robust measure of the rest-frame EW distribution of Lyα emission at the highest redshift when the Universe is believed to be fully ionized (Fan et al. 2006, c.f. Mesinger 2010). This provides a sound basis for predicting the likelihood of emission at higher redshift and thereby enabling a test of whether there is absorption by neutral gas. Significantly, we found that over 50% of moderately-faint ($-20.25 < \mathrm{M_{UV}} < -18.75$) $z \simeq 6$ LBGs exhibit strong emission with rest frame EWs > 25 Å. As this fraction increases over $4 < z < 6$, we argued on continuity grounds that we should expect a high success rate in recovering line emission from the newly-found WFC3/IR samples of $z > 7$ LBGs *unless* we encounter a more neutral IGM in the short time interval prior to $z \simeq 7$. Some evidence for this is seen in the recent

studies of Fontana et al. (2010) and Vanzella et al. (2011).

The present paper is concerned with an initial application of this test to the newly-available sample of WFC3/IR candidates with photometric redshifts in the redshift range $6.3 < z < 8.8$. Two important factors have motivated and shaped our program. Firstly, it is important to note that Lyα emission is the only spectroscopic redshift indicator for galaxies beyond $z \simeq 6$. Since it is the absence of strong Lyα emission that provides the basis for considering an increased neutral fraction, it is important to be sure that the targets are truly at the expected redshifts. Many early candidate LBGs believed to lie beyond $z \simeq 6 - 7$ remained controversial because of their limited or marginal photometry. The improved filter set and superior performance of WFC3/IR has given us confidence that the current list of $z \simeq 7 - 8$ candidates is more robust than those based on earlier NICMOS data (Robertson 2010b). Secondly, to match the lower redshift data, sampling from a similarly wide range of LBG luminosities, as we do here, will be advantageous. As shown in Papers I and II, the fraction of line emission increases in intrinsically fainter sources and so by comparing fractions with respect to their LBG luminosities, we may gain additional evidence for the onset of the neutral era.

Throughout the paper, we adopt a Λ-dominated, flat universe with $\Omega_\Lambda = 0.7$, $\Omega_M = 0.3$, and $\mathrm{H_0} = 70\,\mathrm{h_{70}}\ \mathrm{km\,s^{-1}\,Mpc^{-1}}$. All magnitudes in this paper are quoted in the AB system (Oke & Gunn 1983).

2.2 Observations

In compiling a target list for this program, we are guided by the need for a robust photometric redshift for each galaxy based on improved photometry from WFC3/IR and a range of rest-frame UV luminosities ($\mathrm{M_{UV}}$[1]). Our primary source of targets for the wide-field multi-slit capabilities of the Low Resolution Imaging Spectrometer (LRIS) on the Keck I telescope (Oke et al. 1995) equipped with a new red-sensitive CCD was i' and z'-drop candidates whose photometric redshifts $z > 6.3$ from the HST Early Release Science (ERS) field (Hathi et al. 2010; McLure et al. 2011). The grating for these observations was blazed at 600 lines $\mathrm{mm^{-1}}$. On January 7 and February 4 2011 we secured 7 hours of on-source integration for 8 suitable targets on a single mask using slit widths of $1''$, observed through a median seeing of $0.98''$.

In a more ambitious campaign probing to higher redshift we also targeted 3 z'-drop sources from the Hubble Ultradeep Field (HUDF) P34 field (GO 11563, PI: Illingworth) and an additional gravitationally-lensed source in the cluster MS0451-03 (GO 11591, PI: Kneib) using the near-infrared spectrograph NIRSPEC (McLean et al. 1998) during November 14-17 2010 and Jan 14-15 2011. This extends our search for Lyα emission up to a redshift $z \simeq 8.2$. Although we undertook extended integrations on all 4 sources with a $0.76''$ slit, tracking difficulties affected some exposures. To

[1]corresponding to a rest wavelength $\lambda \simeq 1500$ Å (Paper I)

determine the effective on-source integration time, we secured our astrometric position for each exposure by locating objects visible in the slit viewing camera to a precision of $\sim 0.2''$. We continued this campaign over May 15-18 2011. During these 4 nights, we did not encounter any tracking difficulties and, in excellent conditions, successfully used NIRSPEC to study an additional 7 WFC3-IR dropouts drawn from numerous surveys: the BoRG pure parallel survey (Trenti et al. 2011) (also independently discovered by Yan et al. 2011), the EGS region in CANDELS (Grogin et al. 2011; Koekemoer et al. 2011), and the lensing clusters Abell 1703 (GO 10325, PI: Ford, Bradley et al. 2012b), and Abell 2261 (CLASH survey, Postman et al. 2012).

We reduce the LRIS data following standard procedures, with bias subtraction and flat-fielding using dome exposures. We used the Kelson (2003) code to remove spatial and spectral distortion and to model and subtract the sky emission. Wavelength calibration was determined directly from sky lines. A final two-dimensional spectrum was extracted for each object with pixels binned logarithmically by $\Delta\log(\lambda) = 4.02 \times 10^{-5}$. As in Papers I and II, we search through the two-dimensional spectrum visually to identify emission lines, and confirm these with a boxcar extracted one-dimensional spectrum.

Our exposures with NIRSPEC were conducted with typical spatial dithering of $5''$. In the case of some lensed sources, we dithered by longer amounts to ensure the arc was oriented along the slit, and was not spatially coincident with any background objects. We flat-fielded and sky-subtracted the spectra using IDL routines written by G. Becker (2010, private communication). To compute the camera distortion and spectral curvature, we fit traces of standard stars along the slit, and skylines perpendicular to the slit. From this, we then derive a wavelength and sky position for all pixels in each two-dimensional spectrum, which were used to align the individual exposures. A final spectrum was created for each object by median stacking all exposures to eliminate signals from cosmic ray strikes.

Table 2.1 Catalog of sources with Keck spectroscopy and emission line properties, when detected. 1σ magnitude errors are listed in parenthesis. For non-detections, we list 2σ limiting magnitudes. For our NIRSPEC targets, times correspond to exposures in filters N1 and N2, which cover wavelength ranges of 9470 - 11210 Å and 10890 - 12930 Å, respectively.

ID	R.A.	Dec	z_{850}	J_{125}	H_{160}	μ[1]	z_{phot}	t_{exp} [hr]	z	EW [Å]
				LRIS						
ERS 5847[48]	03:32:16.0	-27:43:01.4	26.6(0.1)[2]	26.6(0.1)	26.7(0.1)	-	6.48	7		
ERS 7376[48]	03:32:29.5	-27:42:04.5	27.2(0.1)[2]	27.0(0.1)	27.0(0.1)	-	6.79	7		
ERS 7412	03:32:10.0	-27:43:24.0	26.9(0.1)[2]	27.0(0.1)	26.7(0.1)	-	6.38	7		
ERS 8119	03:32:29.5	-27:41:32.7	27.7(0.2)[2]	27.1(0.1)	27.5(0.1)	-	6.78	7		
ERS 8290	03:32:13.4	-27:42:30.9	27.3(0.1)[2]	27.1(0.1)	26.8(0.1)	-	6.52	7		
ERS 8496[4]	03:32:29.7	-27:40:49.9	27.2(0.1)[2]	27.3(0.1)	27.5(0.1)	-	6.52	7	6.441	69 ± 10
ERS 10270	03:32:29.5	-27:42:54.0	28.1(0.1)[2]	27.4(0.1)	28.0(0.2)	-	7.02	7		
ERS 10373	03:32:27.0	-27:41:42.9	27.5(0.1)[2]	27.4(0.1)	27.8(0.2)	-	6.44	7		
				NIRSPEC						
A1703_zD1[5]	13:14:59.4	51:50:00.8	25.8(0.2)	24.1(0.1)	24.0(0.1)	9.0	6.75	2, –		
A1703_zD3[5]	13:15:06.5	51:49:18.0	26.8(0.5)	25.5(0.1)	25.1(0.2)	7.3	6.89	2, –		
A1703_zD6[5]	13:15:01.0	51:50:04.3	27.9(0.5)	25.8(0.1)	25.9(0.1)	5.2	7.02	5, 3	7.045	65 ± 12
A1703_zD7[5]	13:15:01.3	51:50:06.1	> 28.5	26.8(0.2)	26.4(0.2)	5.0	8.80	5, 3		
A2261_1	17:22:28.7	32:08:30.9	> 28.6	26.9(0.1)	27.3(0.1)	3.5	7.81	5.7, –		
BoRG_58_1787_1420[6]	14:36:50.6	50:43:33.6	> 27.9[2]	25.8(0.1)	25.9(0.2)	-	8.27	2, 3		
EGS_K1	14:19:24.2	52:46:36.2	> 27.8[3]	25.3(0.1)	25.4(0.1)	-	8.27	2.5, –		
HUDF09_799[7]	03:33:09.1	-27:51:55.4	> 29.1	27.7(0.1)	27.6(0.2)	-	6.88	4.5, –		
HUDF09_1584[7]	03:33:03.8	-27:51:20.4	27.2(0.1)	26.7(0.1)	26.6(0.1)	-	7.17	5.5, –		
HUDF09_1596	03:33:03.8	-27:51:19.6	27.3(0.1)	26.8(0.1)	26.8(0.1)	-	7.45	5.5, –	6.905?	30 ± 15
MS0451-03_10	04:54:08.8	-3:00:29.1	> 28.3	26.7(0.1)	26.9(0.1)	50	7.50	2.5, –		

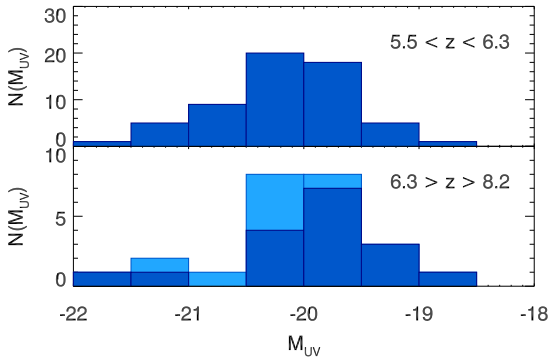

Figure 2.1 Distribution of rest-frame UV absolute magnitudes, M_{UV}, for i'-drop sources discussed in Paper II with z $\sim$ 5.5-6.3 (top panel) compared with those for the present survey of i' and z'-drops at z $\geq$ 6.3 (lower panel). There is an additional dropout, A2261_1, not shown on this histogram at $M_{UV} \simeq -16$. Dark shading in the lower panel refers to sources selected on the basis of WFC3/IR imaging in the Keck campaign (Table 2.1); light shading refers to additional data drawn from the VLT campaign of Fontana et al. (2010).

In total, this paper therefore presents the results of Keck spectroscopy for 19 WFC3-IR selected sources whose photometric redshifts lie in the range $6.3 < z < 8.8$. A summary of the new observations is given in Table 2.1. To this sample, we add a further 7 $z > 6.3$ sources discussed by Fontana et al. (2010). Figure 2.1 compares the UV absolute magnitude distribution of the combined sample with that presented for the redshift range $z \simeq 5 - 6$ in Paper II; clearly the samples span a similar luminosity range. This luminosity range is broader than the recent work of Ono et al. (2012) and Pentericci et al. (2011). In similar spectroscopic follow-up campaigns, they target brighter dropouts, primarily with $M_{UV} < -21.4$, and $-21.75 < M_{UV} < -20.0$, respectively.

Remarkably, from the new Keck exposures, we find very few convincing detections of line emission. Figure 2.2 (bottom panel) shows a 2-D spectroscopic montage of 4 sources for which line emission may be present, of which one case (HUDF09_1596) is marginal (2σ) and the other (ERS 8290) lies outside the expected redshift range if it is Lyα.

The emission line apparently seen in ERS 8290 (a z'-band dropout) is detected at $>5\sigma$ with a flux of $6.7 \pm 0.8 \times 10^{-18}$ erg cm^{-2} s^{-1} at $\lambda 7644 \pm 2$ Å. It also exhibits the asymmetric profile characteristic of Lyα in the 1D extraction, but this would place the object at $z = 5.286$, quite discrepant from our photometric estimate of $z = 6.52$. However, upon examining the positioning of our LRIS slits more carefully (bottom panel of Figure 2.2), we find there is a faint V-drop candidate with $i' = 27.5$ and $z' = 27.9$ only $0.4''$ away, which would have been at least partially visible through our slit during the exposure. After subtracting the line flux from the i'-band photometry, we determine a photometric redshift of $z = 4.91$, in reasonable agreement with the Keck spectroscopy, particularly given a greater line flux (as is likely given the object's poor positioning in the slit) would

increase the photometric redshift estimate. The resolution of the confusion arising from these two proximate sources emphasizes again the prominence of Lyα emission in low luminosity $z \simeq 5-6$ sources (Papers I and II).

The two satisfactory detections refer to emission at λ9045 $\pm$2 Å for ERS 8496 in the LRIS mask and emission at λ9780 $\pm$ 4 Å in the NIRSPEC exposure of the lensed source Abell 1703_zD6. Both objects are detected at $\geq 5\sigma$ in our final exposures. In our 1D extraction of ERS 8496, the emission line has a FWHM of 9 $\pm$ 1 Å, and displays an asymmetric profile with a steeply rising blue edge and slowly decaying red tail, characteristic features of Lyα at high redshift. Because our spectral resolution is significantly lower (6.5 Å for NIRSPEC versus 4.1 Å for LRIS) in our spectrum of A1703_zD6, so we are unable to determine any line profile information. The emission feature is seen independently in coadditions on two separate nights, indicating its reality.

If both lines are Lyα, the implied spectroscopic redshifts for ERS 8496 and Abell 1703_zD6 are $z = 6.441 \pm 0.002$ and 7.045 ± 0.004, respectively, in excellent agreement with our photometric predictions of 6.52 and that of 7.0 derived by Bradley et al. (2012b). The measured line fluxes for the two objects are 9.1 ± 1.4 and $28.4 \pm 5.3 \times 10^{-18}$ erg cm^{-2} s^{-1}. We then assume a spectral slope of β = -2, which is characteristic of galaxies at this redshift (Dunlop et al. 2012), though there may be evidence for steeper slopes at sub-$L_\star$ luminosities (Bouwens et al. 2010b). Under this assumption, taking the magnitude from the first filter in which the object is detected (Y_{098M} for ERS 8496, and J_{125} for 1703_zD6), we calculate EWs of 69 $\pm$ 10 and 65 $\pm$ 12 Å, respectively. Because our objects have additional coverage longward of the detection filter, we can also compute a value for β, and extrapolate to find the continuum flux at λ_{rest} = 1216 Å. Using the formulae of Dunlop et al. (2012), we find β = -2.39 $\pm$ 0.55, and -2.44 $\pm$ 0.64. When computing EWs using this method, we obtain 67 $\pm$ 11 and 59 $\pm$ 12 Å, respectively.

2.3 Analysis

Our approach in this paper is to compare the rate of occurrence of Lyα in our new $6.3 < z < 8.8$ sample with that expected from our reference sample of i'-drops with $5.5 < z < 6.3$ drawn from Paper II (Figure 2.1). In both Papers I and II we showed that the rest-frame EW distribution is a function of rest-frame UV absolute magnitude, M_{UV}, and thus we additionally take this luminosity dependence into account. We estimate the luminosities of all our sources in Table 2.1 from their photometric redshift and incorporate the lensing magnification μ for our lensed sources from Bradley et al. (2012b) for Abell 1703 and from the mass model of Richard et al. (2010) for MS0451-03 and Abell 2261. For our baseline Lyα EW distribution, we use the data from of Paper II at $z \simeq 6$, separated into high and low luminosity regimes.

The fraction of emitters within each bin of EW > 25 A is taken directly from Figure 2 of Paper

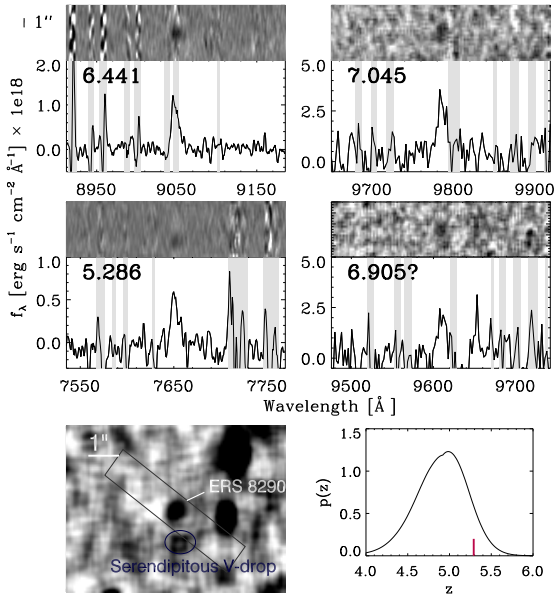

Figure 2.2 Montage of Lyα emission detected from 4 sources in our Keck survey, along with boxcar-extracted 1D spectrum. Wavelength ranges contaminated by strong skylines are shaded in grey in the 1D extraction. The top row shows the two robust detections of ERS 8496 and A1703_zD6 at $z = 6.441$ and z=7.045, respectively. The bottom row shows a marginal detection at z=6.905 for HUDF09_1596 and a likely $Ly\alpha$ line at $z = 5.286$ arising from a serendipitous V-drop close to ERS 8290 as illustrated in the bottom left slit image. The bottom right panel shows the photometric redshift distribution for this serendipitous V-drop, with a vertical line indicating the observed spectroscopic redshift (see text for further details).

II. We set the slope of the distribution within an EW bin equal to the slope between the two lowest bins in Paper II, 25 Å < EW < 55 Å, and 55 Å < EW < 85 Å. This slope is equal to $dp(\mathrm{EW})/d\mathrm{EW}$ = −0.0030 for the lower luminosity sample (−20.25 <M_{UV} < −18.75), and −0.0017 for the higher luminosity sample (−21.75 <M_{UV} < −20.25). To create the probability distribution for galaxies with EW less than 25 Å, we extrapolate to EW = 0 Å using this slope, and assign the remaining fraction of galaxies as non-emitters. In Papers I and II we also showed the fraction of emitters is a function of redshift, rising significantly for lower luminosity sources over $4 < z < 6$, most likely as a result of reduced dust extinction in the early Lyman break population. Therefore, as discussed in Paper II, we have also used a projected rest-frame EW distribution at $z \simeq 7$, assuming this evolutionary trend continues beyond $z \simeq 6$.

Two key factors enter into the calculation of the visibility of line emission in a ground-based survey. Firstly, for any target with a particular photometric redshift likelihood function $p(z)$, it may be that the spectral region surveyed by LRIS or NIRSPEC does not completely cover the expected wavelength range where Lyα might be present. Secondly, the EW limit for Lyα emission will be a highly non-uniform function of wavelength due to the mitigating effect of night sky emission. Provided the photometric redshift solution we derive is robust, we can estimate both factors and hence derive the likelihood of seeing Lyα for each of our 26 sources, assuming the relevant wavelength range studied and the exposure time secured, if the particular source of a given M_{UV} has a EW distribution drawn from the sample with $5.5 < z < 6.3$.

In the case of those sources for which the wavelength range searched does not fully sample the extended $p(z)$, we reduce the detection likelihood by the fraction of the integrated $p(z)$ that lies outside our search range. For each target, we determine its redshift probability function $p(z)$ using the photometric redshift code EAZY (Brammer et al. 2008). To determine the varying visibility function within our search range, we first estimate the the noise within an aperture encompassing the expected profile of the line, assuming an emission line width of 10 Å FWHM, which is typical of those detected in Paper II. Figure 2.3 illustrates the 5σ EW limit as a function of wavelength (and Lyα redshift) for most sources in our 12 hour LRIS exposure ($6.3 < z < 7.2$) and a typical source studied with NIRSPEC ($6.8 < z < 8.2$) during a 5 hour exposure. We note that although our survey spans a large range in redshift ($6.3 < z < 8.8$), the $p(z)$ distributions for individual galaxies typically span a much smaller range. The average 1σ redshift confidence interval for sources in our sample is only $\Delta z = 0.43$.

Since the NIRSPEC exposures were usually single-object exposures, the limits vary from source to source depending on the conditions and exposure times. We then apply a completeness correction to account for the fact that an emission line may fall in a noise trough and lie undetected, despite having an intrinsic flux above the 5σ limit. To estimate this completeness correction, we follow the methods discussed in detail in Paper II, where we simulate the addition and recovery of fake

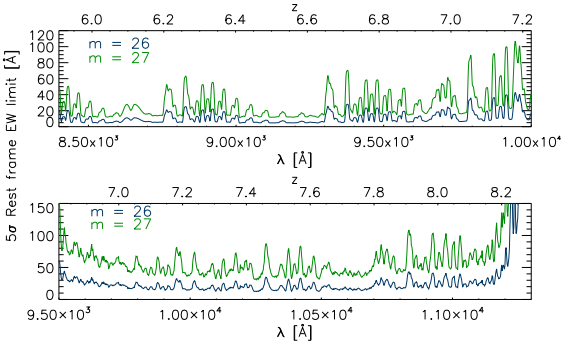

Figure 2.3 Sensitivity limits to Lyα emission in our new Keck spectroscopic campaign: The panels show the 5σ limiting EW calculated for a typical source studied in our 12 hour multi-slit LRIS exposure (top) and an example 5 hour long slit NIRSPEC observation (bottom). The limits vary from source to source depending on the continuum brightness and the exposure times. An additional completeness correction is taken into account by adding and attempting to recover fake emission lines with fluxes equal to the 5σ flux limit at the wavelength of insertion. See text and Paper II for more detailed discussion.

line emission in our actual spectra, again assuming a FWHM of 10 Å. As the absolute limits vary from source to source our Keck survey is not complete to a fixed EW limit but, provided the limits are well-understood for each source, we can readily estimate the probability of seeing Lyα in our exposures. In the case of the Fontana et al. (2010) FORS2 survey we estimated the night sky emission from our own LRIS exposures normalizing the limits from numerical data supplied in that paper.

The above simulations can be used to verify that our Keck survey is well-placed to search for Lyα emission. Out of the combined 26 targets from our survey and that of Fontana et al. (2010), 24 are covered spectroscopically over more than half the integrated probability of their photometric redshift distribution, and 17 are covered over 95% of the range. Additionally, we are able to determine the fraction of our spectra occulted by OH sky emission. For example, for a J=27 galaxy in one of our LRIS exposures, we are sensitive to lines with EW $\geq$ 30 Å over 70% of our usable spectral range (see Figure 2.3). Similarly, for a 5 hr NIRSPEC exposure of a J= 27 galaxy, we are sensitive to lines with EW $>$ 55 Å over 49% our spectral range.

The results of the simulations are shown in Figure 2.4 where, depending on whether we adopt the EW distribution observed at $5.5 < z < 6.3$ or that extrapolated to $z \simeq 7$ in Paper II assuming continuity in redshift-dependent increase in line emission seen over $4 < z < 6$, we would expect to recover 7-8 emission lines in the combined Keck and VLT surveys. In contrast, we have only 2 robust detections (both in the Keck sample, Figure 2.2) and at most 4 including the marginal candidate discussed by Fontana et al. (2010) and HUDF09_1596 at $z = 6.905$ shown in Figure 2.2. Assuming all the targeted sources are at $z > 6.3$, given our previously mentioned assumptions, our

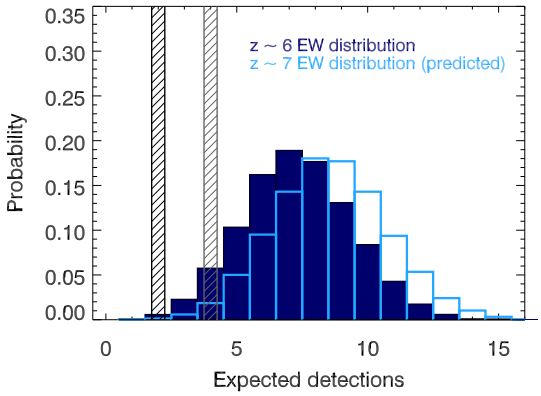

Figure 2.4 The expected number of detected Lyα emission lines with greater than or equal to 5σ significance in the combined Keck and VLT survey of 26 sources. The blue histogram shows the likelihood function for 10,000 Monte Carlo realizations assuming the intrinsic line emission properties follow the luminosity dependence seen in our $5.5 < z < 6.3$ i'-drop sample (Figure 2.1 (top)). The open histogram shows the expectation if the fraction of line emitters continues to increase with redshift at the rate described in Paper II. Vertical lines show the recovered number of emitters (robust and maximal including marginal detections in both the Keck and VLT surveys).

results reject the input EW distributions at the 99.3% level of significance (91.4% if the two marginal detections are included).

We can display the significance of this downturn with increasing redshift in the terms of the fraction of Lyα emission seen in Lyman break galaxies, X(Lyα), as in Paper I. The difficulty we face in creating such a figure is the non-uniform EW limit across the various targets in the Keck and VLT campaigns, in contrast to the more straightforward uniform search we undertook with DEIMOS at $4 < z < 6$. To account for this, we assume a simple model in which Lyα emission is transmitted without IGM absorption for a fraction f of galaxies, while it is fully extinguished by the IGM for a fraction of galaxies (1-f). We assume that $f = 1$ at redshifts below 6, where the universe is believed to be highly ionized (Fan et al. 2006), and that f is independent of the intrinsic EW of a Lyα emission line. We caution that an interpretation in terms of absolute values of f is premature, as there is still some debate on whether the IGM is fully ionized at $z \sim 6$ (Mesinger 2010), but emphasize that our value of f at $z \sim 7$ is computed relative to the value assumed at $z \sim 6$. Additionally, with the increased fraction of emitters in our $z \sim 6$ sample from Paper II, we do not see any evidence for a decrease in f prior to $z \sim 6$, though we cannot rule it out.

It is important to note that our f is differs from $f_{esc}^{Ly\alpha}$, commonly defined in the literature as the total escape fraction of Lyα photons (e.g., Hayes et al. 2011). $f_{esc}^{Ly\alpha}$ represents the total transmission of Lyα, accounting for both attenuation of photons within the galaxy by mechanisms such as dust, as well as any attenuation by the IGM. Our definition of f is only intended to account for any

downturn in the fraction of LBGs which show observable Lyα emission from the $z = 6$ (or $z = 7$) extrapolated EW distributions from Paper II, and represents an IGM extinction averaged over the entire population.

To compute the most likely value of f, we undertake Monte Carlo simulations using the previously described EW distributions, but with f now added as a free parameter. We vary f from 0 to 1 in steps of 0.01, and compute N=1000 simulations for each step. We can then calculate the probability distribution for f given our N_{obs}=2 confirmed sources using Bayes' theorem:

$$p(f|N_{obs} = 2) = \frac{p(N_{obs} = 2|f)p(f)}{\int_0^1 p(N_{obs} = 2|f)df} \tag{2.1}$$

Here, $p(f)$ is the prior probability for f, which we take to be uniform for $0 \leq f \leq 1$, and $p(N_{obs} = 2|f)$ is the probability, drawn from our Monte Carlo simulations, that we would find $N_{obs} = 2$ sources for a given value of f. Assuming that the intrinsic EW distribution for our observed sources is that of Paper II at $z = 6$, we find $f = 0.45 \pm 0.20$, while using the $z = 7$ extrapolated distribution yields $f = 0.34^{+0.24}_{-0.15}$. In the Figure 2.5, we plot the value of X(Lyα) in the same luminosity bins of Paper II, as predicted by our best fit values of f.

We stress that this figure is intended to serve as a continuation of the visualization provided in Papers I and II, rather than a statistiscal result of our study. Due to our strongly varying limiting EW sensitivity (as a function of both wavelength and object magnitude), choosing a fixed EW limit will exclude a non-negligible fraction of useful data from our analysis. Our Monte Carlo simulations are able to utilize the full data set, simulating whether we would have likely seen a line even when our EW limits are above the fixed thresholds used in Figure 2.4, and thus represent the major statistical result of this study.

Using the models of McQuinn et al. (2007) to predict what global neutral hydrogen fraction, X_{HI} would be required to account for this decline, we find $X_{HI} \simeq 0.44$, and $X_{HI} \simeq 0.51$, respectively. The models of Dijkstra et al. (2011), which provide a more comprehensive treatment of Lyα radiative transfer through outflows, result in an increased value for X_{HI} in both cases.

2.4 Discussion

Although we consider the most likely explanation for our observed decrease in the number of LBGs which show observable Lyα emission to be an increase with redshift in the neutral fraction of the IGM, it is important to remember our assumptions. Foremost we have assumed that *all* of our 26 targets have true redshifts beyond $z \simeq 6.3$. Should there be low redshift interlopers or Galactic stars in our new sample, we will overestimate the decline in the Lyα fraction. Secondly, we have assumed the DEIMOS spectra from Paper II constitute a representative sample for calculating the expected

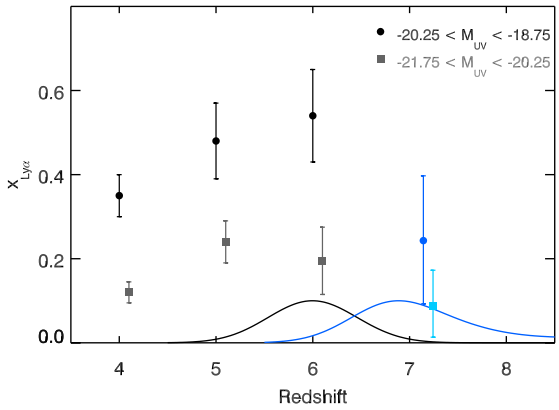

Figure 2.5 The redshift-dependent fraction of color-selected Lyman break galaxies that reveal Lyα in emission, X(Lyα), adjusted as discussed in the text to approximate one within a similar luminosity range with a rest-frame EW in excess of 25 Å. Data points for the galaxies with $-21.75 < \mathrm{M_{UV}} < -20.25$ are displaced by +0.1 in redshift for clarity. Data over $4 < z < 6$ is from Paper I and Paper II, and new estimates beyond $z > 6.3$ are derived from the present paper, including sources discussed by Fontana et al. (2010). The curves shown represent the aggregate redshift probability distributions for our sources in the z $\simeq$ 6 bin (black), and the z $\simeq$ 7 bin (blue); probability distributions for individual sources are typically much sharper.

EW distribution for $6.3 < z < 8.2$. Although the uncertainties here are not as great, we plan further studies with DEIMOS to increase the statistical sample of $5.5 < z < 6.3$ LBGs.

Of course our observed decrease in the Lyα fraction could also be attributed to an increased opacity arising from dust within the LBGs. However, given the blue UV continuum slopes observed for galaxies with $z > 6.3$ (Bouwens et al. 2010b; Dunlop et al. 2012), we consider this explanation unlikely.

Our diagnosis of a possible increase in the neutral hydrogen fraction beyond $z \simeq 6.3$ is supported by the earlier study by Fontana et al. (2010). They found 1 marginal candidate out of 7 targets whereas we found 2 robust and 1 marginal cases out of our 19 targets spanning a larger luminosity and redshift range. Our conclusion is also supported by LAEs studies at $z = 5.7$ and 6.5 by Ouchi et al. (2010) and Kashikawa et al. (2011). Compared to $z = 5.7$, their LAE sample at $z = 6.5$ displays systematically lower EWs for Lyα. They also derive little evolution in the rest UV luminosity function for LAEs, but a decrease in the Lyα LF, which could be explained by an increase in X_{HI}. Our derived values of X_{HI} are slightly higher than that of Kashikawa et al. (2011), perhaps consistent with our survey probing to higher redshifts than their $z = 6.5$ LAEs. Hayes et al. (2011) have recently compiled results from numerous Lyα and UV luminosity function studies to derive a volumetrically averaged Lyα escape fraction, and find very similar results. Their derived Lyα escape fraction steadily increases with redshift below $z = 6$, then tentatively drops off at higher redshifts.

Very recently, Ono et al. (2012) report the convincing detection of Lyα emission in a small

fraction (3/11) of LBGs that, by virtue of their selection using Subaru imaging, are more luminous ($M_{UV} < -21$) than most of the objects considered here. Such a complementary campaign targeting luminous LBGs selected from larger volumes will provide further insight into whether reionization is responsible for the declining fraction of line emission.

We note that our measured decrease in the fraction of LBGs with strong Lyα potentially agrees with the result of Cowie et al. (2011). Although they argue against any evidence for reionization at $z = 6.5$, they find that $\sim 24\%$ of galaxies at this redshift show strong Lyα emission, comparable to the fraction we detect in this work, spread across a larger redshift range.

With the new generation of multi-object, near infrared spectrographs, such as MOSFIRE, set to come online soon, the prospects for this field are bright. In addition to the significant multiplexing advantage, the increased sensitivity of these detectors will allow us to probe the lower luminosity ranges at $z \geq 6.5$ to EW limits comparable to those in Paper II between sky lines. Having such a statistical sample is key for allowing the quantification of any change in the hydrogen neutral fraction.

Chapter 3

The UV Luminosity Function of Star-Forming Galaxies via Dropout Selection at Redshifts z $\sim$ 7 and 8 from the 2012 Ultra Deep Field Campaign

Abstract

We present a catalog of high redshift star-forming galaxies selected to lie within the redshift range $z \simeq$ 7-8 using the Ultra Deep Field 2012 (UDF12), the deepest near-infrared (near-IR) exposures yet taken with the Hubble Space Telescope. As a result of the increased near-infrared exposure time compared to previous HST imaging in this field, we probe ~ 0.65 (0.25) mag fainter in absolute UV magnitude, at $z \sim 7$ (8), which increases confidence in a measurement of the faint end slope of the galaxy luminosity function. Through a 0.7 mag deeper limit in the key F105W filter that encompasses or lies just longward of the Lyman break, we also achieve a much-refined color-color selection that balances high redshift completeness and a low expected contamination fraction. We improve the number of drop-out selected UDF sources to 47 at $z \sim 7$ and 27 at $z \sim 8$. Incorporating brighter archival and ground-based samples, we measure the $z \simeq 7$ UV luminosity function to an absolute magnitude limit of $M_{\rm UV} = -17$ and find a faint end Schechter slope of $\alpha = -1.87^{+0.18}_{-0.17}$. Using a similar color-color selection at $z \simeq 8$ that takes account of our newly-added imaging in the F140W filter, and incorporating archival data from the HIPPIES and BoRG campaigns, we provide a robust estimate of the faint end slope at $z \simeq 8$, $\alpha = -1.94^{+0.21}_{-0.24}$. We briefly discuss our results in the context of earlier work and that derived using the same UDF12 data, but with an independent photometric redshift technique (McLure et al. 2013).

3.1 Introduction

Great progress has been made in recent years in studies of the population of star-forming galaxies at redshifts $z \simeq 7-8$. Following installation of the infrared Wide Field Camera 3 (WFC3) on the Hubble Space Telescope (HST), the number of candidates has risen from a few (Bouwens et al. 2008) to $\simeq 100$ (McLure et al. 2010; Bouwens et al. 2010a; Oesch et al. 2010; Yan et al. 2010). In addition to providing hints of the early galaxy population to $z \simeq 8$, previous data sensitive to $z \sim 7$ galaxies have provided initial determinations of their rest-frame UV colors, stellar populations (McLure et al. 2011; Bouwens et al. 2012b; Dunlop et al. 2012), stellar masses and likely ages (Labbé et al. 2010; González et al. 2010; McLure et al. 2011; Finkelstein et al. 2012b), and nebular emission line strengths (Labbé et al. 2013). Our work builds upon these previous efforts to present the first drop-out selected samples and luminosity function determinations for redshift $z \sim 7$ and $z \sim 8$ sources from the 2012 Hubble Ultra Deep Field project (hereafter UDF12; GO 12498, PI: R. Ellis).

Before UDF12, progress has naturally been greatest at redshift $z \simeq 7$ where synergy between ground- and space-based surveys has effectively exploited the full dynamic range of accessible galaxy luminosities. Early surveys from Subaru (Ouchi et al. 2009) and the ESO Very Large Telescope (Castellano et al. 2010) have probed the luminous component of the star-forming population over an area > 1000 arcmin^2. More recently, the UltraVISTA survey has covered 3600 arcmin^2 in the COSMOS field, locating $z \simeq 7$ galaxies to $M_{\rm UV} = -22.7$ (Bowler et al. 2012).

However, only HST can probe the important faint end of the galaxy luminosity function at these redshifts. An early result from the 2009 Hubble Ultra Deep Field campaign (GO 11563, PI: Illingworth, hereafter UDF09) was the discovery of an abundant population of sub-luminous galaxies at $z \simeq 7$ (Oesch et al. 2010; Bunker et al. 2010; McLure et al. 2010) corresponding to a Schechter faint end slope α between -1.7 to -2.0. In such a distribution, the bulk of the integrated luminosity density arises from low luminosity galaxies that may be responsible to maintaining cosmic reionization (Robertson 2010b).

Clearly the luminosity function of star-forming galaxies at redshifts $z \simeq$ 7-8 is of great importance. However, given the large range in luminosity that must be sampled, wider-field HST surveys have proved an important complement to panoramic ground-based surveys. WFC3 data from the GOODS Early Release Science (ERS) (Windhorst et al. 2011), and CANDELS fields (Grogin et al. 2011; Koekemoer et al. 2011) have sampled intermediate luminosities $-21 \lesssim M_{\rm UV} \lesssim -19$. The HIPPIES and BoRG pure parallel surveys have provided additional candidates at $z \sim 8$ (Yan et al. 2011; Trenti et al. 2011; Bradley et al. 2012a).

Collectively these surveys have provided a reasonably clear view of the galaxy luminosity function at $z \simeq$7 at the luminous end, but there remain disagreements regarding the precision with which the faint end slope is determined. While the UDF09 collaboration has measured a faint-end slope of

$\alpha_{z\sim7} = -2.01 \pm 0.21$ (Bouwens et al. 2011) incorporating the UDF, parallel fields, and the ERS data, a competing determination utilizing the size-luminosity relation measured from the UDF09 data and the CANDELS Deep+Wide surveys in three fields finds a shallower faint-end slope of $\alpha_{z\sim7} = -1.7 \pm 0.1$ (Grazian et al. 2012). The luminosity function at $z \simeq 8$ is even more uncertain, both because of the limited depth of the necessary photometry (Dunlop et al. 2012) and the possibility of contamination from lower redshift sources.

Distant star-forming galaxies are commonly found using some variant of the Lyman break technique pioneered by Steidel et al. (1996). At $z \gtrsim 6.5$, the opacity due to neutral hydrogen in the intergalactic medium means the source flux below a rest-wavelength $\lambda_{rest} = 1216$Å is dimmed by factors ≥ 5 (Madau 1995). A search exploiting this effect has utilized one of two methods. In the 'dropout' technique, objects are selected within a carefully-chosen window in color-color space specifically tuned to select star-forming galaxies within the required redshift range while minimizing the contribution from lower redshift contaminants. At $z \sim 7$ (where the Lyman break falls near the overlap of the HST z_{850} and Y_{105} filters) the Lyman dropout is chosen via a red color in $z - Y$, and the star-forming nature of the galaxy via a blue color in $Y - J$. Additionally, candidates are required to lie below a certain threshold in deep optical data; this further limits contamination by lower redshift sources. Early demonstrations of the drop-out technique at redshifts $z \gtrsim 6$ were presented by Bunker et al. (2004) and Bouwens et al. (2004).

An alternative approach uses the full array of broadband detections and upper limits in the context of photometric redshift codes (McLure et al. 2010; Finkelstein et al. 2010; McLure et al. 2011). These codes employ a range of synthetic spectra for galaxies (e.g., Bruzual & Charlot 2003) over all redshifts of interest, and optimum fits are produced for each source in the catalog. As in the dropout selection technique, leverage comes primarily from the Lyman break but the method is particularly advantageous when detections are available in more than 3 filters.

In general, agreement between the two techniques is often quite good (McLure et al. 2011). However, the methods are distinct and each has aspects relevant for interpreting their photometric samples. The SED method provides redshift probability distributions for individual sources but may be susceptible to systematic errors inherent in population synthesis models, such as uncertainties in the reddening law and star-formation histories, when differentiating between low-redshift interlopers and true high-redshift sources. In contrast, our drop-out selection utilizes the observed color information independent of stellar population synthesis modeling, but requires careful simulations to quantify the possible presence of low-redshift contaminants satisfying the break criterion. It also assumes that the intrinsic colors of possible contaminants do not differ at fainter luminosities. Given their complementary features, particularly for estimating contributions from contaminants, independent luminosity function determinations from both methods will be helpful in furthering progress. The goal of the present paper is therefore to exploit this unique data to provide the best current

constraints on the UV luminosity function of star forming galaxies at redshift 7 and 8 using the dropout technique. A companion UDF12 paper (McLure et al. 2013) presents the results of a search through the data for $z \geq 6.5$ candidates using the photometric redshift technique.

The present paper is one in a series devoted to scientific results from the UDF12 campaign, which provides a significant advance over the earlier UDF09 imaging in this field appropriate for the present luminosity function study and the complementary analysis discussed in McLure et al. (2013). The UDF12 survey design and its data processing is discussed in Koekemoer et al. (2013). Public versions of the final reduced WFC3/IR UDF12 images, incorporating all earlier UDF data, are available to the community on the UDF12 web page[1]. Initial $z \geq 8.5$ detections in the UDF12 data were presented by Ellis et al. (2013), while the UV continua of high-redshift candidates were measured by Dunlop et al. (2013). A review of the implications of the survey in the context of cosmic reionization including the results of the present paper is provided in Robertson et al. (2013).

A plan of the paper follows. In Section 3.2 we introduce the UDF12 data and the brighter ground-based and HST data sets and their reductions essential for realizing an analysis of the luminosity function at $z \simeq$7 and 8. Section 3.3 discusses the important decisions we have taken in color-color space to optimize the completeness of galaxies at these redshifts, while minimizing contamination from lower redshift sources. Section 3.3 also presents the final list of galaxies in the two redshift intervals that we use for our analysis. In Section 3.4 we present our luminosity functions and in Section 3.5 we briefly discuss our results in the context of earlier work, highlighting the important advances made possible through the UDF12 campaign.

Throughout this paper, we adopt a $\Lambda-$dominated, flat universe with $\Omega_\Lambda = 0.7$, $\Omega_M = 0.3$, and $\mathrm{H}_0 = 70\,\mathrm{h}_{70}\ \mathrm{km\,s^{-1}\,Mpc^{-1}}$. All magnitudes in this paper are quoted in the AB system (Oke & Gunn 1983). We will refer to the HST ACS and WFC3/IR filters F435W, F600LP, F606W, F775W, F814W, F850LP, F098M, F105W, F125W, F140W, and F160W as B_{435}, V_{600}, V_{606}, i_{775}, i_{814}, z_{850}, Y_{098}, Y_{105}, J_{125}, J_{140}, and H_{160}, respectively.

3.2 Data

Central to any analysis of the galaxy luminosity function is the collation of a complete sample of galaxies within the chosen redshift interval spanning a wide range in luminosities, free from bias and with any interlopers minimized. In this section we introduce the UDF12 and more luminous auxiliary datasets.

[1] http://udf12.arizona.edu/

3.2.1 UDF

To provide the best constraints on the faint end of the luminosity function at $z \simeq 7$ and 8, the primary advance of this paper is the increased depth and redshift fidelity provided by our new UDF12 survey. The UDF12 program dataset (described in full in Koekemoer et al. 2013) represents a significant improvement over the previous UDF09 observations in several respects. In particular, the survey was purposefully designed to improve our understanding of the redshift $z \simeq 7$ and 8 luminosity functions. Firstly, we increased the total exposure time in the key Y_{105} filter over that in the UDF09 campaign by a factor of 4, with the addition of 71 new orbits. As the Lyman break lies near the edge of the filter transmission profile for galaxies at $z \simeq 7$, this ensures we can probe significantly fainter (by $\simeq$0.4 mag) in absolute magnitude at $z \simeq$7 and with considerably greater fidelity in redshift selection at $z \simeq$8 (Ellis et al. 2013). A further improvement is the addition of comparable imaging in the newly-utilized J_{140} filter. By stacking our detections in this filter with either those at J_{125} at $z \simeq$7 or H_{160} at $z \simeq$8, we secure improved detections that correspond to extending the depth by an additional $\simeq$0.1 mag in each case.

Our final analysis is based on the compilation discussed by Koekemoer et al. (2013) which incorporates all earlier WFC3 imaging in the UDF including the earlier UDF09 campaign (GO 11563; PI: Illingworth) and less deep imaging undertaken as part of the CANDELS survey (GO 12060, PIs: Faber & Ferguson). In total the imaging constitutes 100, 39, 30, and 84 orbits in each of the Y_{105}, J_{125}, J_{140}, and H_{160} filters, respectively (see Koekemoer et al. 2013 for further details). An important associated dataset in this field is the ultra deep ACS imaging data from the 2004 UDF campaign (Beckwith et al. 2006) essential for a further rejection of low redshift sources.

3.2.2 Auxiliary data

To constrain the bright end of the $z \simeq 7$ and 8 luminosity functions we take advantage of several auxiliary WFC3 datasets which are somewhat shallower than our UDF12 data but nonetheless unique in their coverage and depth. At $z \simeq 7$, we include the UDF parallel fields, UDF-P1 and P2 (sometimes referred to as UDF-P12 and P34, respectively), from various surveys including UDF05 (GO 10532, PI: Stiavelli) and the aforementioned UDF09 survey, the Early Release Science (ERS) WFC3 campaign from the WFC3 Science Team (GO 11359, PI: O′Connell; Windhorst et al. 2011), and imaging in the GOODS-S field from CANDELS-Deep (Grogin et al. 2011; Koekemoer et al. 2011). We also adopt the datapoints from the ground-based surveys of Ouchi et al. (2009), Castellano et al. (2010), and Bowler et al. (2012), which provide vital observations of the rare population of galaxies brighter than $M_{\rm UV,\star}$.

At $z \sim 8$, it is difficult for ground-based programs to provide any meaningful constraints, so we instead include data provided by two HST pure-parallel WFC3 programs: HIPPIES (GO/PAR

11702, PI: Yan; Yan et al. 2011) and BoRG (GO/PAR 11700, PI; Trenti; Trenti et al. 2011; Bradley et al. 2012a). As the shortest wavelength coverage of these surveys is provided only with the V_{606W} (or V_{600LP}), Y_{098}, and J_{125} filters, a robust spectral break can only be verified between Y_{098} and J_{125}, as the wavelength spanned between V_{606W} and Y_{098} is too great and there remains no optical rejection filter at shorter wavelengths. Thus, these fields can only usefully identify galaxies at $z \sim 8$, and therefore we do not use them for our selection at $z \sim 7$.

Table 3.1. LF Datasets, candidates, and Survey Depth 5σ AB

Name	Area (arcmin^2)	z$\sim$7 candidates	z$\sim$8 candidates	Y_{105W}	J_{125W}	J_{140W}	H_{160W}
UDF12	4.6	47	27	30.0	29.5	29.5	29.5
UDF-P1	4.6	15	10	28.9	29.0	-	28.7
UDF-P2	4.6	13	10	29.0	29.2	-	28.7
ERS	36.8	15	4	27.6[a]	28.0	-	27.5
CANDELS-Deep	64.9	32	18	28.2	28.1	-	27.7

[a]The ERS program replaces the Y_{105} filter with the Y_{098} filter.

We summarize the filter coverage, survey area, limiting depths in the selection filter(s), and the number of high redshift candidates for each of these auxiliary datasets in Table 3.1.

3.2.3 Data Reduction

Prior to applying photometric color cuts optimized for the selection of $z \simeq 7$ and 8 galaxies, each survey data was similarly reduced to provide a series of processed and calibrated WFC3 frames. We describe below the data reduction steps taken for each field.

3.2.3.1 UDF and Parallels

The preliminary processing stages that yield images ready for source selection are discussed in detail by Koekemoer et al. (2013). Briefly, we first process the raw images using the Pyraf/STDAS task *calwf3*, which flags bad pixels, and corrects for bias and dark current throughout the detector. After processing, the images are then registered and stacked using a version of the MultiDrizzle algorithm (Koekemoer et al. 2003) to create the final mosaics on a pixel scale of $0.03''$ per pixel. This processing was carried out to create reductions of the UDF, UDF-P1, and UDF-P2 fields.

3.2.3.2 ERS and CANDELS-Deep

For the ACS data in the CANDELS-Deep and ERS fields, we use the publicly available v2.0 mosaics from the GOODS campaign (Giavalisco et al. 2004). We augment this with our own compilations of both the i_{814} and z_{850} data taken in parallel during the CANDELS WFC3 campaign. We combine the publicly available single epoch mosaics for these filters weighting by exposure time, using the image combination routine SWARP (Bertin et al. 2002). In the case of the z_{850} data, we add this to the already existing GOODS mosaic.

We combine the public WFC3 mosaics from the CANDELS team (Koekemoer et al. 2011) in the same manner across CANDELS-Deep. For the ERS WFC3 data, we use the reduction described in McLure et al. (2011). Due to the lack of sub-pixel dithering available in the wider area fields, the CANDELS and ERS mosaics were produced with final pixel scales of $0.06''$ per pixel.

3.2.3.3 BoRG + HIPPIES

As the BoRG and HIPPIES programs are pure parallel surveys, their data products differ significantly in many ways from those discussed above. Details of the relevant observation strategies can be found in Trenti et al. (2011) and Bradley et al. (2012a). The initial dataset presented in Bradley et al. (2012a) consists of 59 independent fields with an output pixel scale $0.08''$ per pixel and a median 5σ depth of 27.5 in J_{125}, which varies significantly from field to field.

We have analyzed the updated BoRG dataset, which includes a further 10 currently unpublished fields. We encountered significant difficulties in compiling a robust list of candidates. Although we assembled a final list of 48 candidate high-redshift objects, we cannot apply the same rigorous constraints in ensuring each is not an artifact or Galactic star due to the coarser pixel scale and absence of a dithered observing strategy. Such limitations are inherent in the use of the pure parallel observing mode.

Recognizing the unfortunate loss of valuable additional data, we did explore the issue of potential contamination from stellar sources via a simulation to determine how robustly we could rule out unresolved objects based solely upon the BoRG PSF. We created a galaxy template with a physical half-light radius of $0.10''$, chosen to match the median found for the luminous ($0.3 < L/L_{\star,z=3} < 1.0$) $z \sim 8$ UDF12 galaxies analysed in Ono et al. (2012). This template was then convolved with the measured PSF and inserted into the images, along with unresolved point sources, at steps of 0.1 in magnitude. Observed half-light radii of all inserted sources were then re-measured with SExtractor. We found that the 95% confidence intervals of our synthetic galaxies and genuine point sources already began to overlap at a detection significance of $\sim 24\sigma$ in the J_{125} filter (equivalent to an object with $J_{125} = 25.8$ for the median depth of the survey). Thus, at quite bright luminosities at $z \simeq 8$, it is very difficult to robustly exclude point sources. Ultimately, at the 5σ limit, the observed median half-light radii of point sources and synthetic galaxies differ by only 0.3, pixels rendering discrimination impossible.

In view of these challenges, we chose not to include our analysis of the uptodated BoRG data in our determination of the $z \sim 8$ luminosity function, other than inclusion of the data points of Bradley et al. (2012a). In Section 3.5, we note the effect of excluding this subset of data.

3.2.4 Photometry

In the case of the UDF12, which pushes HST to new limiting depths, we adopted a robust technique to locate and measure the fluxes from each faint source, rather than relying on errors output from the SExtractor source extraction code (Casertano et al. 2000). As the correlated noise produced as a result of applying the Multidrizzle algorithm produces a subtle underestimate of uncertainties when using SExtractor, in the specific case of the UDF12 we chose to use our own IDL photometry routine to compute all fluxes quoted in this paper.

We briefly summarize the various stages. Processing proceeds by using a χ^2 stack of all the images to identify regions of blank sky over the area in question. A grid of blank apertures is then generated, with separation larger than the `pixfrac` footprint of Multidrizzle, ensuring that noise between adjacent apertures is not correlated. To estimate the level of any residual background around an object of interest, we take the median flux of the 50 closest blank apertures. We adopt the root mean square of the flux in these blank apertures as our uncertainty in the background level.

Fluxes are then computed using the APER routine in IDL (Landsman 1993). For the shallower non-UDF12 fields, although we utilized SExtractor to compute fluxes and background levels, the flux uncertainties were still estimated using this improved technique.

As the HST point spread function (PSF) varies significantly with wavelength (particularly between the ACS optical images and near-infrared images from WFC3), it is important to account for this change when measuring accurate colors. To improve detections and color measurements for the faintest sources, aperture sizes should be quite small yet properly account for wavelength-dependent PSF variations. We chose circular apertures whose diameters encircle $\geq 70\%$ of the total flux from a point source. For the ACS B_{435}, V_{606}, i_{775}, i_{814}, and z_{850} filters, we adopted aperture diameters of $0.30''$ in all fields processed with $0.03''$ pixel diameter (UDF12, UDF-P1, and UDF-P2), and $0.40''$ in all other fields. For the WFC3 filters, the aperture diameters are $0.40''$, $0.44''$, $0.47''$, and $0.50''$, for Y_{105}/Y_{098}, J_{125}, J_{140}, and H_{160}, respectively. Such small apertures remain meaningful both because of the FWHM of the HST PSF (ranging from $0.09''$ in B_{435} to $0.17''$ in H_{160}), and the precise degree of alignment of the individual image sub-exposures (better the $0.005''$ in the UDF; Koekemoer et al. 2013). In a related paper, Ono et al. (2013) validate these choices by measuring half-light radii, r_{hl}, for stacks of our high-redshift samples, and find values of 0.36 kpc at both $z \sim 7$ and 8, which translate to angular half-light radii of $0.07''$ (not including any broadening due to the PSF). To correct to total magnitudes for the purposes of computing the luminosity function, we applied an aperture correction of 0.47 magnitudes, determined by measuring the flux of a synthetic galaxy template with this half-light radius that falls outside our apertures.

3.3 Candidate selection

We now turn to the photometric selection of star-forming galaxies at $z \simeq 7$ and 8, using the photometric catalogs generated as discussed in Section 3.2. A key issue for our dropout selection technique is the optimum choice of the two color cuts used to select candidates. The goal is to balance completeness in high z selection against a low fraction of foreground interlopers and spurious sources. As the available filter sets differ for each of the component surveys, we discuss each case in turn.

3.3.1 Potential contaminants

A selection criterion tuned to select only high-redshift galaxies at high confidence, with essentially no contamination, would be impractical, leading to a severely limited sample. In order to be inclusive in such a search, a crucial condition for an accurate determination of the luminosity function, a small degree of contamination can be tolerated, provided the fraction is reasonably well-understood.

In fact, the primary sources of contamination in high-redshift searches are now well-known. We briefly review them here. Low-temperature Galactic dwarf stars display quite similar colors to high

redshift galaxies in the near infrared (e.g., Bowler et al. 2012). While ground-based surveys can only constrain stellar contamination by comparing SEDs of cool stars to observed colors (Bowler et al. 2012), WFC3 data has the distinct advantage of an extremely sharp point-spread function, ranging from $0.15''$ in Y_{105} to $0.18''$ in H_{160}. Previous studies in the UDF have utilized this to conclude that Galactic stars are not expected to contribute significantly ($< 2\%$) to contamination in extremely deep, small area surveys (Finkelstein et al. 2010; Bouwens et al. 2011).

We have also investigated our ability to rule out unresolved contaminants with our UDF12 data. We conducted a simulation similar to that described in Section 3.2.3.3, inserting both point sources and simulated galaxies into the image and recovering their observed half-light radii distributions as a function of magnitude. In this case, we used a galaxy model with an intrinsic half-light radius of only $0.07''$, to match the value found for stacks of the faintest UDF12 galaxies in Ono et al. (2012). This template was then convolved with the observed PSF before insertion into the image. In this case, we found that the 95% confidence intervals of the point sources and our galaxy model did not overlap until $m = 28.6$. Brightward of this magnitude, none of the 19 high-redshift sources selected in this study show half-light radii consistent with a point source at the 2σ level, further reinforcing our conclusion that stellar contamination should not be significant.

A more relevant concern is potential interlopers at $z \sim 2$. Around this redshift, the Balmer and 4000Å breaks will lie near the same observed wavelengths where we search for a Lyman break in our high-redshift sources. However, unlike the Lyman break, the Balmer break has a maximum possible depth, aiding us in isolating robust high-redshift sources (see Figure 2 of Kriek et al. 2010 for actual measurements at $z > 0.5$). Due to our extraordinarily deep optical data, these objects must either then be severely reddened in the rest-frame ultraviolet or significantly affected by photometric scatter in order to be picked up by our selection criteria. However, we recognize there may be the potential for some contamination from rare sources with extreme emission line equivalent widths (e.g., Taniguchi et al. 2010; Atek et al. 2011; Brammer et al. 2013) or with other sharp spectral features that can mimic the presence of a Lyman break (Hayes et al. 2012). The possible effects both types of contaminants are discussed further in the context of our contamination simulations (Section 3.3.3).

3.3.2 Optical non-detection criteria

Applying a rigorous set of optical non-detection criteria is key to obtaining a clean sample of high-redshift sources by removing the lower redshift contaminants we describe above, as we expect all intrinsic flux from true high-redshift sources to be nearly extinguished by neutral Hydrogen at these wavelengths (Madau 1995). Here we adopt a slightly modified version of the criteria used in Bouwens et al. (2011) to eliminate sources with marginal optical detections from our selections.

The criteria we apply are as follows: (1) The measured flux in each filter shortward of the dropout

filter is less than 2.0σ. For the z-drops, this includes B_{435}, V_{606}, and i_{775}; for the Y-drops, we add z_{850}. (2) No more than one of the filters listed above shows a detection above 1.5σ. (3) To effectively add all the optical data, we finally require χ^2_{opt} [2] must be less than a threshold value, depending on the observed magnitude of the source. We compute this value using both our standard $0.30''$ diameter circular apertures, and a smaller $0.21''$ aperture, to rule out the most compact contaminants. At or below the 5σ limit of $m_{AB} = 29.5$ (in uncorrected, aperture magnitudes), we adopt a χ^2_{opt} upper limit of 2.5, while at the 10σ limit of $m_{AB} = 28.7$, we relax this to limit 5.0. A linear interpolation is used to determine the limit for magnitudes between the 5 and 10σ level.

3.3.3 Contamination simulations and the adopted UDF12 color-color selection

To estimate the number of contaminants we expect, we utilized the excellent HST photometry for objects at $25.0 < H_{160} < 27.0$ (as measured in our $0.5''$ diameter apertures) in the UDF. As we can robustly rule out the presence of a Balmer break at this depth, we selected, as our base color distribution of contaminants, all sources in this magnitude range that displayed at least one optical detection. The key assumption in our simulations is that the color distribution of these potential contaminants is unchanged as one moves down to the fainter magnitudes, where the majority of our dropout galaxies lie. If the relative number of strong emission line galaxies which mimick sharp spectral breaks (e.g., Atek et al. 2011) increases significantly toward faint magnitudes, our assumption may fail. However, such sources are surely rare and considering the color trend in this magnitude range, we see no evidence of such an effect. For our sample at $25.00 < H_{160} < 25.25$, the median $z_{850} - Y_{105}$, $Y_{105} - J_{125}$, and $J_{125} - H_{160}$ colors are 0.45, 0.31, and 0.31, respectively. At $26.75 < H_{160} < 27.00$, these three colors show even less extreme median colors of 0.32, 0.17, and 0.15.

We then create an array of synthetic sources, matched to the actual number of observed sources in the UDF in bins of 0.1 magnitudes. To get an accurate representation of sources intrinsically below our detection limit that have some chance of being scattered upwards into detection, we extrapolate the number counts beyond $H_{160} = 28.7$ (equivalent to a source at 10.0σ) as a function of magnitude via a power law down to sources intrinsically as faint as 1.0σ. The colors of these synthetic sources are chosen to obey the same color distribution as the brighter contaminant population described above, but noise consistent with their synthetic magnitudes is then added. These sources are then subject to the same optical non-detection criteria described above, but the colors cuts in $z_{850} - Y_{105}$ and $Y_{105} - J_{125}$ ($Y_{105} - J_{125}$ and $J_{125} - H_{160}$) for z-drops (Y-drops) are varied in steps of 0.05 as shown in Figure 3.1. To create these plots, we repeated the simulations for $N = 1000$ UDF fields.

[2] defined as $\chi^2_{opt} = \Sigma_i sign(f_i)(f_i/\sigma_i)^2$, where the i index runs across B_{435}, V_{606}, and i_{775} for z-drops; additionally i_{814} where available, and z_{850} for Y-drops

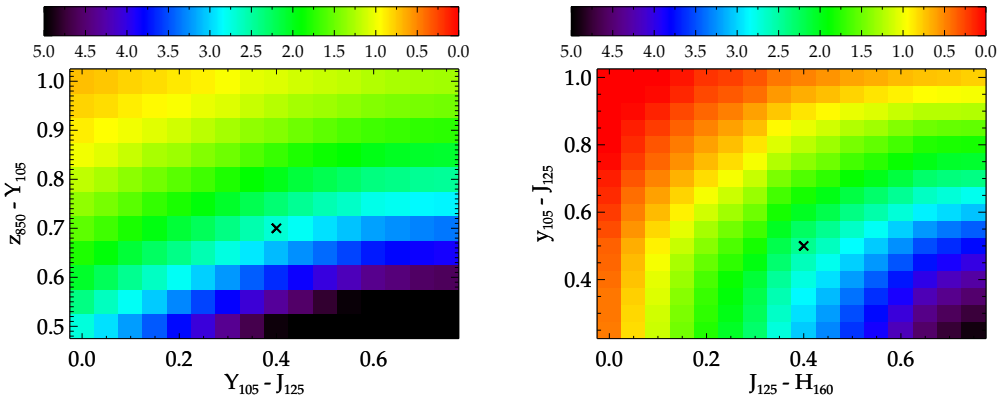

Figure 3.1 Left: Number of z_{850}-drop contaminants per UDF12 field as a function of the color cuts in $z_{850} - Y_{105}$ and $Y_{105} - J_{125}$. We assume that these contaminants obey the same intrinsic color distribution as UDF12 objects with $25.0 < H_{160} < 27.0$, as described in §3.3. The selection criteria are defined such that the $z_{850} - Y_{105}$ must be greater than the value on the y-axis to be selected, and the$Y_{105} - J_{125}$ less than the value on the x-axis. Right: As left, but for Y_{105}-drops. Our chosen cuts are marked by the black $'$x$'$ in each figure. We refer the reader to Figure 3.3 for a visualization of our final cuts.

Clearly, the most robust constraint on eliminating contaminants comes from requiring a large break in the bluer color for each sample, but gains are also made by limiting the color longward of the break to relatively blue values. Provided with these estimates, we chose to implement the color selection criteria as shown in Figure 3.1:

$$z_{850} - Y_{105} > 0.7 \tag{3.1}$$

$$Y_{105} - J_{125} < 0.4 \tag{3.2}$$

At $z \sim 8$, we use

$$Y_{105} - J_{125} > 0.5 \tag{3.3}$$

$$J_{125} - H_{160} < 0.4 \tag{3.4}$$

This leads to a selection for z-drops broadly within the redshift range $6.2 < z < 7.3$. For the $z \simeq 8$ study, we use our new ultra-deep WFC3 Y_{105} as the dropout filter, which leads to a sample spanning the redshift range $7.3 < z < 8.5$. A discussion of more distant sources in the UDF is provided by Ellis et al. (2013).

Finally, to ensure our sources are robust, we demand a detection significance of 3.5σ in the

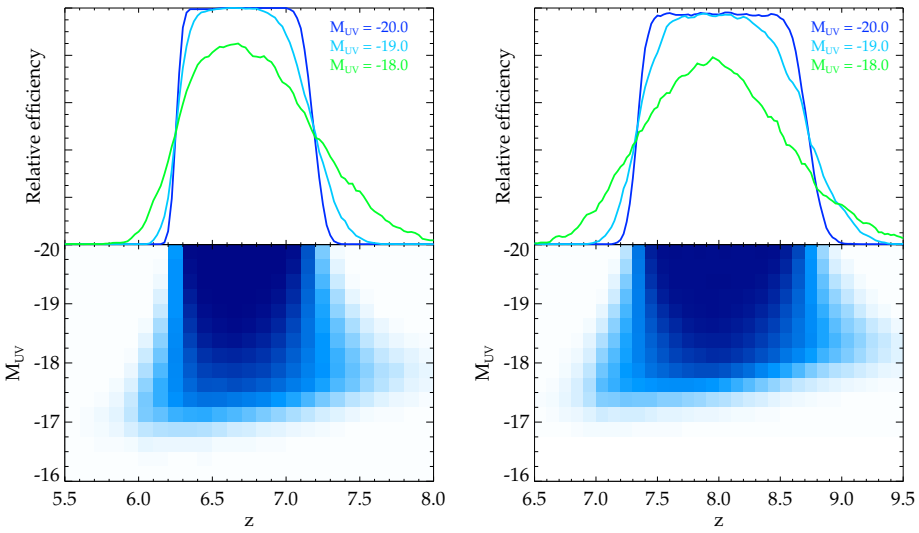

Figure 3.2 Left: Selection function for z_{850}-drop galaxies in the UDF, as a function of $M_{\rm UV}$ and redshift, constructed using the simulations discussed in §4.1. We have assumed that these galaxies display no Lyman α in emission. Even at bright magnitudes, maximum efficiency is only ∼0.65 due to the area subtended by other objects and our strict optical non-detection criteria, which result in a small fraction of true high-redshift sources being excluded. Right: Equivalent selection function for Y_{105}-drops.

filter immediately longward of the Lyman break (Y_{105} for our z-drops, J_{125} for our Y-drops, and a similarly robust detection in one further WFC3 filter at longer wavelengths.

These selection criteria are designed to provide as large a sample of galaxies as possible above redshift 6.5, while minimizing the effect of contamination. We plot selection functions for both z-drops and Y-drops in Figure 3.2 (see Section 3.4.1 for details on the selection function simulation). At bright magnitudes of $J_{140} < 27.5$, our z-drop color cuts provide a nearly complete census of star-forming galaxies between $6.30 < z < 7.15$, while the Y-drop cuts do the same between $7.35 < z < 8.60$.

Due to our strict criterion for optical non-detection, and the area subtended by other sources in UDF12, our maximum selection efficiency does not exceed $\sim 65\%$. For both our z- and Y-drop selections, 22% of the area is excluded due to objects occupying the image. For the more luminous z-drops, a further 13% of the area is excluded due to our optical exclusion criteria. As we impose more stringent criteria on the fainter sources, our optical criteria reject 21% of the areal coverage for our $z \sim 7$ search. For our $z \sim 8$ search criteria, the optical exclusion criteria reject 16% of the area at the bright end and 24% at the faint end.

Extending our $Y_{105} - J_{125}$ color cut for z-drops to 0.5 would only add an extra ~ 0.1 in redshift space to our selection function, as the color tracks are rapidly departing from our selection window,

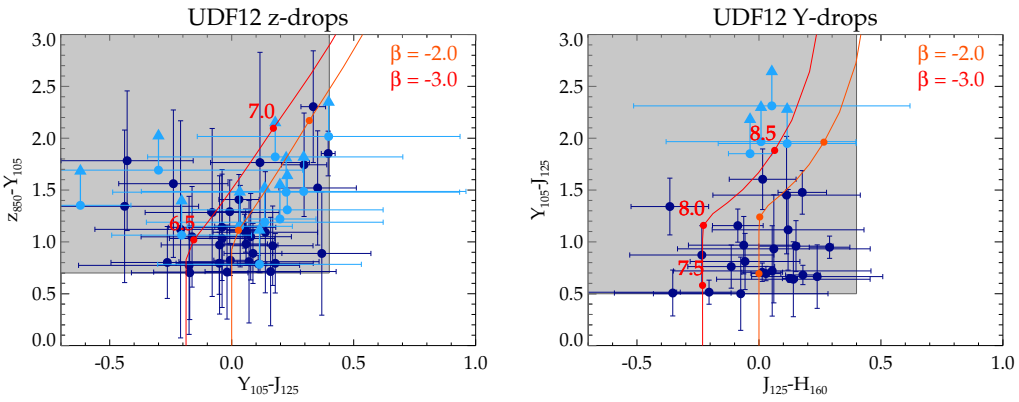

Figure 3.3 Color-color diagram of galaxies selected as z_{850}-drops (left) and Y_{105}-drops (right). Red and orange curves show the tracks of synthetic high-redshift galaxies for various UV continuum slopes β. Light blue points denote 1-σ upper limits.

as can be seen in Figure 3.3 This would additionally add an extra 0.3 expected contaminants. Combined with the concern that our new Y_{105} data is actually deeper than the existing z_{850} data, and that the primary contaminants themselves are intrinsically red, we opted for this conservative $Y_{105} - J_{125}$ color cut for our z-drop sample. Similarly adding an extra 0.1 mag to our $J_{125} - H_{160}$ limit for Y-drops is expected to add ~ 0.4 contaminants. As can be seen from the Y-drop color-color plot in Figure 3.3, the density of Y-drops with $J_{125} - H_{160}$ colors this red is quite low, so we chose to truncate the selection at $J_{125} - H_{160} < 0.4$, to limit the contamination. Adopting these cuts and all of our previously discussed selection criteria, we expect 2.79 and 1.42 contaminants per UDF field for z-drops and Y-drops, respectively.

We include candidate lists and photometry for our final selection of z-drops and Y-drops in Tables 3.2 and 3.3, respectively, and color-color plots in Figure 3.3. In total, we select 47 z-drops, and 27 Y-drops, of which 20 and 9 were only identified using our new UDF12 data. The vast majority consist of single components in the WFC3 imaging. We detect a single Y-drop with two components separated at only 0.4″, UDF12-3764-6015. The aperture photometry of the main component is 1.2 magnitudes brighter than the secondary component, and the two are considered as a single object in our later luminosity function analysis.

There are an additional 4 closely-spaced pairs in our sample. We detect 1 pair of z-drops, UDF12-3983-6189 and UDF12-3989-6189, separated by only 0.8″. There are two additional pairs of Y-drops, UDF12-4474-6450 and UDF12-4470-6443, separated by 0.9″, and UDF12-4314-6285 and UDF12-4309-6277, separated by 1.0″. This second pair is also part of a larger association of Y-drops in our sample, consisting of 5 candidates all within a separation of $< 9.0''$ (or 44 kpc at $z \sim 8$).

The final pair consists of a z-drop, UDF12-4036-8022, and a Y-drop, UDF12-4033-8026, so it is unlikely that these are physically related. Placing 47 z-drops and 27 Y-drops in the UDF at random,

we find a z-drop/Y-drop pair at $d < 1.0''$ 23% of the time, so such serendipitous alignment is not unreasonable. The significant difference in photometry (and thus photometric redshift) supports this case: UDF12-4036-8022 has $Y_{105} - J_{125} = 0.0$, while UDF12-4033-8026 shows $Y_{105} - J_{125} = 0.9$.

Table 3.2. UDF12 z-drops $6.2 < z < 7.3$

ID	RA	Dec	z_{850LP}	Y_{105W}	J_{125W}	J_{140W}	H_{160W}	References
UDF12-3746-6328	3:32:37.46	-27:46:32.8	28.4 ± 0.1	27.6 ± 0.1[a]	27.5 ± 0.1[a]	27.4 ± 0.1[a]	27.3 ± 0.1[a]	1,3,9
UDF12-4256-7314	3:32:42.56	-27:47:31.4	30.4 ± 0.7	28.1 ± 0.1[a]	27.8 ± 0.1[a]	27.8 ± 0.1[a]	27.7 ± 0.1[a]	1,2,3,4,5,7,10
UDF12-4219-6278	3:32:42.19	-27:46:27.8	29.2 ± 0.2	28.1 ± 0.1[a]	28.1 ± 0.1	28.0 ± 0.1	28.1 ± 0.1[a]	1,3,4,7,9,10
UDF12-3677-7536	3:32:36.77	-27:47:53.6	29.0 ± 0.2	28.2 ± 0.1[a]	28.2 ± 0.1	28.3 ± 0.1	28.2 ± 0.1[a]	1,2,3,4,7,9,10
UDF12-3744-6513	3:32:37.44	-27:46:51.3	29.5 ± 0.2	28.4 ± 0.1[a]	28.3 ± 0.1	28.5 ± 0.1	28.5 ± 0.1	1,2,3,4,5,7,9,10
UDF12-4105-7156	3:32:41.05	-27:47:15.6	30.4 ± 0.7	28.7 ± 0.1	28.4 ± 0.1	28.3 ± 0.1	28.4 ± 0.1	1,2,3,5,10
UDF12-3958-6565	3:32:39.58	-27:46:56.5	29.8 ± 0.3	28.4 ± 0.1[a]	28.4 ± 0.1	28.4 ± 0.1	28.4 ± 0.1	1,2,3,5,7,9,10
UDF12-3638-7162	3:32:36.38	-27:47:16.2	29.5 ± 0.2	28.5 ± 0.1[a]	28.5 ± 0.1	28.4 ± 0.1	28.5 ± 0.1	1,2,3,4,5,7,9,10
UDF12-4057-6436	3:32:40.57	-27:46:43.6	29.9 ± 0.4	28.6 ± 0.1	28.6 ± 0.1	28.5 ± 0.1	28.7 ± 0.1	1,2,3,4,5,7,9,10
UDF12-4431-6452	3:32:44.31	-27:46:45.2	29.6 ± 0.3	28.7 ± 0.1	28.6 ± 0.1	28.7 ± 0.1	28.9 ± 0.2	1,7,9,10
UDF12-4160-7045	3:32:41.60	-27:47:04.5	30.0 ± 0.5	28.8 ± 0.1	28.8 ± 0.1	28.7 ± 0.1	28.8 ± 0.1	7,9,10
UDF12-4268-7073	3:32:42.68	-27:47:07.3	29.9 ± 0.3	29.1 ± 0.1	28.9 ± 0.1	28.9 ± 0.2	28.9 ± 0.1	10
UDF12-3313-6545	3:32:33.13	-27:46:54.5	< 31.3	29.3 ± 0.1	28.9 ± 0.1	28.6 ± 0.1	29.0 ± 0.1	1,6,7,9,10
UDF12-3402-6504	3:32:34.02	-27:46:50.4	30.8 ± 0.7	29.3 ± 0.1	28.9 ± 0.1	29.0 ± 0.1	29.2 ± 0.2	7,10
UDF12-4182-6112	3:32:41.82	-27:46:11.2	30.3 ± 0.5	29.3 ± 0.1	29.1 ± 0.1	29.0 ± 0.1	28.9 ± 0.1	3,4,5,7,9,10
UDF12-3734-7192	3:32:37.34	-27:47:19.2	30.3 ± 0.5	29.3 ± 0.1	29.2 ± 0.2	29.5 ± 0.2	29.5 ± 0.2	10
UDF12-4239-6243	3:32:42.39	-27:46:24.3	30.0 ± 0.3	29.2 ± 0.1	29.3 ± 0.2	28.9 ± 0.1	29.1 ± 0.2	3,5,7,11
UDF12-3989-6189	3:32:39.89	-27:46:18.9	30.5 ± 0.8	29.4 ± 0.1	29.3 ± 0.2	29.5 ± 0.2	29.5 ± 0.2	1,10

Table 3.2—Continued

ID	RA	Dec	z_{850LP}	Y_{105W}	J_{125W}	J_{140W}	H_{160W}	References
UDF12-4068-6498	3:32:40.68	-27:46:49.8	30.6 ± 0.8	29.7 ± 0.1	29.4 ± 0.2	29.4 ± 0.2	29.6 ± 0.2	10
UDF12-3853-7519	3:32:38.53	-27:47:51.9	< 31.4	29.6 ± 0.1	29.4 ± 0.2	29.4 ± 0.2	29.7 ± 0.3	2,7,10
UDF12-4472-6362	3:32:44.72	-27:46:36.2	30.8 ± 1.0	29.0 ± 0.1	29.4 ± 0.3	28.8 ± 0.1	28.9 ± 0.1	10
UDF12-3983-6189	3:32:39.83	-27:46:18.9	30.0 ± 0.4	29.2 ± 0.1	29.4 ± 0.2	29.7 ± 0.3	29.4 ± 0.1	1,11
UDF12-3736-6245	3:32:37.36	-27:46:24.5	30.6 ± 0.7	29.4 ± 0.1	29.5 ± 0.2	29.5 ± 0.2	29.6 ± 0.2	7,10
UDF12-3456-6493	3:32:34.56	-27:46:49.3	31.4 ± 3.9	29.6 ± 0.1	29.5 ± 0.2	29.3 ± 0.1	29.2 ± 0.1	7,10
UDF12-3859-6521	3:32:38.59	-27:46:52.1	30.4 ± 0.6	29.3 ± 0.1	29.5 ± 0.2	29.9 ± 0.3	29.5 ± 0.2	7,10
UDF12-4384-6311	3:32:43.84	-27:46:31.1	< 30.9	29.8 ± 0.2	29.6 ± 0.3	29.5 ± 0.2	29.9 ± 0.4	10
UDF12-3755-6019	3:32:37.55	-27:46:01.9	< 31.4	29.9 ± 0.2	29.6 ± 0.2	29.9 ± 0.4	29.6 ± 0.2	7,10
UDF12-3975-7451	3:32:39.75	-27:47:45.1	30.9 ± 1.1	29.4 ± 0.1	29.6 ± 0.2	29.2 ± 0.2	29.3 ± 0.2	7,10
UDF12-4201-7074	3:32:42.01	-27:47:07.4	30.6 ± 1.0	29.6 ± 0.1	29.6 ± 0.2	30.0 ± 0.4	29.6 ± 0.2	10
UDF12-4037-6560	3:32:40.37	-27:46:56.0	< 31.3	29.9 ± 0.2	29.6 ± 0.2	30.1 ± 0.4	30.1 ± 0.3	7,10
UDF12-4426-6367	3:32:44.26	-27:46:36.7	30.8 ± 1.4	29.6 ± 0.1	29.6 ± 0.3	29.7 ± 0.3	29.5 ± 0.2	-
UDF12-3909-6092	3:32:39.09	-27:46:09.2	30.2 ± 0.6	29.5 ± 0.1	29.7 ± 0.2	30.3 ± 0.4	29.9 ± 0.3	10
UDF12-4143-7041	3:32:41.43	-27:47:04.1	30.6 ± 0.7	29.9 ± 0.2	29.8 ± 0.2	30.2 ± 0.4	30.0 ± 0.4	10
UDF12-3696-5536	3:32:36.96	-27:45:53.6	30.5 ± 0.5	29.7 ± 0.2	29.8 ± 0.3	29.3 ± 0.2	29.9 ± 0.3	7,10
UDF12-3897-8116	3:32:38.97	-27:48:11.6	30.7 ± 0.8	29.9 ± 0.2	29.8 ± 0.3	30.0 ± 0.4	29.8 ± 0.3	10
UDF12-4288-6261	3:32:42.88	-27:46:26.1	30.7 ± 1.0	29.7 ± 0.2	29.8 ± 0.2	30.0 ± 0.3	30.5 ± 0.7	10

Table 3.2—Continued

ID	RA	Dec	z_{850LP}	Y_{105W}	J_{125W}	J_{140W}	H_{160W}	References
UDF12-3817-7327	3:32:38.17	-27:47:32.7	< 30.5	30.0 ± 0.2	29.8 ± 0.3	30.0 ± 0.4	30.3 ± 0.6	11
UDF12-4379-6510	3:32:43.79	-27:46:51.0	30.8 ± 1.2	29.4 ± 0.1	29.9 ± 0.3	29.8 ± 0.3	29.8 ± 0.3	10
UDF12-3691-6517	3:32:36.91	-27:46:51.7	< 30.7	30.0 ± 0.2	29.9 ± 0.3	29.7 ± 0.3	30.2 ± 0.4	8,10
UDF12-4071-7347	3:32:40.71	-27:47:34.7	< 31.4	29.7 ± 0.2	30.0 ± 0.4	29.4 ± 0.2	30.0 ± 0.6	7,10
UDF12-4036-8022	3:32:40.36	-27:48:02.2	< 31.2	30.1 ± 0.2	30.0 ± 0.4	29.9 ± 0.3	30.7 ± 1.3	3,7,10
UDF12-3922-6149	3:32:39.22	-27:46:14.9	30.8 ± 1.0	30.0 ± 0.2	30.2 ± 0.5	30.6 ± 0.6	30.1 ± 0.3	10
UDF12-4245-6534	3:32:42.45	-27:46:53.4	< 30.9	30.3 ± 0.2	30.2 ± 0.4	29.5 ± 0.2	29.6 ± 0.2	11
UDF12-4263-6416	3:32:42.63	-27:46:41.6	31.1 ± 3.2	30.0 ± 0.2	30.2 ± 0.3	30.3 ± 0.5	30.1 ± 0.4	10
UDF12-4090-6084	3:32:40.90	-27:46:08.4	< 31.3	30.2 ± 0.3	30.5 ± 0.6	30.3 ± 0.4	29.8 ± 0.3	11
UDF12-4019-6190	3:32:40.19	-27:46:19.0	< 31.0	29.9 ± 0.2	30.5 ± 0.6	29.9 ± 0.3	29.8 ± 0.2	10

Note. — z-drop photometry. All magnitudes listed are measured in the 70% inclusive aperture sizes listed in Section 3.2.4 and not corrected to total here. We also note that errors in magnitude space become significantly asymmetric below $\sim 10\sigma$. We have plotted the larger error wherever appropriate. Upper limits are 1σ. References are (1) McLure et al. (2010), (2) Oesch et al. (2010), (3) Finkelstein et al. (2010), (4) Wilkins et al. (2011), (5) Yan et al. (2010), (6) Lorenzoni et al. (2011), (7) Bouwens et al. (2011), (8) Bouwens et al. (2011) potential, (9) McLure et al. (2011), (10) McLure et al. (2013) robust, (11) McLure et al. (2013) potential

[a]Photometric errors $< 10\%$.

Table 3.3. UDF12 Y-drops $7.3 < z < 8.5$

ID	RA	Dec	Y_{105W}	J_{125W}	J_{140W}	H_{160W}	References
UDF12-3880-7072	3:32:38.80	-27:47:07.2	28.0 ± 0.1[a]	27.3 ± 0.1[a]	27.3 ± 0.1[a]	27.2 ± 0.1[a]	1,2,3,4,5,7,9,10
UDF12-4470-6443	3:32:44.70	-27:46:44.3	28.5 ± 0.1	27.8 ± 0.1[a]	27.8 ± 0.1[a]	27.8 ± 0.1[a]	1,2,3,5,7,9,10
UDF12-3952-7174	3:32:39.52	-27:47:17.4	29.3 ± 0.1	28.3 ± 0.1	28.2 ± 0.1	28.0 ± 0.1	1,2,3,5,7,9,10
UDF12-4314-6285	3:32:43.14	-27:46:28.5	29.0 ± 0.1	28.3 ± 0.1	28.2 ± 0.1	28.1 ± 0.1[a]	1,2,3,4,5,7,9,11
UDF12-3722-8061	3:32:37.22	-27:48:06.1	29.0 ± 0.1	28.3 ± 0.1	28.3 ± 0.1	28.3 ± 0.1	1,2,3,5,7,9,10
UDF12-3813-5540	3:32:38.13	-27:45:54.0	30.1 ± 0.2	28.6 ± 0.1	28.5 ± 0.1	28.4 ± 0.1	1,3,5,6,7,9,10
UDF12-3780-6001	3:32:37.80	-27:46:00.1	29.8 ± 0.2	28.6 ± 0.1	28.6 ± 0.1	28.7 ± 0.1	1,3,5,6,7,10
UDF12-3764-6015	3:32:37.64	-27:46:01.5	30.5 ± 0.3	28.9 ± 0.1	28.9 ± 0.1	28.8 ± 0.1	1,3,5,7,10
UDF12-3939-7040	3:32:39.39	-27:47:04.0	30.0 ± 0.2	29.1 ± 0.1	29.1 ± 0.1	28.9 ± 0.1	10
UDF12-4474-6450	3:32:44.74	-27:46:45.0	29.7 ± 0.2	29.0 ± 0.1	29.1 ± 0.2	29.1 ± 0.1	1,2,3,5,7,10
UDF12-4309-6277	3:32:43.09	-27:46:27.7	30.3 ± 0.3	28.9 ± 0.1	29.4 ± 0.2	29.3 ± 0.1	1,3,5,7,11
UDF12-4309-6260	3:32:43.09	-27:46:26.0	30.1 ± 0.2	29.3 ± 0.2	28.9 ± 0.1	29.3 ± 0.2	7,10
UDF12-3463-6472	3:32:34.63	-27:46:47.2	30.3 ± 0.2	29.6 ± 0.2	29.3 ± 0.2	29.4 ± 0.2	7
UDF12-3551-7443	3:32:35.51	-27:47:44.3	30.7 ± 0.4	29.5 ± 0.2	29.9 ± 0.4	29.4 ± 0.3	7,11
UDF12-4336-6203	3:32:43.36	-27:46:20.3	< 31.8	29.5 ± 0.2	29.6 ± 0.2	29.4 ± 0.2	-
UDF12-4240-6550	3:32:42.40	-27:46:55.0	30.4 ± 0.3	29.4 ± 0.1	29.7 ± 0.2	29.5 ± 0.2	7,10
UDF12-4033-8026	3:32:40.33	-27:48:02.6	30.1 ± 0.3	29.3 ± 0.2	29.6 ± 0.3	29.5 ± 0.3	3,7,10
UDF12-4308-6242	3:32:43.08	-27:46:24.2	30.4 ± 0.3	29.7 ± 0.3	30.0 ± 0.4	29.6 ± 0.2	7,10

Table 3.3—Continued

ID	RA	Dec	Y_{105W}	J_{125W}	J_{140W}	H_{160W}	References
UDF12-3931-6180	3:32:39.31	-27:46:18.0	29.8 ± 0.2	29.3 ± 0.2	29.3 ± 0.1	29.6 ± 0.2	10
UDF12-3934-7256	3:32:39.34	-27:47:25.6	31.2 ± 0.7	29.8 ± 0.3	30.0 ± 0.3	29.7 ± 0.2	7,11
UDF12-3881-6343	3:32:38.81	-27:46:34.3	30.6 ± 0.4	29.9 ± 0.4	30.0 ± 0.4	29.8 ± 0.3	11
UDF12-3681-6421	3:32:36.81	-27:46:42.1	< 31.4	30.0 ± 0.4	30.0 ± 0.4	29.8 ± 0.3	7,11
UDF12-4294-6560	3:32:42.94	-27:46:56.0	30.8 ± 0.6	29.9 ± 0.3	30.5 ± 0.7	29.9 ± 0.3	11
UDF12-3920-6322	3:32:39.20	-27:46:32.2	< 31.9	29.9 ± 0.3	29.7 ± 0.3	29.9 ± 0.3	10
UDF12-3858-6150	3:32:38.58	-27:46:15.0	30.3 ± 0.3	29.8 ± 0.3	30.3 ± 0.4	29.9 ± 0.3	11
UDF12-4344-6547	3:32:43.44	-27:46:54.7	< 31.9	30.0 ± 0.3	30.1 ± 0.4	30.0 ± 0.3	10
UDF12-4101-7216	3:32:41.01	-27:47:21.6	30.4 ± 0.2	29.9 ± 0.3	30.0 ± 0.3	30.9 ± 0.8	10

Note. — Y-drop photometry. All magnitudes listed are measured in the 70% inclusive aperture sizes listed in Section 3.2.4 and not corrected to total here. We also note that errors in magnitude space become significantly asymmetric below $\sim 10\sigma$. We have plotted the larger error wherever appropriate. Upper limits are 1σ. References are (1) McLure et al. (2010), (2) Oesch et al. (2010), (3) Finkelstein et al. (2010), (4) Wilkins et al. (2011), (5) Yan et al. (2010), (6) Lorenzoni et al. (2011), (7) Bouwens et al. (2011), (8) Bouwens et al. (2011) potential, (9) McLure et al. (2011), (10) McLure et al. (2013) robust, (11) McLure et al. (2013) potential

[a]Photometric errors $< 10\%$.

3.3.4 UDF-P1 and UDF-P2

The two UDF parallel fields, observed as part of the UDF05 (GO10632; PI: Stiavelli) and UDF09 (GO 11563; PI: Illingworth) campaigns comprise the two data sets most similar to our UDF12 dataset, though the depths are ∼0.5 mag shallower. As such, we utilize the same color-color criteria determined for our UDF12 selections. Because the optical data is shallower, we tighten our χ^2_{opt} upper limit for selection to 1.5 (3.0) at the 5σ (10σ) aperture magnitude limit in each field. We utilize the ultradeep 128 orbit z_{814} ACS data taken in parallel to our main UDF12 program, which covers roughly 70 % of the P2 WFC3/IR field. For z-drops within this area we impose an additional criterion of $z_{814} - Y_{105} > 2.0$ OR $f_{814}/\sigma_{814} < 2.0$. This extra cut reinforces the requirement for a sharp spectral break and more fully utilizes our deep i_{814} data over the P2 field. From our synthetic spectral models at $z = 6.2$, where our selection function begins to yield sources, we expect an $i_{814} - Y_{105}$ color of 2.0, which increases further with increasing redshift. The $f_{814}/\sigma_{814} < 2.0$ criterion allows sources to pass our cuts in the case where the candidate is too faint to robustly establish a 2 magnitude break between i_{814} and Y_{105}. In practice, this only occurs in the CANDELS field (described below), but we consider it advantageous to keep uniform selection criteria where possible.

3.3.5 ERS

For the ERS dataset, the Y_{098} filter was utilized, so we take care to alter our selection criteria accordingly. We chose to use the criteria derived by Bouwens et al. (2011), at $z \sim 7$, which, despite the different filter selection, produce a selection function that probes a similar range in redshift. These criteria are (1) $z_{850} - J_{125} > 0.9$, (2) $z_{850} - J_{125} > 0.8 + 1.1(J_{125} - H_{160})$, and (3) $z_{850} - J_{125} > 0.4 + 1.1(Y_{098} - J_{125})$. At $z \sim 8$, we adopt the Bouwens et al. (2011) $Y_{098} - J_{125}$ lower limit of 1.25, but chose the same $J_{125} - H_{160} < 0.4$ cut we use for the UDF fields, to ensure the selection functions for our analysis are as homogeneous as possible.

3.3.6 CANDELS

For the CANDELS field, we use the same criteria as adopted for UDF-P34, including the addition of the z_{814} criteria. Due to the varying depth of the data, we divide the CANDELS field into 3 distinct subregions when performing our analysis. The first region consists of the immediate area around the HUDF that is covered by ACS optical imaging taken as part of the HUDF04 (Beckwith et al. 2006) campaign, but falls outside the region probed by our UDF12 campaign, due to the smaller field of view of the WFC3 instrument. Here, the optical data is nearly a full 2 magnitudes deeper than the available IR data, resulting in negligible contamination rates in our sample.

The remaining sample is further divided into an East and West region. The East and West

regions have identical depth in the ACS data from the GOODS program, and in the J_{125} and H_{160} filters, but the Y_{105} depth in the West region is approximately 0.4 magnitudes shallower than that of the East. For the purposes of contamination and completeness simulations, we separate these two fields in order to properly account for the variation in depth.

3.4 The Luminosity Function at $z \sim 7$ and ~ 8 from UDF12 data

With our candidate selection completed, we now turn to evaluating the $z \simeq 7$ and 8 luminosity functions. The key issue in converting numbers of sources of known absolute magnitude into a comoving density of luminosities is, of course, the redshift-dependent selection function which defines the visibility as a function of apparent magnitude as well as the optimum algorithm for fitting a function to the resulting number density. We now introduce the algorithms we will utilize for both of these critical steps.

3.4.1 Simulations

We first describe how we calculate the selection function used to determine the effective volumes for our luminosity function calculations.

To create synthetic fluxes for galaxies in our simulations, we assume an input UV slope $\beta = -2.0$. This choice is motivated by the results of Dunlop et al. (2013), who find no conclusive evidence for an intrinsic scatter in β from this value at $z \sim 7-8$ in the UDF12 field (cf. Wilkins et al. 2011; Bouwens et al. 2012b; Finkelstein et al. 2012b). We also assume that these galaxies display no Lyman α in emission, motivated by the rarity of detectable emission in recent studies (e.g., Pentericci et al. 2011; Schenker et al. 2012; Ono et al. 2012). Fluxes are computed by applying intergalactic extinction from Meiksin (2006) to a Bruzual and Charlot (Bruzual & Charlot 2003) synthetic spectrum consistent with this value of β.

We parameterize our selection efficiency, $S(m, z)$, as a function of redshift and the magnitude for the filter (or filters for the UDF12 data) used to determine the rest-frame UV magnitude. In each field, we determine the shape of the selection function first using numerical simulations only, which take into account the limiting magnitudes in each filter for point sources. In steps of 0.01 in redshift, and 0.05 in magnitude, we take the synthetic flux from our galaxy model, perturb it by the appropriate noise, and apply our color-color selection criteria. At each step of z, m, and for each field, we perform this $N = 1000$ times to construct a complete surface for our selection function. We define the selection function produced by this process as $S_{numeric}(m, z)$.

However, this selection function is only appropriate if these galaxies are point sources in otherwise

blank fields, which is certainly not the case. The marginally resolved nature of our targets will result in higher incompleteness levels at faint magnitudes than for point sources. It is imperative to correct for this effect, as a varying completeness correction can produce large differences in the faint end slope (Grazian et al. 2012). To account for this incompleteness, as well as that caused by area in the images obscured by brighter sources, we rely on inserting synthetic galaxy images into our mosaics for each field. We generate a synthetic template with a Sersic index of 1.5, consistent with a stack of LBGs at $z \sim 4$ (Oesch et al. 2010). The template image has a half-light radius of 0.35 kpc, motivated by the results of Ono et al. (2013), who perform a detailed measurement of the sizes of UDF12 high-redshift candidates. This template is then convolved with the point spread function for each filter, multiplied by the appropriate model flux as described above, and inserted into the image in a random location. After inserting $N = 1000$ non-overlapping sources, we run the SExtractor program for object detection, and compute fluxes and errors in the same manner as for our science images. We perform this simulation at the peak of each of our selection functions in redshift space, in steps of 0.05 in magnitude. This peak efficiency at a given magnitude $\epsilon(m)$ is then used to normalize our selection function such that our total selection function used to compute effective volumes is given by $S_{total}(m, z) = S_{numeric}(m, z) \times \epsilon(m)$. The final selection functions for both z-zdrops and Y-drops in the UDF are presented in Figure 3.2.

3.4.2 Maximum Likelihood Luminosity Functions

Using the new UDF12 data and previous observations, we assemble dropout samples at $z \sim 7$ and ~ 8 in multiple fields. For each sample, we split the galaxy number counts into bins of width $\Delta M = 0.5$ in absolute magnitude M_{UV}. We use these binned galaxy number counts and our simulations of photometric scattering and low-redshift contaminants to determine the high-redshift stepwise maximum likelihood (SWML; Efstathiou et al. 1988) and Schechter (1976) galaxy luminosity functions $\Phi(M_{\mathrm{UV}})$ in units of Mpc^{-3} mag^{-1}.

3.4.2.1 Stepwise Maximum Likelihood Luminosity Function

The SWML luminosity function aims to jointly fit the binned galaxy abundance Φ_k in the k^{th} of N_{bin} magnitude bins. For each bin, the maximum likelihood values for Φ_k are determined by using the observed number of galaxies $n_{\mathrm{obs},k}$, the effective volume $V_{\mathrm{eff},k}$ for galaxies with intrinsic M_{UV} in the bin, and the probabilities $P_{i,j}$ for scattering galaxies with intrinsic M_{UV} in bin i into bin j owing to photometric noise and the number of low-redshift contaminants $n_{\mathrm{con},k}$ for the bin calculated as

described in §3.4.1. Given Φ_k, we construct the expected number of galaxies in each bin as

$$\begin{aligned} n_{\mathrm{exp},k} &= \Phi_k V_{\mathrm{eff},k} \left(1 - \sum_{i \neq k} P_{k,i}\right) \\ &+ \sum_{i \neq k} \Phi_i V_{\mathrm{eff},i} P_{i,k} \\ &+ n_{\mathrm{con},k}, \end{aligned} \tag{3.5}$$

where the summations run over N_{bin}. In practice, when using a bin width $\Delta M_{\mathrm{UV}} = 0.5$ galaxies do not scatter by more than one bin and the summations are trivial. We account for photometric scattering of sources into our faintest bin by a simple extrapolation of the luminosity function to yet fainter magnitudes.

To fit the shape of our SWML, we can use the likelihood of observing $n_{\mathrm{obs},k}$ given the expected number $n_{\mathrm{exp},k}$:

$$p(n_{\mathrm{obs},k}|n_{\mathrm{exp},k}) = \left(\frac{n_{\mathrm{exp},k}}{\Sigma_j n_{\mathrm{exp},j}}\right)^{n_{\mathrm{obs},k}} \tag{3.6}$$

The SWML luminosity function Φ_k is determined by maximizing the product of these individual likelihoods across all bins, and across all fields. Photometric scatter correlates the individual Φ_k for each field, and the SWML values must therefore be determined simultaneously. This calculation amounts to an N_{bin}-parameter estimation problem, and we use the *MultiNest* nested sampling code for Bayesian inference problems (Feroz & Hobson 2008; Feroz et al. 2009) to maximize the Φ_k likelihoods.

To fit the overall normalization of our SWML, we sum $n_{\mathrm{obs},k}$ across all fields for each magnitude bin. Since we expect this quantity to be Poisson distributed, we can easily generate a posterior distribution of the normalization for each bin. To find our final posterior distribution, for the normalization, we multiply the posteriors generated in this manner across all bins.

The results of the SWML luminosity function calculation for redshift $z \sim 7$ are shown in Figure 3.4 and for redshift $z \sim 8$ in Figure 3.5. The data points indicate the maximum likelihood Φ_k at each magnitude for our sample taking into account all fields, while error bars indicate the smallest marginalized interval to encompass 68% of the likelihood for each bin.

3.4.2.2 Schechter Luminosity Functions

A determination of the Schechter (1976) luminosity function parameters is calculated by estimating the mean galaxy abundance in each bin as

$$\Phi_k = \frac{1}{\Delta M_{\mathrm{UV}}} \int_{M_{\mathrm{UV},k} - 0.5\Delta M_{\mathrm{UV}}}^{M_{\mathrm{UV},k} + 0.5\Delta M_{\mathrm{UV}}} \Phi(M) dM \tag{3.7}$$

Table 3.4. SWML determination of the $z \sim 7$ LF

$M_{\rm UV}$	log ϕ_k [Mpc^{-3} mag^{-1}]
-20.65	$-4.29^{+0.29}_{-0.28}$
-20.15	$-3.71^{+0.14}_{-0.10}$
-19.65	$-3.31^{+0.08}_{-0.10}$
-19.15	$-3.02^{+0.13}_{-0.06}$
-18.65	$-2.98^{+0.17}_{-0.23}$
-18.15	$-2.56^{+0.19}_{-0.06}$
-17.65	$-2.23^{+0.12}_{-0.09}$
-17.15	$-3.03^{+0.54}_{-2.34}$

Table 3.5. SWML determination of the $z \sim 8$ LF

$M_{\rm UV}$	log ϕ_k [Mpc^{-3} mag^{-1}]
-22.00	< 5.01
-21.50	$-5.02^{+0.44}_{-0.47}$
-21.00	$-4.28^{+0.16}_{-0.24}$
-20.50	$-4.15^{+0.12}_{-0.43}$
-20.00	$-3.54^{+0.17}_{-0.06}$
-19.50	$-3.34^{+0.15}_{-0.17}$
-19.00	$-2.97^{+0.09}_{-0.20}$
-18.50	$-2.91^{+0.14}_{-0.24}$
-18.00	$-2.61^{+0.18}_{-0.20}$
-17.50	$-2.57^{+0.25}_{-0.74}$

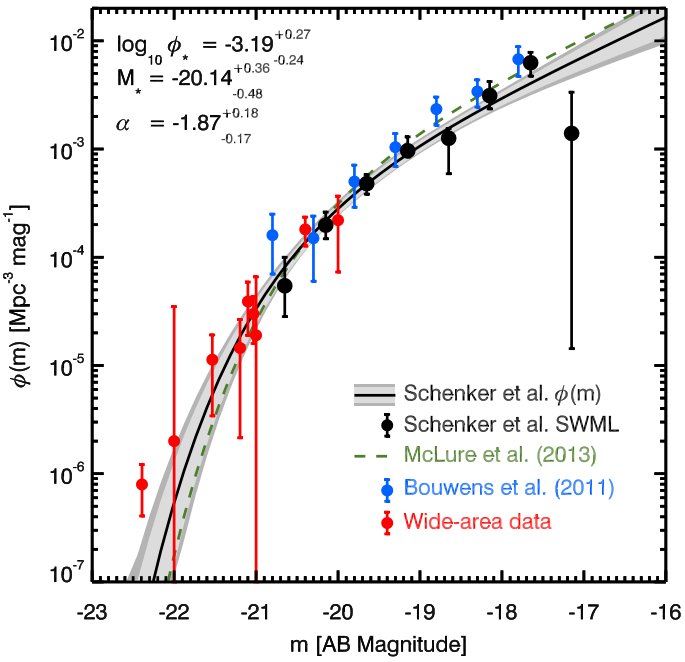

Figure 3.4 The luminosity function of star-forming galaxies at $z \sim 7$ from the z_{850}-drop sample. Black points were determined using the UDF12 data set and other HST data mentioned in this work. Red points denote wide area ground based data. The black line defines the maximum likelihood Schechter luminosity function and the shaded light grey region denotes the 68% confidence interval. The shaded dark grey region denotes the 68% confidence interval when errors from cosmic variance are included. The green dashed line denotes the fit of McLure et al. (2013).

and then using Equations 3.5 and 3.6 to calculate the likelihood of the fit parameters. The likelihoods of each binned sample in each field are multiplied. To improve constraints at the bright end at $z \sim 7$, when fitting the Schechter function parameters, we also include data from the ground-based surveys of Ouchi et al. (2009), Castellano et al. (2010), and Bowler et al. (2012). Incorporating the wide-area ground-based constraints is critical as even our wide area HST data only detects sources dimmer than $M_{\rm UV} \sim -21.0$, or approximately 1 magnitude brighter than M^*_{UV} at this redshift. As pointed out in Robertson (2010a), Bouwens et al. (2011), and Bradley et al. (2012a), there remains a large degeneracy between M^*_{UV} and the faint end slope, α without sufficient data at the bright end. These additional data are incorporated using the published data points and errors through a χ^2 likelihood, assuming the reported errors are Gaussian. The maximum likelihood Schechter function parameters are determined using *MultiNest* to conduct Bayesian inference.

The Schechter function fit results for redshift $z \sim 7$ are shown in Figure 3.4 and for $z \sim 8$ in Figure 3.5, with the maximum likelihood models shown as a black line. At $z \sim 7$, the best fit Schechter function parameters are $\log_{10}\phi_\star = -3.19^{+0.27}_{-0.24}\log_{10}\mathrm{Mpc}^{-3}\ \mathrm{mag}^{-1}$, $M_{\mathrm{UV},\star} = -20.14 \pm 0.4$, and $\alpha_{z\sim7} = -1.87^{+0.18}_{-0.17}$. The uncertainty range for each parameter reflects the smallest interval in

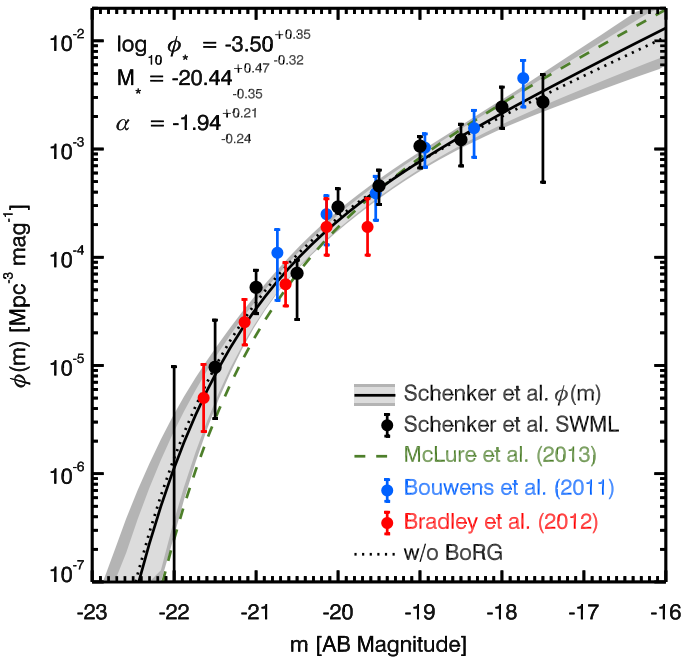

Figure 3.5 The luminosity function of star-forming galaxies at $z \sim 8$ from the Y_{105}-drop sample. Black points were determined using the UDF12 data set and other HST data mentioned in this work. Red points denote data from the Bradley et al. (2012a) analysis of the BoRG fields that increase the range in luminosity. The black line defines the maximum likelihood Schechter luminosity function and the shaded light grey region denotes the 68% confidence interval The shaded dark grey region includes the error contribution from cosmic variance. The green line denotes our fit when removing the BoRG dataponts; we note that our fit to the faint end slope is remarkably insensitive to their inclusion/exclusion. The green dashed line denotes the fit of McLure et al. (2013).

each marginalized distribution to encompass 68% of the posterior probability. At $z \sim 8$, the best fit Schechter function parameters are $\log_{10}\phi_\star = -3.50^{+0.35}_{-0.32}\log_{10}\mathrm{Mpc}^{-3}$ mag^{-1}, $M_{\mathrm{UV},\star} = -20.44^{+0.5}_{-0.4}$, and $\alpha_{z\sim8} = -1.94^{+0.21}_{-0.24}$. In Figures 3.4 and 3.5, the light grey shaded regions denote the inner 68% of the marginalized posterior distribution in galaxy abundance at each magnitude. The dark grey regions in each plot represent the 68% marginalized confidence intervals including potential error contrubitions from cosmic variance, as discussed in Section 3.4.2.3.

At $z \sim 8$, we also include a Schechter function fit excluding the Bradley et al. (2012a) BoRG data, denoted by the dotted black line. The best fit parameters are $\log_{10}\phi_\star = -3.47 \pm 0.39\mathrm{Mpc}^{-3}$ mag^{-1}, $M_{\mathrm{UV},\star} = -20.45 \pm 0.50$, and $\alpha_{z\sim8} = -1.87 \pm 0.25$. This results in nearly identical values for $\phi_\star$ and $M_{\mathrm{UV},\star}$, with a slightly shallower faint end slope and marginally larger error bars compared to the fit with the data included. Thus, even without the wide area data, we still find strong evidence for a steep value of α.

We caution the reader against an over-interpretation of the faintest bins in our luminosity functions. Although heating of the intergalactic medium during reionization is expected to suppress the

formation of dwarf galaxies below a characteristic halo mass (e.g., Wyithe & Loeb 2006; Muñoz & Loeb 2011), the density determinations of ϕ_k in our faintest bins are very sensitive both to upscattering of sources below the limit and completeness corrections. This is largely a result of being in a regime where the effective volume is rapidly changing as a function of magnitude. For example, simply dividing the number of observed sources, after correcting for the expected contamination, in our faintest $z \sim 7$ bin by the effective volume yields $\log_{10} \phi_k \sim -2.3$, which is much more in line with our best fit Schechter function parameters. Though we have made our best effort to quantify and account for corrections arising from finite size, scattering, and contamination, the situation remains difficult at the faintest reaches of the survey.

3.4.2.3 Cosmic Variance

Although we have not included the effects of cosmic variance in any of the parameter estimates given above, it is nonetheless useful to obtain some indication of its effect. To first order, cosmic variance is unlikely to have a major effect on one of the primary goals of this paper, namely an estimate of the faint end slope at $z \sim 7 - 8$. In the following, we therefore give an approximate calculation of the effective variance arising from large scale structure.

Density fluctuations owing to large scale modes can cause variations in the observed galaxy abundance beyond uncertainties arising from number counting statistics. Following Robertson (2010a), by using our best fit luminosity functions at $z \sim 7 - 8$, we can characterize these cosmic variance uncertainties for each field in our sample. We use the linear power spectrum calculated with the Eisenstein & Hu (1998) transfer function, conservatively assuming root-mean-squared density fluctuations in volumes of radius 8 h^{-1}Mpc of $\sigma_8 = 0.9$ at $z = 0$, to estimate the typical root-mean-squared density fluctuations in our survey fields at the redshifts of interest. To estimate the clustering bias of galaxies at these redshifts, we simply match the abundance of galaxies from our luminosity functions with the abudance of dark matter halos provided by the Tinker et al. (2008) halo mass function, and then assign the clustering bias of the halos to the galaxies assuming the bias function of Tinker et al. (2010). For the UDF, to our limiting magnitude we find that the typical cosmic variance (the fractional uncertainty in the total galaxy number counts owing to large scale structure) is $\sigma_{CV} \approx 0.30$ at $z \sim 7$ and $\sigma_{CV} \approx 0.36$ at $z \sim 8$. The typical bias for galaxies in the UDF is $b \approx 5.0$ at $z \sim 7$ and $b \approx 6.2$ at $z \sim 8$. For UDF-P1, we find that the typical cosmic variance is $\sigma_{CV} \approx 0.33$ at $z \sim 7$ and $\sigma_{CV} \approx 0.38$ at $z \sim 8$. The typical bias for galaxies in the UDF-P1 is $b \approx 5.4$ at $z \sim 7$ and $b \approx 6.6$ at $z \sim 8$. For UDF-P2, we find that the typical cosmic variance is $\sigma_{CV} \approx 0.32$ at $z \sim 7$ and $\sigma_{CV} \approx 0.37$ at $z \sim 8$. The typical bias for galaxies in the UDF-P2 is $b \approx 5.2$ at $z \sim 7$ and $b \approx 6.5$ at $z \sim 8$. For ERS, we find that the typical cosmic variance is $\sigma_{CV} \approx 0.30$ at $z \sim 7$ and $\sigma_{CV} \approx 0.34$ at $z \sim 8$. The typical bias for galaxies in the ERS field is $b \approx 6.4$ at $z \sim 7$ and $b \approx 7.7$ at $z \sim 8$. Lastly, for CANDELS-Deep we find that the typical cosmic variance is $\sigma_{CV} \approx 0.26$ at $z \sim 7$ and $\sigma_{CV} \approx 0.30$

at $z \sim 8$. The typical bias for galaxies in CANDELS-Deep is $b \approx 6.3$ at $z \sim 7$ and $b \approx 7.6$ at $z \sim 8$.

We also make an attempt to model the additional uncertainties introduced to our luminosity function calculations by cosmic variance. We repeat the calculations of Sections 3.4.2.1 and 3.4.2.2, but modify them to marginalize across fluctuations in the galaxy abundance in our survey volumes owing to density fluctuations. We calculate the expected number counts $n_{\mathrm{exp},k}$ as before (Equation 5), but for the likelihood of observing $n_{\mathrm{obs},k}$ galaxies given $n_{\mathrm{exp},k}$ we use

$$p(n_{\mathrm{obs},k}|n_{\mathrm{exp},k},\sigma_{CV}) = \int_{-1}^{\infty} d\delta_g \; p_{\mathrm{LN}}(\delta_g|\sigma_{CV}) \left(\frac{(1+\delta_g)n_{\mathrm{exp},k}}{\sum_j n_{\mathrm{exp},j)}}\right)^{n_{\mathrm{obs},k}}, \tag{3.8}$$

where σ_{CV} is the cosmic variance uncertainty in the number counts and the distribution of galaxy count overdensities δ_g is modeled as a lognormal

$$p_{\mathrm{LN}}(\delta_g|\sigma_{CV}) = \frac{1}{\sqrt{2\pi x^2}} \exp\left[-\frac{1}{2}\left(\frac{y}{x}+\frac{x}{2}\right)^2\right], \tag{3.9}$$

with $y \equiv \ln(1+\delta_g)$ and $x \equiv [\ln(1+\sigma_{CV}^2)]^{1/2}$. We have adopted this model from Robertson et al. (2010) (see also Adelberger et al. 1998), who used the lognormal distribution to model galaxy count fluctuations in the quasilinear regime. Note that in the limit $\sigma_{CV} \to 0$ we recover the previous method, and this approach treats the possible galaxy count fluctuations of each field independently. Given the cosmic variance uncertainty estimates calculated above, we conservatively adopt $\sigma_{CV}(z \sim 7) = 0.4$ and $\sigma_{CV}(z \sim 8) = 0.45$. Since Equation 3.8 models the shape of the luminosity function we adopt the same normalization constraint as before, treating contributions to the total galaxy count from all fields simultaneously.

The results for such an extension of the fitting are shown in Figures 3.4 and 3.5 as dark gray bands (68% confidence intervals including cosmic variance uncertainty). Including cosmic variance uncertainty and using the likelihood in Equation 3.8, we find best fit Schechter function parameters of $\log_{10}\phi_\star = -3.18^{+0.32}_{-0.38}$, $M_{\mathrm{UV},\star} = -20.14^{+0.41}_{-0.46}$, and $\alpha_{z\sim7} = -1.87^{+0.25}_{-0.22}$ at redshift $z \sim 7$ and $\log_{10}\phi_\star = -3.52^{+0.42}_{-0.58}$, $M_{\mathrm{UV},\star} = -20.47^{+0.52}_{-0.75}$, and $\alpha_{z\sim8} = -1.94^{+0.34}_{-0.30}$ at redshift $z \sim 8$. The fitting method recovers almost exactly the best fit parameters found without accounting for cosmic variance uncertainty, but the marginalized uncertainties on the parameters increase. The uncertainties on the faint-end slope α increase by $\Delta\sigma_\alpha \approx 0.05 - 0.08$ at redshift $z \sim 7$ and by $\Delta\sigma_\alpha \approx 0.09 - 0.10$. Since we have assumed a conservatively large cosmic variance uncertainty, we expect these additional uncertainties to be somewhat overestimated. Nonetheless these observations have provided high precision measures of the luminosity function parameters at $z \sim 7$ and $z \sim 8$, even accounting for cosmic variance uncertainties.

3.5 Discussion

3.5.1 Comparison with McLure et al. (2013)

We now compare our results with those of McLure et al. (2013). Of our combined sample of 74 UDF12 sources, 57 are identified as robust and 13 as non-robust, leaving only 4 not selected in either category by McLure et al. (2013). Examining these objects individually, one was excluded, as it was too close to the edge of the detector, although this difference is accounted for in the selection volume simulations for each paper. The remaining 3 objects were excluded by virtue of a concern by McLure et al. (2013) that they might lie at $z < 6.5$. The SED approach imposes a strict lower redshift limit, whereas our drop-out selection functions maintain some sensitivity to $z \sim 6.0 - 6.3$ (Figure 3.2). These differences in selection sensitivity are fully accounted for in the two analyses.

Notwithstanding the agreement, McLure et al. (2013) have amassed a sample of 100 robust high-redshift candidates in comparison to our 74. We list here the reasons a number of these objects were excluded from our sample. Two objects lie at $z \geq 9.5$, which our selection criteria are insensitive to. Our more stringent optical rejection criteria preclude another 7 candidates from our final sample. Additionally, we exercised caution in excluding an additional two candidates which lie in close proximity to extended, low-redshift galaxies. When the above differences are accounted for, we find that McLure et al. (2013) includes an additional 28 $z > 6.5$ candidates that are not accepted by our selection functions, which only target objects with evidence of a firm spectral break in adjacent filters.

Table 3.6. Best fit LF parameter compilation

Study	$z \simeq 7$			$z \simeq 8$		
	$\log_{10}\phi_\star$ [Mpc^{-3}]	$M_{\rm UV,\star}$	α	$\log_{10}\phi_\star$ [Mpc^{-3}]	$M_{\rm UV,\star}$	α
This work	$-3.19^{+0.27}_{-0.24}$	$-20.14^{+0.36}_{-0.48}$	$-1.87^{+0.18}_{-0.17}$	$-3.50^{+0.35}_{-0.32}$	$-20.44^{+0.47}_{-0.35}$	$-1.94^{+0.21}_{-0.24}$
McLure et al. (2013)	$-2.96^{+0.18}_{-0.23}$	$-19.90^{+0.23}_{-0.28}$	$-1.90^{+0.14}_{-0.15}$	$-3.35^{+0.28}_{-0.47}$	$-20.12^{+0.37}_{-0.48}$	$-2.02^{+0.22}_{-0.23}$
Lorenzoni et al. (2013)	-3.14	-20.19	-1.9 (fixed)	-3.02	-19.37	-1.9 (fixed)
Bradley et al. (2012a)	-	-	-	$-3.37^{+0.26}_{-0.29}$	$-20.26^{+0.29}_{-0.34}$	$-1.98^{+0.23}_{-0.22}$
Oesch et al. (2012)	-	-	-	$-3.30^{+0.38}_{-0.46}$	$-20.04^{+0.44}_{-0.48}$	$-2.06^{+0.35}_{-0.28}$
Grazian et al. (2012)	-3.13 (fixed)	-20.14 (fixed)	-1.7 ± 0.1	-	-	-
Bouwens et al. (2011)	-3.07 ± 0.26	-20.14 ± 0.26	-2.01 ± 0.21	-3.23 ± 0.43	-20.10 ± 0.52	-1.91 ± 0.32

As expected therefore, the results of the luminosity function studies are in excellent agreement. The best fit parameters for both studies are summarized in Table 3.6. All derived parameters are consistent within 1σ with error bars of comparable size. In particular, the faint end slopes, α, agree to well within the 1σ errors. As one of the main goals of UDF12 was to improve this measurement, the robustness of our conclusions with respect to differing selection methodology is reassuring.

3.5.2 Comparison with other high-redshift literature

It is instructive to compare the Schechter function parameters derived by our study to those of previous analyses, both at these redshifts, and below. While the full array of derived parameters from recent high-redshift studies is available in Table 3.6, we focus here again on the faint end slope, α. Previous studies at redshifts $2 < z < 6$ find a remarkably consistent value of $\alpha \sim -1.7$ across this range (e.g., Oesch et al. 2007; Bouwens et al. 2007; Reddy & Steidel 2009; McLure et al. 2009).

At the moderately larger redshift of $z \sim 7$, the situation remains much more uncertain. While Bouwens et al. (2011) claim a significantly steepened value of $\alpha = -2.01 \pm 0.21$, at $z \sim 7$, Grazian et al. (2012) find no signal of slope evolution, determining $\alpha = -1.7 \pm 0.1$. Our determination of $\alpha_{z\sim7} = -1.87^{+0.18}_{-0.17}$, though still consistent with -1.7, does suggest a steepening of the faint end slope with increasing redshift, especially when considering the value of $\alpha = -1.90^{+0.14}_{-0.15}$ determined by McLure et al. (2013).

At $z \sim 8$, the existing literature largely agrees on a steepening of α, with the most recent determinations by Bouwens et al. (2011), Oesch et al. (2012), and Bradley et al. (2012a) finding values between -1.9 and -2.1. Extending 0.25 magnitudes fainter in UV luminosity than any previous study, our determination of $\alpha_{z\sim8} = -1.94^{+0.21}_{-0.24}$ provides increased support for this evolution, in concert with the $\alpha_{z\sim8} = -2.02^{+0.22}_{-0.23}$ found by McLure et al. (2013). As noted by many authors (e.g., Robertson 2010b; Bouwens et al. 2012a), this will significantly increase the ability of galaxies to maintain the reionization of the intergalactic medium as intrinsically faint sources become more numerous. This steepening is also predicted by conditional luminosity function methods based on the evolution of the dark matter halo mass function (Trenti et al. 2010; Tacchella et al. 2013). We also note that although our derived values of $\phi_\star$ and $M_{\rm UV,\star}$ favor an decreasing $\phi_\star$ with redshift to account for the evolution of the luminosity function, the errors are still too large to rule out an evolution in the characteristic magnitude instead (or a combination). The reader may also wish to read a significantly more detailed analysis of the impact of our survey on reionization in Robertson et al. (2013).

3.5.3 Summary

Along with McLure et al. (2013), we have uncovered the most comprehensive and robust sample of subluminous high-redshift galaxies to date. At moderate magnitudes, $M_{\rm UV} \leq -18.0$, we achieve a more refined sample of dropouts, including an additional 3 (3) z-drops (Y-drops) not previously identified as high redshift sources as a result of our improved photometry. Of greater importance, though, are our advances below this UV magnitude; we discover an additional 14 sources at $z \sim 7$ by virtue of our ultradeep Y_{105} image, as well as an additional 5 sources at $z \sim 8$, indicating the steepness of the faint end slope continues beyond 2 magnitudes below $M_{\rm UV,\star}$ at these redshifts. Additionally, our sample is in excellent agreement with the independent determination from McLure et al. (2013). We note only 2 of our sources at $z \sim 7$, as well as 2 at $z \sim 8$ that are not present in their final catalog.

With the upcoming HST *Frontier Fields* observations scheduled to begin in Cycle 21, progress in this regime vital to understanding if and when starforming galaxies can maintain reionization is sure to continue. We stress that the gains made by UDF12 strengthen claims of an increased steepness at the faint end and, along with McLure et al. (2013), provide a self-consistent, robust determination of α at redshifts 7 and 8.

Chapter 4

Contamination of Broad-Band Photometry by Nebular Emission in High Redshift Galaxies: Investigations with Spitzer and MOSFIRE

Abstract

Earlier work has raised the potential importance of nebular emission in the derivation of the physical characteristics of high redshift Lyman break galaxies. Within certain redshift ranges, and especially at $z \simeq 6-7$, such lines may be strong enough to reduce estimates of the stellar masses and ages of galaxies compared those derived, assuming broad-band photometry represents stellar light alone. To investigate this, we first review the results of Stark et al. (2013). In this work, we isolated galaxies in the previously detailed Keck spectroscopic survey which lie in the redshift range $3.8 < z < 5.0$. For these galaxies, Hα falls within the IRAC 3.6 μm filter, while the adjacent K_s and 4.5 μm filters are free from any strong nebular lines. We fit spectral energy distributions (SEDs) to the data excluding the contaminated 3.6 μm filter, and use the difference between the SED-predicted and observed flux to infer, photometrically, the strength of the Hα emission line.

To test this hypothesis at the highest redshifts where such lines can be probed spectroscopically with ground-based facilities, we examine the near-infrared spectra of a representative sample of 28 $3.0 < z < 3.8$ Lyman break galaxies using the newly-commissioned MOSFIRE near-infrared spectrograph at the Keck I telescope. We use this data to derive the rest-frame equivalent widths (EW) of [OIII] emission. Although our current sample is modest, its [OIII] EW distribution is consistent with that inferred for Hα based on SED fitting of Stark et al's larger sample of $3.8 < z < 5$ galaxies. For a subset of survey galaxies, we use the combination of optical and near-infrared spectroscopy to quantify kinematics of outflows in $z \simeq 3.5$ star-forming galaxies, and discuss the implications for reionization measurements. The trends we uncover underline the dangers of relying purely on broad-band photometry to estimate the physical properties of high redshift galaxies and emphasize the important role of diagnostic spectroscopy. Having demonstrated the validity of deriving emission line strengths through broadband photometry, we conclude with a revised estimate of the stellar mass density of the universe at $4 < z < 8$, corrected for these effects.

4.1 Introduction

Detailed photometry of Lyman Break galaxies undertaken with the *Hubble Space Telescope* and the *Spitzer Space Telescope* has provided spectral energy distributions for large samples of Lyman break galaxies in the important redshift range $3 < z < 7$. These data have been used to derive valuable estimates of the star formation rates, stellar masses, and ages (e.g., Stark et al. 2009; Labbé et al. 2010; González et al. 2011). Accurate measurements of galaxies' stellar masses, which we are concerned with in this work, are particularly important because they enter into the calculation of two quantities fundamental to our understanding of reionization and early galaxy formation: the specific star formation rate (sSFR) of galaxies, and the cosmic stellar mass density (SMD).

Observations of the specific star formation rate can provide a valuable test of galaxy formation scenarios when compared with theoretical work. If gas for star formation is provided by inflows of cold baryonic material, both semi-analytic models and numerical simulations predict that the sSFR should closely follow the specific baryon accretion rate (e.g., Weinmann et al. 2011; Davé et al. 2011). This rate is thought to rise steeply with redshift as $(1+z)^{2.25}$ (Neistein & Dekel 2008). Thus if the physics of star formation did not appreciably change over the period $2 < z < 7$, we would expect a corresponding rapid increase in the sSFR as well. However, earlier results (Stark et al. 2009; González et al. 2010; Bouwens et al. 2012a) showed only a relatively modest increase of less than a factor of two across this epoch, leading to numerous theoretical efforts to explain this discrepancy. Possible explanations include metallicity-dependent star-formation suppression (Krumholz & Dekel 2012) or delayed gas consumption (Weinmann et al. 2011), though these are both a posteriori corrections.

The cosmic stellar mass density is another particularly important measurement, as it provides a key indication of whether yet earlier star formation at $z > 6$ is capable of maintaining cosmic reionization. Here, tension has been observed within the observations themselves, with derived stellar mass densities overestimating the prediction found by integrating the measured UV-derived star formation rate densities across time (Robertson 2010b).

Of course, these tensions have not gone unnoticed. Many earlier studies (e.g., Schaerer & de Barros 2009, 2010; Ono et al. 2010; de Barros et al. 2014) have suggested that high redshift stellar masses and stellar mass densities may be overestimated because the broad-band fluxes analyzed may be contaminated by strong nebular emission lines (e.g., [OII], [OIII], Hα). Although this contamination has been well-documented in some rare local star-forming galaxies (e.g., Sargent & Searle 1970; Krueger et al. 1995; Papaderos et al. 1998), and more recently at moderate redshifts through HST grism data (Atek et al. 2011), the extent of such contamination is largely unconstrained at the high redshifts relevant for understanding cosmic reionization.

Early attempts address this problem at high redshift, mentioned above, used 'forward modeling' techniques which fit stellar population synthesis models, including nebular emission, to broad-band

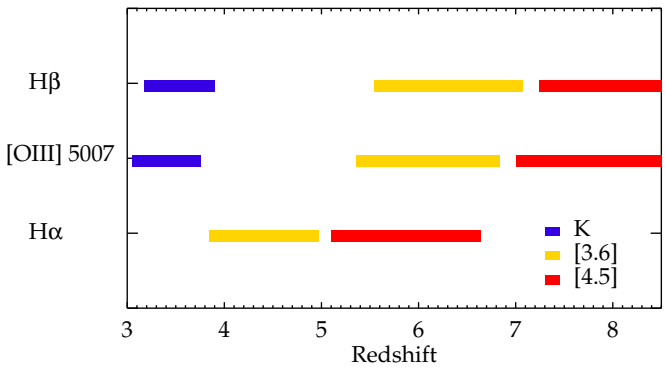

Figure 4.1 Colored stripes denote redshift ranges over which emission lines contaminate the K_s band (dark blue), IRAC 3.6 μm (yellow), and IRAC 4.5 μm (red) filters. Hα emission is expected in the 3.6 μm filter at $3.8 < z < 5.0$, with no lines expected in either adjacent filter.

photometry without any knowledge of the galaxy redshifts. These methods suffer from a major limitation: it is not known a priori which filters are likely contaminated. In this respect, examining the SEDs of galaxies of known spectroscopic redshift provides a much sounder approach (Shim et al. 2011). In this chapter, we perform such a study by examining galaxies with known spectroscopic redshifts in the range $3.8 < z < 5.0$, drawn from our extensive Keck survey. Within this window, the 3.6 μm IRAC filter encompasses the Hα emission, while the adjacent K_s and 4.5 μm filters are devoid of any strong lines. By fitting SEDs to these objects and calculating the excess in the observed flux relative to that predicted from a stellar continuum only SED, we infer the characteristic strength of nebular emission lines in these galaxies, as well as derive new estimates of the specific star formation rate and cosmic stellar mass density. This is particularly important at $z \simeq 6 - 7$, where both the 3.6 and 4.5 μm IRAC filters are contaminated by nebular emission ([OIII] and Hα, respectively). We provide a graphic to illustrate line contamination in various filters as a function of redshift in Figure 4.1.

To place these findings on an even firmer basis, we then take the next logical step by verifying *directly with near-infrared spectroscopy* the impact of nebular emission in the analysis of SEDs for high redshift LBGs. Prior to the launch of the *James Webb Space Telescope (JWST)* it will not be possible to directly examine contamination by $H\alpha$ emission within the IRAC warm filters. However, in a manner similar to that described above, we can investigate contamination by Hβ and [OIII] 4959+5007 Å in the photometric K_S band at 2.2μm by studying a representative sample of $3.0 < z < 3.8$ spectroscopically-confirmed LBGs. Our goal is to determine the rest-frame equivalent width distribution of [OIII] directly, and to compare this to the extent possible with that inferred for Hα from the our Spitzer/IRAC SED-based study. Such a spectroscopic program is made possible by the arrival at the Keck 1 telescope of the multi-slit near-infrared spectrograph MOSFIRE (McLean

et al. 2012) which offers the advantage of a significant multiplex gain. Using this new instrument, we target a representative sample of LBGs selected to lie within the $3.0 < z < 3.8$ redshift range in the GOODS North field. We can thus take advantage of ACS photometry from the GOODS survey and improved near-infrared photometry from the CANDELS survey. This extensive photometry further means we can directly compare measured [OIII] fluxes with those inferred using the SED-based approach.

Throughout this work, we adopt a $\Lambda-$dominated, flat universe with $\Omega_\Lambda = 0.7$, $\Omega_M = 0.3$, and $\mathrm{H}_0 = 70\,\mathrm{h}_{70}\ \mathrm{km\,s^{-1}\,Mpc^{-1}}$. All magnitudes in this paper are quoted in the AB system (Oke & Gunn 1983). We will refer to the HST ACS and WFC3/IR filters F435W, F606W, F775W, F850LP, F105W, F125W, and F160W as B_{435}, V_{606}, i_{775}, z_{850}, Y_{105}, J_{125}, H_{160}, respectively. Additionally, we will refer to the Spitzer/IRAC 3.6 and 4.5 μm filters as [3.6] and [4.5], respectively.

4.2 Hα emission line strengths from Spitzer IRAC photometry

In this section, we briefly review the methodology and analysis used in Stark et al. (2013a) to derive emission line strengths from broadband photometry at $3.8 < z < 5.0$, before moving on to our attempts to validate this method with direct spectroscopy at $3.0 < z < 3.8$.

4.2.1 Data

In order to proceed with this project, we required a large sample of galaxies with spectroscopic redshifts. This is provided by the Keck spectroscopic survey, previously described in Chapter 2, as well as Stark et al. (2010) and Stark et al. (2014, in prep.). As mentioned previously, for this experiment we are only concerned with the subset of galaxies spectroscopically confirmed to be at $3.8 < z < 5.0$, limiting our sample to 92 objects. We further cull this sample by requiring that each object be significantly detected ($> 5\sigma$) in the IRAC [4.5] band, resulting in a subset of 45 remaining galaxies. Such a cut ensures that we will be able to get a meaningful fit to the stellar continuum longward of the contaminated [3.6] filter, crucial to a robust measurement of the emission line equivalent width.

Optical photometry for these galaxies is drawn from the publicly released GOODS v2 cagalogs (Giavalisco et al. 2004). In GOODS-S, we add to this the public release of the WFC3 imaging from the CANDELS Multi-Cycle Treasury Program (Grogin et al. 2011; Koekemoer et al. 2011), as well as our own reduction (see McLure et al. 2011) of the Early Release Science imaging (Windhorst et al. 2011). We computed colors relative to z_{850} using matched apertures, and total WFC3 magnitudes were assigned by combining these colors with the total z_{850} flux given by MAG_AUTO in the

GOODS catalog. We obtain K_s photometry using deep ISAAC imaging (Retzlaff et al. 2010), conducting photometry in 1" diameter circular apertures and correcting to total magnitudes using offsets determined from bright but unsaturated stars in the image. In GOODS-N, we utilize near-infrared imaging from CFHT/WIRCAM (Wang et al. 2010), obtaining photometry through the same method as in the ISAAC imaging.

The crucial rest-frame optical imaging is provided by the deep Spitzer/IRAC (Fazio et al. 2004) imaging of both GOODS fields. We utilize both the [3.6] and [4.5] imaging, which have approximate exposure times of 23 hours per pointing for each filter. Due to the $\sim$ 1.7" point spread function, many objects become confused with their neighbors, so we exercise caution with our photometry. For isolated objects, we perform photometry in a 2.4" diameter circular aperture, applying a 0.7 mag correction for light outside the aperture derived from isolated point sources. In GOODS-S, we augment this with flux measurements for confused objects from the MUSIC catalog (Santini et al. 2009).

4.2.2 SED fitting

Our method for deriving emission line strengths relies on not just accurate photometry, but accurate SED fits. By virtue of our spectroscopic redshifts, we already eliminate a key source of uncertainty. Our fitting procedure is based on the population synthesis models of Bruzual & Charlot (2003). For consistency with earlier work, we adopt a Salpeter (1955) initial mass function with a range from $0.1 - 100 M_{\odot}$. We construct a grid of models, varying the age between 5 Myr and the age of the universe, dust reddening according to the prescription from Calzetti et al. (2000) in steps of 0.02 from $E(B-V) = 0.0$ to 0.5, and the normalization factor. We fix the star formation history as either constant or rising with time according to the $t^{1.7}$ power law fit in Papovich et al. (2011). Motivated by measurements of $z \sim 4$ LBGs in Jones et al. (2012), we adopt a metallicity of $Z = 0.2 Z_{\odot}$.

To calibrate our fitting procedure, we use a sample of four spectroscopically confirmed $1.8 < z < 2.3$ galaxies from the HST grism survey of Trump et al. (2011). For these objects, we have both a robust measurement of the total line flux from the grism data, as well as WFC photometry for which the emission line falls within either the J_{125} or H_{160} filter. We fit the data using the procedure described above, both including and excluding the contaminated filter from the fit, then subtracting the synthetic SED photometry from that actually observed to measure the emission line strength. We find that in all four cases, the fit *including* the contaminated filter provides a closer match to the line flux as measured by the grism, while the fit excluding the contaminated filter consistently provides an overestimate. As such, we have chosen to include the filter contaminated by emission line flux even when fitting our stellar continuum only SEDs, but also discuss the change in results when this filter is excluded.

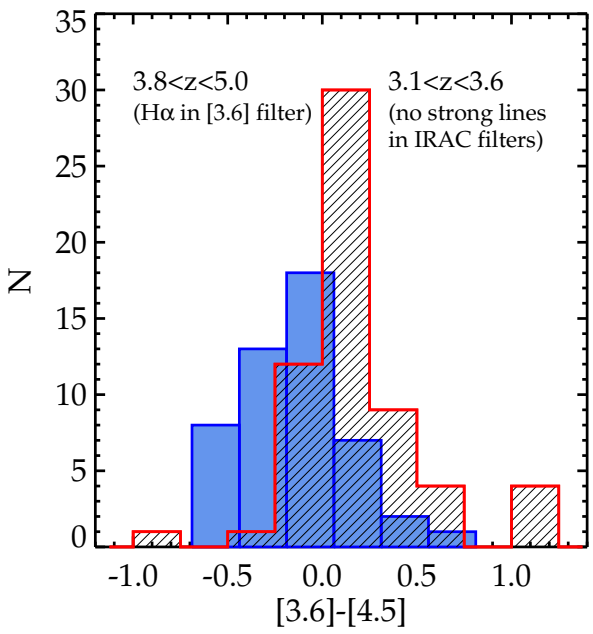

Figure 4.2 Evidence for emission line contamination in Spitzer/IRAC broadband colors. We compare the distribution of [3.6]-[4.5] colors for spectroscopically confirmed galaxies at $3.1 < z < 3.6$, where no strong rest-optical lines are in either IRAC filter (red shaded histogram) with the same color for galaxies at $3.8 < z < 5.0$, where Hα falls in the [3.6] filter (blue filled histogram). A clear offset toward bluer colors is seen for the latter, with a median color 0.33 mag bluer.

4.2.3 Evidence for [3.6] emission line contamination

4.2.3.1 Comparison to control sample

We begin our analysis with a brief comparison of the [3.6] - [4.5] IRAC colors of our galaxies to a control sample to simply demonstrate the evidence for nebular emission. For our control sample, we use a subset of galaxies, also spectroscopically confirmed from our Keck survey, but which lie at slightly lower redshifts, $3.1 < z < 3.6$. Given the typical spectra of high-redshift star-forming regions, this control sample should have no strong emission lines contaminating either the [3.6] or [4.5] filter, and thus a significantly redder IRAC color than our selected sample. Indeed, this is observed for both samples in Figure 4.2; the median [3.6] - [4.5] color at $3.8 < z < 5.0$ is 0.33 mag bluer than the $3.1 < z < 3.6$ median. A Kolmogorov-Smirnov test conclusively demonstrates that the two colors are drawn from different distributions, with an associated probability by chance of 8×10^{-8}. Now that we have preliminary evidence of broadband photometric contamination by emission lines, we continue to a more precise determination of the equivalent width distribution.

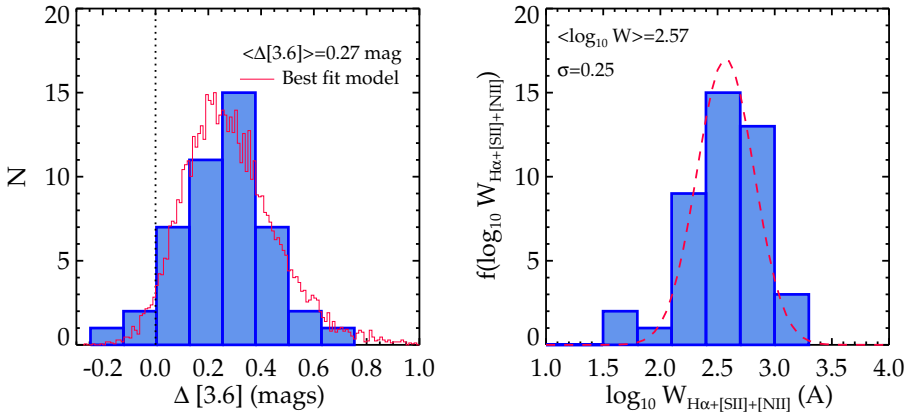

Figure 4.3 Left: Histogram of observed [3.6] flux excesses above best fitting stellar continuum models. Positive values indicate an observed flux above that of the best fit model, and thus evidence for emission line contamination. The red histogram denotes the shape of our best fit lognormal function for the distribution of EWs, with $\sigma = 0.25$ and $\langle \log_{10}(W_{[3.6]}/\text{Å}) \rangle = 2.57$, and an additional photometric scatter of 20%. Bottom: Implied EW distribution from Δ[3.6]measurements. Red dashed line represents the best fitting lognormal distribution again, but with no added scatter.

4.2.3.2 Hα strength

To estimate the strength of nebular emission contaminating the measured [3.6] μm fluxes of our $3.8 < z < 5.0$ sample, we compute the difference between the observed [3.6] magnitude and that predicted by our best-fitting stellar continuum SED. From this point forward, we will refer to this quantity as Δ[3.6], where positive values indicate that the observed flux exceeds that predicted by our SED. We plot the distribution of this measurement in Figure 4.3, which reveals that 96% of our galaxies display a positive value for Δ[3.6], pointing to near-ubiquitous large equivalent widths. In fact, the median excess of 0.27 mag suggest that the typical rest-frame total emission line EW contribution is 360-450 Å. Although our test with the Trump et al. (2011) grism sample showed superior line flux agreement when the contaminated filter was included in the SED fitting, we also investigate the EW inferred if the [3.6] filter is excluded from the fit. In this case, the stellar continuum level is typically reduced, and the median Δ[3.6] increases to 0.37 mag, implying total EWs of 520-650 Å.

We now seek to estimate the entire distribution of equivalent widths, rather than focusing on median values. To do so, we assume that EWs are distributed lognormally, similar to that seen from Hα emission locally and at moderate redshifts (e.g., Lee et al. 2007, 2012; Ly et al. 2011). We consider a grid spanning a range of σ and μ, the mean and width of the EW distribution in log space. Each EW is translated into a [3.6] photometric excess, applying a photometric scatter of 20%. We then compute the Δ[3.6] distribution expected from our input EW distribution, and find the parameters that produce a distribution most similar to that which we measure. From this

exercise, we find the best fitting parameters to be $\sigma = 0.25$ and $\langle \log_{10}(W_{[3.6]}/\text{Å}) \rangle = 2.57$.

Although this contribution will surely be dominated by Hα emission, there will likely be a number of lower strength emission lines that contribute as well, including [SII] and [NII]. To estimate their contribution to the [3.6] excess across our redshift range, we use the synthetic nebular emission spectrum code from Robertson (2010b). This code, given a metallicity and output of ionizing photons from a stellar population, will produce a full nebular spectrum including H, He, and metal emission lines and nebular continuum. Hydrogen emission line ratios are calculated assuming case B recombination, while metal emission line ratios are calibrated with the empirical relations given in Anders & Fritze-v. Alvensleben (2003) as a function of metallicity. We find that, given our redshift range and assumption of $Z = 0.2Z_{\odot}$, Hα contributes an average of $\simeq 76\%$ of the total emission line excess. Thus, the typical Hα EW in this redshift range is $\langle \log_{10}(W_{H\alpha}/\text{Å}) \rangle = 2.45$.

We now compare our results with those of Shim et al. (2011). At face value, both samples are similar in that they investigate spectroscopically confirmed galaxies at $3.8 < z < 5.0$, yet they measure a median EW of 580 Å while ours is only 270 Å. The first reason for our discrepancy lies in the choice of filters used to determine the stellar continuum SED level. Shim et al. (2011) exclude the [3.6] filter from their continuum fit, while we include it, motivated by the improved agreement shown by emission lines at $z \sim 1-2$ measured with the HST grism. If we instead exclude the [3.6] filter from our fits, the stellar continuum is lowered and we find an EW of 410 Å, closer to the value measured by Shim et al. (2011). Another difference between the two studies is the dust law used. While we only use the dust prescription from Calzetti et al. (2000), Shim et al. (2011) use both the Calzetti extinction law and a steeper law appropriate for the SMC, taking the EW from the best fit between the two models. If we limit their sample to only results using the Calzetti law, the median EW drops to only 490 Å. Thus, the apparently large discrepancy between our work and theirs is largely due to different procedures in the fitting. However, given that we have calibrated our results to a HST grism sample at $z \sim 1-2$, we remain confident in our results.

In the following sections, we discuss our attempts to investigate rest-optical line strengths spectroscopically at the highest redshifts possible from the ground, while in Section 4.4.4, we discuss the consequences for the stellar mass density given the verification of these line strengths.

4.3 [OIII]4959/5007 and Hβ emission line strengths from MOSFIRE

4.3.1 Target selection

4.3.1.1 Photometry

For our target selection and SED fitting, it was necessary to assemble a full multi-wavelength catalog across the GOODS-N field. For the HST ACS data, we use the publicly available v2.0 GOODS-N mosaics (Giavalisco et al. 2004). For the newly-obtained CANDELS WFC3/IR data (Grogin et al. 2011; Koekemoer et al. 2011), we combine the single epoch mosaics publicly available as of March 2013 weighting by exposure time, using the image combination routine SWARP (Bertin et al. 2002). Our CANDELS reductions comprise the first 7 epochs taken in GOODS-N, and so a number of objects do not yet have coverage in the Y_{105} filter. However, as we have J_{125} and H_{160}, imaging for all targets, this does not constitute a significant weakness for our SED analyses.

To compute accurate colors for each object, we measured the flux of each object in PSF-matched images. Our PSF matching was done using the *ColorPro* program (Coe et al. 2006). Briefly, we first assembled a PSF for each filter by shifting and stacking ~ 20 bright unsaturated stars. We detected all objects using the i_{775} image, and determined colors using matched isophotal apertures after degrading the i_{775} image FWHM to equal that of each other image in turn. Colors were then corrected to total values by computing the offset from MAG AUTO for the i_{775} band in the GOODS v2.0 catalog. In cases where MAG AUTO was deemed to be unreliable by visual inspection of the images, we used the offset to a flux measured in a 1.0" diameter aperture to derive a total magnitude.

For the key photometry in the spectral region of interest, we use the K_S-band image derived from ultra-deep Canada France Hawaii Telescope imaging published by Wang et al. (2010). This image has total exposure time $t = 49.4$ hr and a 5σ limiting magnitude of 24.5 in the GOODS-N field. As the FWHM of the image is 0.7-0.8", we do not attempt to PSF-match the other images to this coarser resolution. Rather, as our objects are largely compact, we perform photometry in 1.0" diameter apertures, and apply a correction of 0.7 mag for flux falling outside the aperture, determined from analyses of isolated, unsaturated stellar sources in the K_S image. Finally, where available, we use deconfused Spitzer 3.6 and 4.5 μm photometry from the GOODS Superdeep IRAC data. A full description of the deconfusion procedure can be found in McLure et al. (2011).

4.3.1.2 Spectroscopic Sample

Our primary source of targets consisted of spectroscopically-confirmed galaxies from the Keck survey of $3 < z < 6$ LBGs (Stark et al. 2010, 2011) in the GOODS-N field. Briefly, this sample was compiled via optical follow-up of color-selected Lyman break galaxies (B, v, and i-drops) with the

DEIMOS spectrograph on Keck II. The relevant observations took place between 2008 and 2010, and integration times for the sample considered here ranged from 5.0 to 7.0 hours. The interested reader can find the full details of the sample in Stark et al. (2010) and Stark et al. (2014, in prep.).

From this compilation, we chose to undertake near-infrared spectroscopy of LBGs, primarily B-drops, with confirmed redshifts $3.0 < z < 3.8$ since both Hβ and [OIII] 4959 + 5007 lie within the MOSFIRE K-band transmission window. As the original B-drop sample only sparsely populates the above redshift range, in anticipation of the present needs, we increased the available sample via further DEIMOS observations in June 2012 using photometric redshifts to improve the redshift coverage. To achieve this, we first created a catalog of B_{435} dropout galaxies using the GOODS v2.0 catalogs and the selection criteria outlined in Stark et al. (2009). These SEDs were then evaluated with a photometric redshift code to assess their chances of lying at $z \leq 3.8$. This is a key step, as the B-drop sample possesses a mean redshift of $z \sim 4.0$, and only $\simeq 25\%$ of B-drops lie below $z = 3.8$ (see Figure 4.4). Our priorities for inclusion of these targets on the mask were the probability of lying at $z < 3.8$ and the z_{850} magnitude for each target, with brighter targets favored. The observations and data reduction for these additional targets were undertaken in the same manner as those previously described in Stark et al. (2010).

This investment of spectroscopic observing time enabled us to select targets that are known *a priori* to lie in the accessible redshift range, and maximizes our efficiency. Additionally, in the event of non-detections of nebular emission lines, prior knowledge of the redshift affords robust upper limits on the fluxes. In total, we were able to include 13 out of a total of 23 objects with prior spectroscopic identification at $3.0 < z < 3.8$ in our MOSFIRE campaign. As in our additional DEIMOS mask, these objects were prioritized by their z_{850} magnitude (brighter galaxies being favored) and our ability to create efficient mask placements. In all tables and plots, these objects with pre-determined DEIMOS redshifts are identified with the tag '-D' following their IDs.

Since we are interested in the nebular emission line properties of this sample, it is important to note that all the targets for the various DEIMOS campaigns were selected only using ACS photometry, and thus should not be significantly biased towards objects with strong nebular emission.

4.3.1.3 Photometric Sample

As MOSFIRE can accommodate as many as 46 slits on a single mask, we sought to augment our spectroscopic sample above with further photometrically-selected LBGs. Our procedure for adding new targets was largely as described above, except the SEDs now incorporated CANDELS WFC3 data where appropriate, and deconfused Spitzer IRAC photometry.

Although one of the goals of this campaign was to verify the technique pioneered in Shim et al. (2011) and Stark et al. (2013a) of using photometric excesses to determine line strengths, we specifically avoided prioritizing targets by their K-band magnitude. This allows us to construct an unbiased

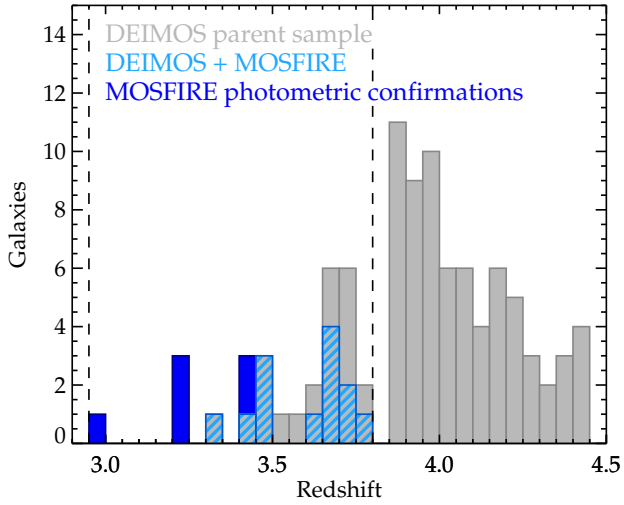

Figure 4.4 Redshift distribution of Lyman Break Galaxies targeted with MOSFIRE. The grey histogram indicates the parent sample within GOODS-N from our prior DEIMOS campaign. The light blue cross-hatched histogram denotes the subset of the DEIMOS spectroscopic sample studied with MOSFIRE and the dark blue histogram that drawn from a photometric selection (see Section 4.3.1.3). Dashed lines show the boundaries within which [OIII] is expected to contaminate the K_S photometry.

sample, and thus a better estimate of the true distribution of nebular line equivalent widths in the following analysis.

In total, we included 15 galaxies from this photometric sample spread across these two masks, but failed to observe any significant line emission in 8 of these. Given the uncertainty in the photometric redshift estimates, we consider two extreme case to explain this lack of emission. In our later analysis (Section 4.4.2), namely that all lie outside the required redshift range $3.0 < z < 3.8$, or that all lie within it but with line emission fainter than our detection limit.

Table 4.1. MOSFIRE target list and properties

ID	Mask	RA	Dec	m_{z850}	z	Mass / $[10^9 M_\odot]$	SFR $[M_\odot\ \mathrm{yr}^{-1}]$	E(B-V)	$\log_{10}$(age / yr)	m_{Ks} [b]
N33_24311-D	1	12:37:06.55	62:15:35.4	25.3	3.474	$1.1^{+0.2}_{-0.3}$	$15.8^{+1.0}_{-0.6}$	$0.05^{+0.00}_{-0.00}$	$7.91^{+0.10}_{-0.15}$	24.1 ± 0.2
N33_19880-D	1	12:36:55.14	62:15:29.2	26.7	3.405	$1.4^{+2.8}_{-1.2}$	$3.4^{+15.6}_{-1.3}$	$0.05^{+0.10}_{-0.05}$	$8.71^{+0.55}_{-1.71}$	25.1 ± 0.4
N33_25713-D	1	12:37:10.62	62:14:52.6	25.6	3.615	$5.7^{+3.2}_{-3.2}$	$37.2^{+40.0}_{-15.5}$	$0.20^{+0.05}_{-0.05}$	$8.26^{+0.45}_{-0.70}$	24.5 ± 0.2
N33_18549-D	1	12:36:51.89	62:15:14.5	26.0	3.333	$6.5^{+3.0}_{-0.5}$	$21.8^{+0.5}_{-8.6}$	$0.20^{+0.00}_{-0.05}$	$8.56^{+0.40}_{-0.05}$	24.3 ± 0.2
N33_19374-D	1	12:36:53.88	62:14:18.0	26.3	3.653	$78.6^{+11.2}_{-19.5}$	$70.7^{+3.2}_{-1.2}$	$0.35^{+0.00}_{-0.00}$	$9.16^{+0.07}_{-0.15}$	23.9 ± 0.1
N33_24278-D	1	12:37:06.46	62:13:20.5	25.8	3.671	$6.7^{+2.5}_{-4.8}$	$7.5^{+6.1}_{-0.1}$	$0.05^{+0.05}_{-0.00}$	$9.06^{+0.15}_{-0.85}$	25.2 ± 0.5
N33_25726-D	1	12:37:10.66	62:12:39.0	25.2	3.733	$10.4^{+2.3}_{-1.9}$	$39.2^{+0.9}_{-0.8}$	$0.15^{+0.00}_{-0.00}$	$8.51^{+0.10}_{-0.10}$	24.0 ± 0.1
N32_20647-D	1	12:36:57.00	62:11:51.0	26.3	3.740	$0.9^{+3.5}_{-0.7}$	$9.6^{+19.4}_{-6.4}$	$0.10^{+0.05}_{-0.10}$	$8.06^{+1.15}_{-1.06}$	25.6 ± 0.9
N32_23933-D	1	12:37:05.52	62:11:27.2	25.3	3.469	$11.8^{+1.0}_{-1.0}$	$106.8^{+2.7}_{-2.8}$	$0.30^{+0.00}_{-0.00}$	$8.11^{+0.05}_{-0.05}$	23.4 ± 0.1
N32_15359	1	12:36:43.54	62:11:21.4	24.4	3.488	$11.7^{+1.8}_{-0.7}$	$1047.6^{+74.4}_{-122.6}$ [a]	$0.40^{+0.00}_{-0.00}$	$7.06^{+0.12}_{-0.06}$	23.0 ± 0.1
N42_7697-D	2	12:36:22.17	62:09:42.3	25.8	3.771	$2.1^{+1.4}_{-1.6}$	$9.9^{+42.1}_{-0.4}$	$0.05^{+0.10}_{-0.00}$	$8.41^{+0.25}_{-1.41}$	25.5 ± 0.7
N42_12130-D	2	12:36:35.15	62:08:50.8	26.0	3.474	$1.7^{+1.6}_{-0.3}$	$171.7^{+0.0}_{-107.3}$	$0.35^{+0.00}_{-0.05}$	$7.00^{+0.76}_{-0.00}$	25.5 ± 0.7
N42_11065-D	2	12:36:32.24	62:09:46.5	25.4	3.658	$2.1^{+0.2}_{-0.8}$	$20.8^{+20.8}_{-0.4}$	$0.10^{+0.05}_{-0.00}$	$8.06^{+0.05}_{-0.54}$	25.1 ± 0.4
N32_14225	2	12:36:40.58	62:10:41.1	26.0	3.245	$11.7^{+7.2}_{-5.1}$	$49.2^{+42.9}_{-19.7}$	$0.30^{+0.05}_{-0.05}$	$8.46^{+0.45}_{-0.55}$	24.1 ± 0.2
N32_16805	2	12:36:47.57	62:10:23.7	25.9	3.235	$7.6^{+0.0}_{-0.6}$	$69.0^{+2.2}_{-0.0}$	$0.30^{+0.00}_{-0.00}$	$8.11^{+0.00}_{-0.05}$	23.9 ± 0.1
N32_15430	2	12:36:43.79	62:11:20.0	25.8	3.237	$3.8^{+2.5}_{-0.5}$	$272.7^{+45.4}_{-151.6}$	$0.40^{+0.00}_{-0.05}$	$7.16^{+0.60}_{-0.14}$	23.9 ± 0.1
N32_19795	2	12:36:54.94	62:11:43.8	25.1	2.976	$16.7^{+0.0}_{-1.3}$	$168.6^{+5.1}_{-0.0}$	$0.35^{+0.00}_{-0.00}$	$8.06^{+0.00}_{-0.05}$	23.2 ± 0.1
N33_23907-D	2	12:37:05.48	62:12:37.1	25.8	3.678	$2.2^{+2.6}_{-1.7}$	$11.6^{+48.5}_{-4.9}$	$0.10^{+0.10}_{-0.05}$	$8.36^{+0.60}_{-1.36}$	25.1 ± 0.4

Table 4.1—Continued

ID	Mask	RA	Dec	m_{z850}	z	Mass / $[10^9 M_\odot]$	SFR $[M_\odot\ \mathrm{yr}^{-1}]$	E(B-V)	$\log_{10}$(age / yr)	m_{Ks}[b]
N33_20428	2	12:36:56.48	62:13:39.9	26.8	3.436	$2.9^{+4.3}_{-2.5}$	$7.8^{+57.5}_{-3.1}$	$0.15^{+0.15}_{-0.05}$	$8.66^{+0.60}_{-1.66}$	24.6 ± 0.3
N33_18453	2	12:36:51.69	62:15:10.1	25.8	3.364	$0.2^{+0.1}_{-0.0}$	$25.0^{+0.0}_{-6.8}$	$0.10^{+0.00}_{-0.00}$	$7.00^{+0.34}_{-0.00}$	24.4 ± 0.2
N32_18454	1	12:36:51.69	62:12:15.1	26.5	$3.88^{+0.17}_{-0.25}$	$1.2^{+0.5}_{-0.4}$	$2.9^{+4.5}_{-0.3}$	$0.00^{+0.10}_{-0.00}$	$8.71^{+0.15}_{-0.55}$	< 26.3
N42_7643	2	12:36:22.00	62:09:12.7	26.5	$2.70^{+0.10}_{-0.20}$	$4.3^{+1.3}_{-0.9}$	$169.1^{+31.7}_{-102.8}$	$0.50^{+0.00}_{-0.05}$	$7.44^{+0.52}_{-0.12}$	24.1 ± 0.2
N42_10036	2	12:36:29.20	62:08:53.5	27.3	$2.92^{+0.21}_{-0.19}$	$5.8^{+9.0}_{-2.7}$	$5.8^{+21.8}_{-3.6}$	$0.20^{+0.15}_{-0.10}$	$9.11^{+0.84}_{-0.90}$	25.0 ± 0.4
N42_10800	2	12:36:31.53	62:10:06.4	27.2	$2.92^{+1.06}_{-0.30}$	$0.1^{+0.1}_{-0.0}$	$7.2^{+5.1}_{-5.8}$	$0.15^{+0.05}_{-0.15}$	$7.00^{+0.96}_{-0.00}$	< 26.3
N32_17776	2	12:36:50.09	62:10:23.7	26.0	$3.54^{+0.20}_{-0.24}$	$1.5^{+2.6}_{-1.0}$	$26.7^{+53.2}_{-13.6}$	$0.20^{+0.05}_{-0.05}$	$7.81^{+0.75}_{-0.81}$	25.4 ± 0.7
N42_13119	2	12:36:37.65	62:12:10.8	27.1	$3.13^{+0.60}_{-0.54}$	$0.5^{+1.4}_{-0.3}$	$26.1^{+37.3}_{-20.5}$	$0.30^{+0.05}_{-0.10}$	$7.26^{+1.25}_{-0.26}$	< 26.3
N32_15794	2	12:36:44.77	62:11:45.8	26.9	$3.54^{+0.20}_{-0.29}$	$1.1^{+5.6}_{-1.0}$	$1.9^{+14.6}_{-0.3}$	$0.00^{+0.15}_{-0.00}$	$8.86^{+0.84}_{-1.86}$	< 25.6
N32_18900	2	12:36:52.71	62:11:37.3	25.9	$3.54^{+0.24}_{-0.13}$	$5.3^{+1.2}_{-1.2}$	$66.5^{+12.7}_{-26.6}$	$0.30^{+0.00}_{-0.05}$	$7.96^{+0.25}_{-0.15}$	24.8 ± 0.3

Note. — Sample IDs, coordinates, redshifts, and properties derived from SED fitting. Where appropriate, emission line flux has been subtracted from the K_S-band photometry before fitting to the photometry, using only the stellar continuum to determine SED properties. Mask '1' denotes objects observed on our Mar 20-21 mask, and '2' denotes those undetaken Apr 16-17. This table contains the full list of 28 objects we observed, with the 20 galaxies with secure spectroscopic confirmation listed first. The identifier '-D' denote objects with previously known spectroscopic redshifts from our DEIMOS campaign.

[a]When SFRs for this object is estimated using the dust correction from Meurer et al. (1999) and the UV continuum to SFR conversion of Kennicutt (1998), we find a much more modest rate of 150 $M_\odot\ \mathrm{yr}^{-1}$.

[b]Total measured K_S magnitude, including any line emission.

4.3.2 Observations

The targets defined above were observed using MOSFIRE (McLean et al. 2012) on the Keck I telescope. We observed two masks on separate observing runs, both using the K-band grating. The first mask was observed on the night of March 20-21, 2013 for a total of 4.25 hours integration time, of which $\simeq 1$ hour was affected by thin cloud. The average seeing for this mask was 0.75 arcseconds full-width at half maximum (FWHM). Our second mask was observed on the night of Apr 16-17, 2013. We obtained a total of 2.50 hours of useful integration time, including approximately 40 minutes with thin clouds, and an average seeing of 0.70 arcseconds FWHM.

We used an ABAB dither pattern with individual exposures of 180 seconds and a slit width of 0.7 arcseconds for all targets. On each mask, in addition to our science targets, we also included a star with $K_{AB} < 19.0$. Using the longslit mode of MOSFIRE, also with a 0.7 arcsedond slit, we observed an A0V star at twilight during each of our runs. Flux calibration was performed using two methods. In the first, we use a spectrum of Vega from the HST CALSPEC database[1], scaled to the K_s magnitude of our A0V standard to determine the sensitivity as a function of wavelength.

In the second method, we use the observations of our standard star to determine the shape of the sensitivity, but set the overall normalization using the star placed on each of our masks. This is done by matching the average flux for the star in wavelengths probed by the K_s band to the value measured in the Wang et al. (2010) K_s photometry. This method has the advantage of intrinsically accounting for the effects of thin cloud and slit loss due to seeing and pointing error during our observations. Its disadvantage is the lack of knowledge of the spectral type of the calibration star. Reassuringly, the two methods agree to within 10%, so we chose to utilize the second method in order to better account for the cloud encountered during our observations. For our analysis, we assume a 15% error on the flux calibration in all calculations.

The data was reduced using the publicly available MOSFIRE data reduction pipeline[2]. Briefly, the pipeline first creates a median, cosmic-ray subtracted flat field image for each mask. Wavelength solutions for each slit are fit interactively for the central pixel in each slit, then propagated outwards to the slit edges to derive a full wavelength grid for each slit. Background subtraction is handled as a two stage procedure. First, individual stacks of all A frames and all B frames, which are then used to produce A-B and B-A stacks. As the A and B frames are temporally interleaved, this provides a first level of subtraction. Secondly, a 2-D b-spline model is fit to the residuals in each of these stacks, in a method similar to that described by Kelson (2003). The two stacks are then shifted, rectified, and combined, producing a positive source signal flanked by two negative signals at approximately half strength, separated by the dither length.

To determine the redshift of each source in our MOSFIRE spectra, we fit three Gaussians to the

[1] http://www.stsci.edu/hst/observatory/cdbs/calspec.html
[2] https://code.google.com/p/mosfire/

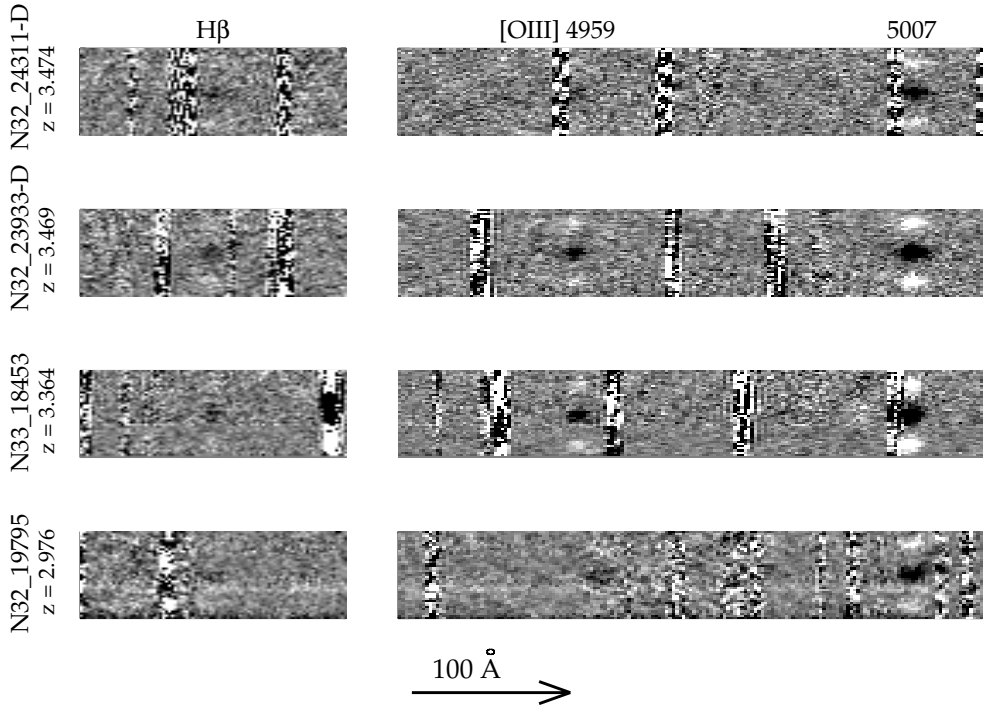

Figure 4.5 Example 2-D MOSFIRE spectra in A-B-A format for 4 targets showing prominent nebular emission. The left panels focus on the region containing Hβ and the right panels the [OIII] doublet (marked).

[OIII] 4959, 5007, and Hβ lines simultaneously, ignoring regions contaminated by nearby skylines. In the spatial direction, we chose the aperture of our 1D spectra to enclose at least 90% of the flux from the star on our mask, which resulted in a width of 9 pixels (1.6″). For line flux measurements, apertures in the spectral direction were set to extend from the line center to at least 2.5 times our measured dispersion (σ), typically resulting in $\sim 10-15$ pixels. Small corrections were made for flux expected to fall outside of these apertures.

In total we examined 28 targets, 20 of which are now securely established within the $3.0 < z < 3.8$ redshift range. Of these, 13 had pre-existing optical spectra from DEIMOS and 7 represent new MOSFIRE spectroscopic confirmations determined from our photometric sub-sample (Section 4.3.1.3). The remaining 8 galaxies display no detectable line emission in our MOSFIRE spectra (see Section 4.4.2 for discussion of these). Table 4.1 and Figure 4.4 summarize the salient properties of the final sample.

4.4 Analysis

The primary goal of this work is to verify or otherwise the conclusions of Section 4.2 which examined the equivalent width distribution for Hα emission for LBGs of known spectroscopic redshift in the range $3.8 < z < 5.0$. A significant conclusion from this study was the remarkably strong emission deduced by SED fitting. Using near-infrared spectroscopy with MOSFIRE we can not only directly measure the equivalent width distribution of [OIII] emission but also test the robustness of the SED-fitting approach by comparing spectroscopic line fluxes with those inferred from broad-band photometry.

Table 4.2. MOSFIRE Hβ + [OII] spectroscopic measurements

ID	flux$_{H\beta}$ [10^{-18} erg/cm/s]	flux$_{[OIII]}$ [10^{-18} erg/cm/s][a]	EW$_{H\beta}$ [Å, rest]	EW$_{[OIII]}$ [Å, rest][a]	$v_{neb} - v_{Ly\alpha}$ [km/s][b]	$\frac{flux_{pred,SED}}{flux_{obs}}$
N33_24311-D	13.5 ± 2.0	99.5 ± 3.2	140^{+240}_{-100}	1100^{+600}_{-200}	152 ± 23	0.91
N33_19880-D	5.9 ± 1.7	35.9 ± 3.9	89^{+196}_{-35}	600^{+550}_{-200}	4 ± 210	...
N33_25713-D	7.2 ± 2.3	21.7 ± 4.2	47^{+78}_{-29}	150^{+70}_{-30}	106 ± 100	...
N33_18549-D	22.5 ± 2.9	38.9 ± 2.5	170^{+240}_{-120}	300^{+100}_{-50}	319 ± 60	0.74
N33_19374-D	-3.0 ± 2.7	1.1 ± 4.7	< 7	< 21	xxx	...
N33_24278-D	-8.6 ± 3.2	32.8 ± 6.4	< 20	370^{+190}_{-120}	207 ± 173	...
N33_25726-D	9.5 ± 3.8	79.9 ± 8.0	40^{+61}_{-21}	360^{+60}_{-50}	86 ± 45	...
N32_20647-D	9.8 ± 3.6	56.2 ± 7.3	130^{+310}_{-40}	890^{+690}_{-320}	113 ± 71	...
N32_23933-D	14.0 ± 2.5	49.1 ± 3.8	40^{+49}_{-30}	150^{+20}_{-20}	195 ± 100	2.31
N32_15359	11.9 ± 2.1	54.8 ± 5.0	21^{+26}_{-17}	100^{+10}_{-10}	...	1.39
N42_7697-D	7.9 ± 6.2	18.6 ± 9.2	91^{+226}_{-5}	260^{+220}_{-160}	227 ± 98	...
N42_12130-D	5.5 ± 3.3	6.0 ± 4.4	65^{+196}_{-7}	150^{+210}_{-90}	xxx	...
N42_11065-D	2.0 ± 4.3	1.2 ± 7.3	< 80	< 120	xxx	18.74
N32_14225	7.2 ± 3.5	47.6 ± 9.0	32^{+65}_{-18}	280^{+100}_{-80}	...	...
N32_16805	20.7 ± 12.0	39.6 ± 5.8	79^{+162}_{-29}	190^{+50}_{-40}	...	1.42
N32_15430	11.3 ± 3.7	68.6 ± 5.2	50^{+82}_{-31}	340^{+80}_{-50}	...	1.01
N32_19795	8.4 ± 6.9	94.2 ± 7.5	17^{+29}_{-4}	190^{+20}_{-20}	...	1.60
N33_23907-D	6.0 ± 4.9	18.3 ± 6.3	54^{+139}_{-3}	210^{+200}_{-120}	xxx	...

Table 4.2—Continued

ID	flux$_{H\beta}$ [10^{-18} erg/cm/s]	flux$_{[OIII]}$ [10^{-18} erg/cm/s][a]	EW$_{H\beta}$ [Å, rest]	EW$_{[OIII]}$ [Å, rest][a]	$v_{neb} - v_{Ly\alpha}$ [km/s][b]	$\frac{flux_{pred,SED}}{flux_{obs}}$
N33_20428	8.1 ± 3.2	45.6 ± 4.9	84^{+164}_{-32}	500^{+280}_{-130}	...	...
N33_18453	9.6 ± 1.7	126.5 ± 3.9	320^{+860}_{-150}	4400^{+6200}_{-2000}	...	1.63

Note. — MOSFIRE emission line measurements for our sample.

[a]Includes contribution from both 4959 and 5007Å lines.

[b]'xxx' denotes DEIMOS objects for which the MOSFIRE emission lines were not robust enough to permit a velocity offset measurement. '...' denotes objects from our photometric sample.

4.4.1 Equivalent width distribution

Even a cursory inspection of our MOSFIRE spectra revealed the presence of many intense line emitters. Figure 4.3.2 shows the 2-D spectra for 4 targets showing strong emission where the continuum remains undetected. To assemble the equivalent width (EW) distribution, we considered all objects with a spectroscopic detection in either our DEIMOS or MOSFIRE campaigns (Table 4.1). Our sample of 20 objects spans $2.97 \leq z \leq 3.77$ with a median of $z = 3.47$. To determine the continuum level necessary to measure the EW, we corrected the K-band photometry for the observed fluxes of any emission lines seen in the MOSFIRE spectra. Where one of the [OIII] doublet lines was partially or fully obscured by a skyline, we assumed its flux, adopting a fixed 5007/4959 line ratio of 3.0. For our two spectroscopic targets for which no significant line fluxes were detected in our MOSFIRE data, we derived 1-σ upper limits for each nebular line EW. The photometry for one of our targets, N33_19374, is likely contaminated by a nearby object. In this case, we made no attempt to correct for the flux falling inside our apertures from other objects, but estimate the EW as a lower limit.

Equivalent widths and errors were measured using a Bayesian Monte Carlo technique. Because our equivalent widths depend on the measured line fluxes both directly and indirectly, through the subtraction of the emission component from the K_S-band photometry, accurate errors are non-trivial and can be asymmetric. To account for this, we run a Monte Carlo simulation with N = 10000 trials for each galaxy. This simulation takes the actual measured line fluxes and K_S photometry, perturbs each by the appropriate error, then calculates the appropriate continuum magnitude and EWs. At each step, we apply a prior that the fluxes must not be negative, to ensure a distribution that reflects reality. For any galaxies with a line flux measured at less than 1σ, we instead calculate a 1σ upper limit in the same manner, given by smallest EW greater than the value of 68% of our Monter Carlo trials.

Table 4.2 presents the spectroscopic line measures and the rest-frame EW distribution of [OIII] 4959 + 5007 is presented in Figure 4.6. It is immediately clear that most have very intense emission lines with a median [OIII] EW_{rest} of 280 Å. There is a significant tail to much higher values; two galaxies have $\mathrm{EW}_{rest} > 1000$ Å, where the K_S-band photometry is dominated by line emission. Importantly, we see no significant difference in the distribution for those galaxies selected on the basis of their DEIMOS spectroscopy and those photometrically selected entirely for this study.

4.4.2 Comparison with Section 4.2

Although the foregoing suggests that intense line emission, sufficient to significantly influence the broad-band photometry, is quite a common property of $z \simeq$ 3-4 LBGs, we now turn to whether the EW distribution within the present sample of 20 LBGs supports the conclusions of our earlier

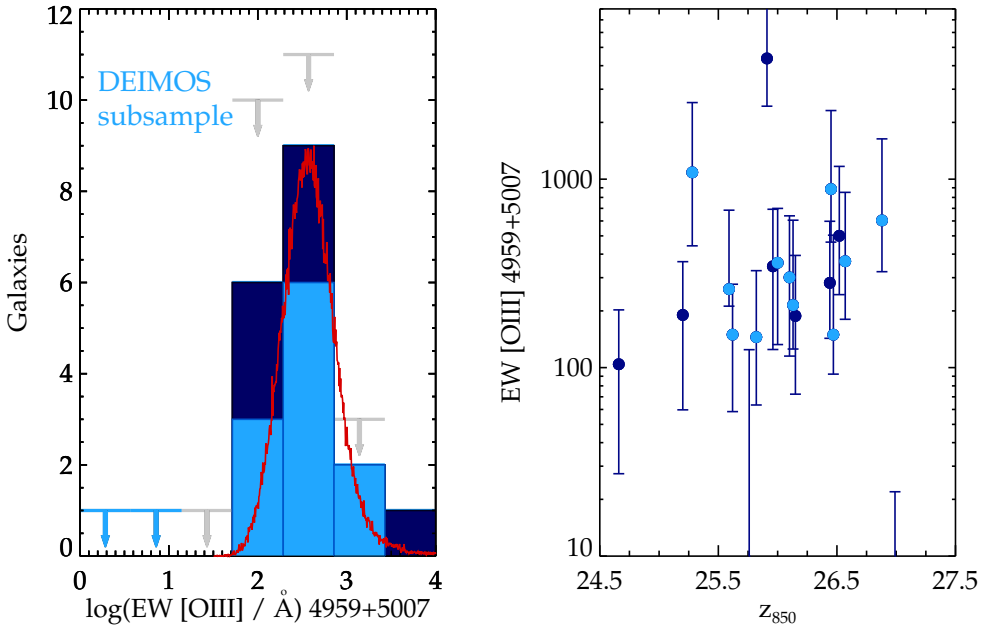

Figure 4.6 Left: The rest-frame equivalent width distribution of [OIII] 4959 + 5007 Å derived from our MOSFIRE spectroscopic data. The red curve estimates the distribution expected from the distribution for Hα derived from SED fitting method in Section 4.2. Light blue downward arrows indicate secure upper limits from our DEIMOS sample with previously known redshifts. Grey downward arrows indicate upper limits for the 8 objects in our photometric sample that display no strong lines, but which may not lie in the required $3.0 < z < 3.8$ redshift range. Right: Individual equivalent widths of [OIII] versus z_{850} magnitude. In both panels, light blue denotes the spectroscopic sample and dark blue the photometric sample (see Section 4.3.1).

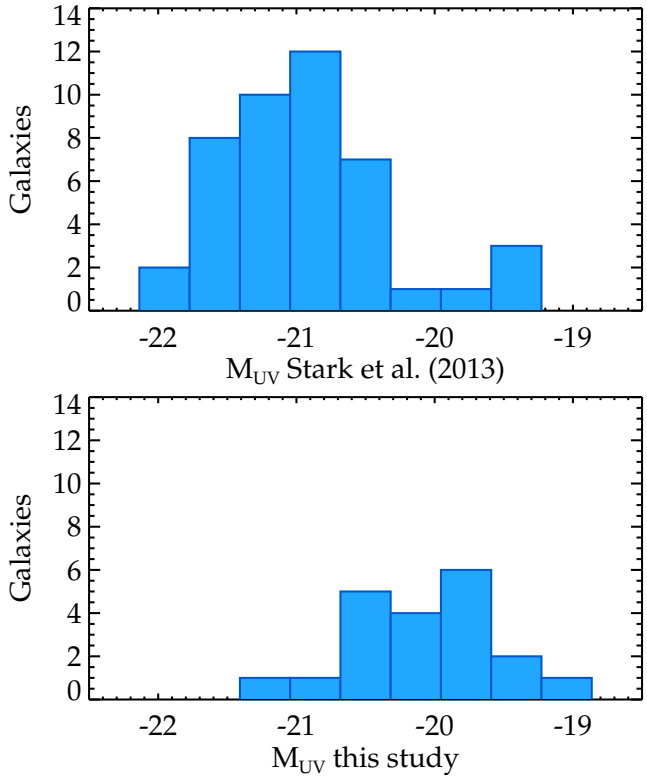

Figure 4.7 Absolute UV magnitude distribution for the $3.8 < z < 5.0$ sample discussed in Section 4.2 (top panel) compared to that at $3.0 < z < 3.8$ studied in this paper. Here we only include the 20 galaxies spectroscopically confirmed at $3.0 < z < 3.8$.

attempts to the EW_{rest} distribution of $H\alpha$ from a larger sample of 45 LBGs with $3.8 < z < 5.0$ using SED fitting.

Firstly, it is important to determine whether the LBG samples in the two studies are broadly comparable. In Figure 4.7 we demonstrate that the UV luminosity distribution for the two samples are fairly similar, with a median absolute magnitude M_{UV} = -21.0 for the $3.8 < z < 5.0$ objects compared to M_{UV} = -20.0 for our present sample. Since the UV luminosity correlates closely with the star formation rate and prominence of Lyman α emission (Stark et al. 2010), this suggests that their nebular emission properties should not be too dissimilar. However, it is important to keep in mind that studies at lower redshift (e.g., Erb et al. 2006; Fumagalli et al. 2012) have found Hα equivalent widths to increase with decreasing mass (and thus decreasing M_{UV}, through the M_* - M_{UV} relation).

Earlier, we found that the strength of Hα emission at $z \simeq 4.5$ could be fit well by a log normal distribution with $\langle \log_{10}(EW_{rest}/\text{Å}) \rangle = 2.57$ and $\sigma = 0.25$. To facilitate a comparison with the present [OIII] data, we adopt a value of 2.2 for the flux ratio of [OIII] to Hα, taken from the

empirical compilation of Anders & Fritze-v. Alvensleben (2003). This ratio is appropriate for a metallicity $Z = 0.2Z_{\odot}$, consistent with that inferred from a stack of LBG spectra at $z \sim 4$ (Jones et al. 2012), as well as measurements of ionized gas in LBGs at $z \sim 3.5$ (Maiolino et al. 2008). We caution that this ratio will change slightly with the stellar population age, but as most ionizing photons arise from stars with $t < 10$ Myr, such an effect should be very small.

To simulate the expected [OIII] EW_{rest} distribution, we must also account for noise in both the K_S-band photometry and the line fluxes, which we incorporate using a Monte Carlo distribution using the uncertainties quoted earlier. The result is the curve in Figure 4.6 which provides a good fit to the MOSFIRE data and a secure confirmation of large nebular line equivalent widths.

Importantly, we also wish determine the best fit lognormal distribution to our measurements of [OIII] EW, but such a measurement must account for the 8 photometrically selected galaxies that exhibit no detectable emission. To understand these, we must consider how well our photometric redshift code can predict the spectroscopic redshifts we actually observe. Considering the 7 photometrically selected galaxies we confirm with MOSFIRE, we find a median $\frac{|z_{best}-z_{spec}|}{\sigma_z} = 0.89$, which instills confidence in the accuracy of our errors. We then consider the photometric redshift distributions of all 15 photometrically selected objects, and calculate what fraction of the total $p(z)$ falls within the $3.0 < z < 3.8$ range for which we are sensitive to emission. We find an expected value of 11.5, indicating that on average 3.5 out of the 8 undetected galaxies will be undetected because their redshifts lie out of the range covered by our spectroscopy.

However, as we cannot determine which galaxies lie outside the detectable range and which have emission too faint to detect, we consider two extreme cases: (1) all these galaxies lie outside the $3.0 < z < 3.8$ redshift range, and we can thus ignore them when deriving distribution properties, or (2) all 8 galaxies lie within this range, but their line fluxes are below our detection limits. For the second case, we assume that the line EWs are distributed with a flat prior in log space between their derived 1σ upper limit (shown as grey downward arrows in 4.6) and 0. Assuming case 1 (2), we find best fit parameters of $\langle \log_{10}(EW_{rest}/\text{Å}) \rangle = 2.4$ (2.3) and $\sigma = 0.35$ (0.5). Thus, even in the pessimistic scenario, our spectra still support the strong line emission observed from these sources on average.

Since we also observe the Hβ line in many of our MOSFIRE spectra, albeit at low significance, this provides an additional check on the expected strength of Hα at these redshifts. To compute the expected Hα flux, we assume a Case B recombination Hα to Hβ flux ratio of 2.87:1, and compute the differential reddening from the best fit SED for each galaxy, assuming a Calzetti reddening law (Calzetti et al. 2000). This yields a predicted Hα flux for each object. The stellar continuum at the location of Hα is likewise estimated from the each best-fit SED. To avoid biasing our estimate to only galaxies with strong emission lines, we compute an average Hα EW for only the 13 galaxies with DEIMOS spectra in our sample, and do not weight the values inversely to their errors while

averaging. We then find a value of $EW_{rest}(H\alpha) = 380$ Å, providing further support for the strong lines inferred by our earlier analysis.

4.4.3 Verifying the SED fitting method

In addition to verifying that our MOSFIRE data on [OIII] emission is broadly consistent with the inferences for Hα deduced from SED fitting, we can perform one final check by applying the SED fitting method used earlier to the present sample and compare the inferred [OIII] fluxes with those measured directly in the near-infrared spectra.

We utilize Bruzual and Charlot 2007 (CB07) library of synthetic spectra. For simplicity, we only consider models with a constant star formation history, age ≥ 10 Myr, and a metallicity of Z = 0.2 $Z_{\odot}$, consistent with observations of Lyman break galaxies at $z \sim 3$ (Shapley et al. 2003). We utilize the Calzetti et al. (2000) prescription for reddening, varying E(B-V) in steps of 0.025. Synthetic fluxes are calculated for each filter, and the χ^2 computed for each model to assess its likelihood.

For all objects with either an IRAC [3.6] or [4.5] detection, we predict the [OIII] line flux using the SED fitting technique adopted earlier. We fit our grid of stellar continuum models to the observed photometry of each galaxy, excluding the K-band. For the best fitting SED, we then compute a synthetic K-band flux, and determine the emission line strength from the residual. This can only be applied for 8 galaxies from Table 4.1 for which a detection is available in at least one IRAC filter.

We list the ratios of the SED-predicted flux to that actually observed for the 8 objects in Table 4.2. Overall, the results are in good agreement: only one object, N42_11065 , is a catastrophic outlier, with a significant [OIII] flux implied from the SED method, but with none observed with MOSFIRE. The remaining 7 objects all have predicted to observed fluxes within a factor of 2.5, and 6 are within a factor ≤ 1.6. Such an agreement provides a clear validation that the technique we used in Section 4.2 can provide line strength measurements suitable for statistical purposes.

4.4.4 Revised stellar mass density

Now that we have both demonstrated the presence of strong nebular contamination in Spitzer/IRAC photometry, as well as validated the method used to derive this with direct MOSFIRE spectroscopy, we are in a position to update previous measurements to the high-redshift stellar mass density. Most previous measurments (e.g., Stark et al. 2007; Eyles et al. 2007; González et al. 2010) assumed that the entirety of the rest-optical flux is emitted by the stellar continuum which, as we have shown, will overestimate stellar massed.

We proceed in a similar fashion to (González et al. 2011), but with the addition of a correction for nebular emission. The first step in our method involves creating a corrected log $M_{\star} - M_{UV}$ relationship, which we will later use to assign a mass for a given UV luminosity. We derive this

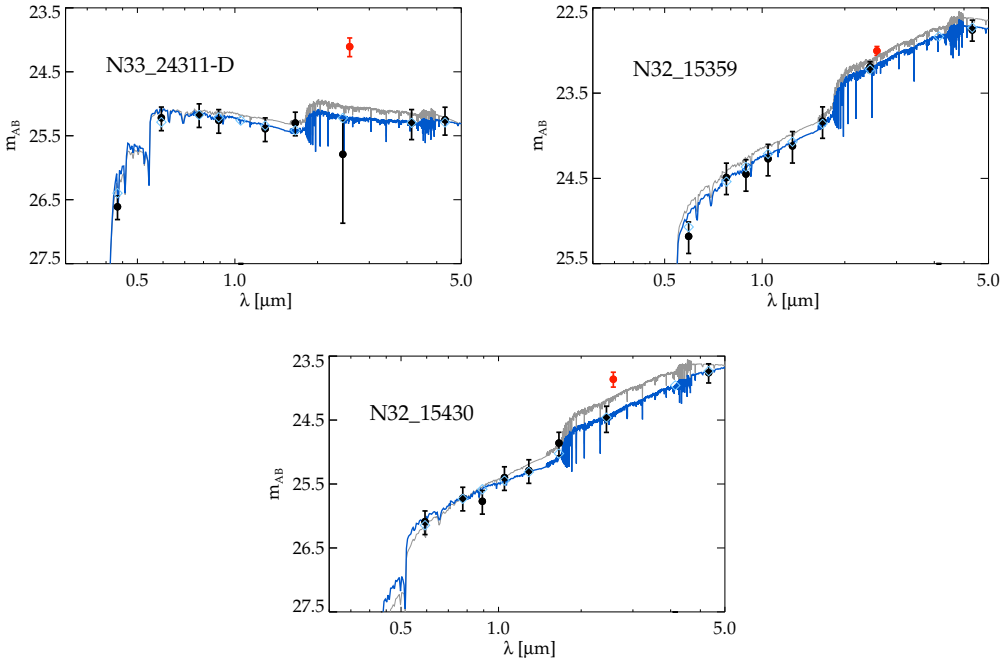

Figure 4.8 Spectral energy distributions for three of our targets. The red data point represents the observed K-band photometry without correction for [O III] contamination, and the grey spectrum shows the best fit SED to this data. The black K-band data point shows stellar continuum flux after correction for the MOSFIRE-determined [O III] line flux, and the blue spectrum is the associated best fit SED.

relationship for $B-$, $V-$, $i'-$, and z-band dropout populations, with median redshifts of $z \sim 4$, 5, 6, and 7. To focus on the average properties of the populations, we fit stellar (Bruzual & Charlot 2003) continuum models to SEDs stacked in bins of UV magnitude from Labbé et al. (2010) and Gonzalez et al. (2012). Both studies take advantage of WFC3 photometry in the UDF and goods fields. The number of objects within each stack ranges from > 100 for the B-band dropouts to $\simeq 10$ for individual bins of i'-drops.

To calculate the nebular line contribution, we assume a flux ratio of ([OIII] + Hβ) / Hα of $\sim 1.7 - 2.0$, with the exact value drawn at random from a uniform distribution between these two numbers. This is consistent with actual measurements at $z \simeq 2 - 3$ (e.g., Hainline et al. 2009; Erb et al. 2010). For each bin at each redshift, we then perform a Monte Carlo simulation that draws a redshift at random from the selection function, and an Hα (and thus Hβ and [OIII]) EW from our best fit EW distribution. If these lines fall within one of the IRAC filters given the selected redshift, we subtract the line flux to derive an estimate of the stellar continuum only flux measurement. Each realization of this process is then individually fit with a (Bruzual & Charlot 2003) SED, with the data point provided by the median fit stellar mass for all these realizations and 1σ error bars from the 68% spread of the distribution in mass. At all redshifts, we assume that the nebular line strengths follow our measured $3.8 < z < 5.0$ Hα EW distribution, but at $z \sim 6$ and 7, we also consider a model where the characteristic EW increases as $(1+z)^{1.8}$, shown to be a good fit to the evolution at lower redshift by Fumagalli et al. (2012). The results are plotted in Figure 4.9, and demonstrate the importance of taking these corrections into account. We find that the average stellar masses are reduced by factors of $\times 1.1, 1.3, 1.6$, and 2.4 for populations centered at $z \simeq 4, 5, 6$, and 7, respectively. At $z \simeq 6$ and 7, if nebular line strengths instead increase as $(1+z)^{1.8}$, we find masses overestimated by factors of $\times 1.9$ and 4.4 instead. Indeed, Smit et al. (2014) have recently provided evidence for such an increase, measuring a median [OIII] + Hβ EW of ~ 1800 Å with a similar technique for a sample of seven lensed galaxies at $z \sim 6.6 - 7.0$.

To derive the corrected stellar mass densities, we must combine the $\log M_\star - M_{UV}$ relationship with a measured UV luminosity function, as these galaxies are selected on the basis of their UV luminosity, and not their stellar mass. We extract a large number ($N = 10^5$) of luminosities from the measured UV LFs of Bouwens et al. (2007) and Bouwens et al. (2011) at $z = 4, 5$ and $z = 6, 7, 8$, respectively. From each of these UV luminosities, we then extract a mass from the nebular-corrected $\log M_\star - M_{UV}$. Rather than relying on the individual data points, we compute a linear slope and normalization of the relationship at $z = 4$, and leave the slope constant while refitting the normalization at each redshift according to our evolving EW model. To compute a tentative measurement at $z \sim 8$, we compute the SMD using the $z \sim 7$ $\log M_\star - M_{UV}$ relationship.

For accurate SMD measurements, it is also crucial to take into account the scatter in this relationship. González et al. (2011) found a value of 0.5 dex for the observed scatter at $z \sim 4$, which may

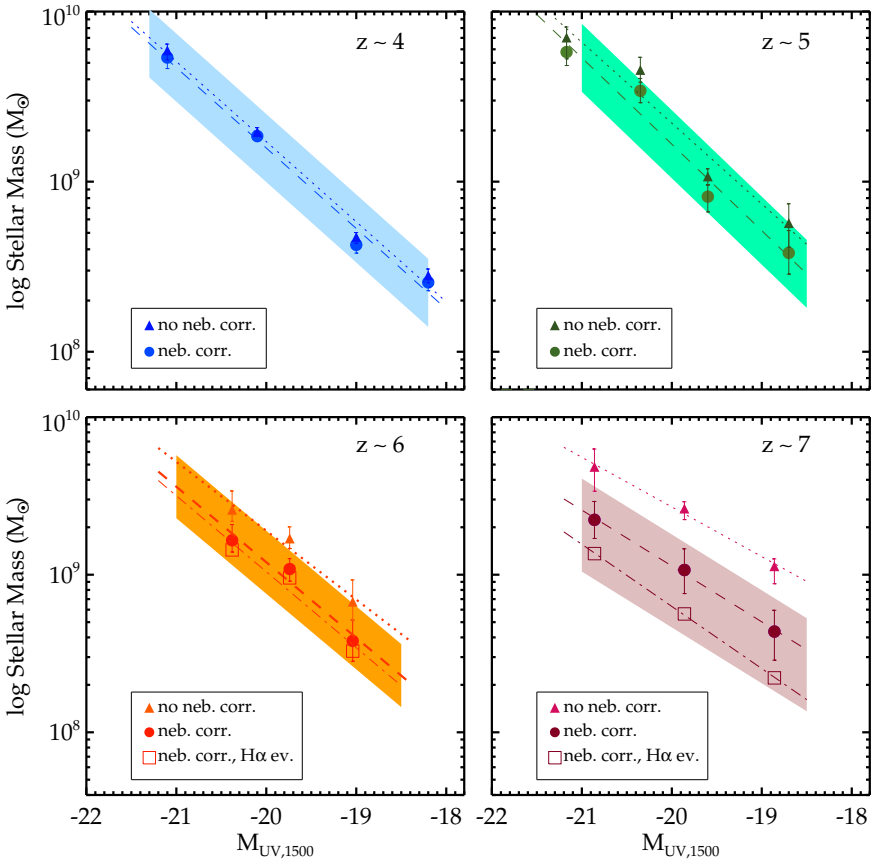

Figure 4.9 Stellar mass vs. UV absolute magnitude relationship at $z \sim 4, 5, 6, 7$. Solid triangles denote stellar masses without accounting for nebular emission, with the dotted line denoting the best-fit $M_\star - M_{UV}$ relation for these points. Closed circles show the masses once nebular emission is corrected for by the method in the text, assuming the measured EW distribution is constant with redshift, with the dashed line giving the corrected $M_\star - M_{UV}$ relation. Empty squares and the dot-dash line denote the same thing, assuming a model where EWs increase as $(1+z)^{1.8}$. The shaded regions indicate the range of stellar masses at a given M_{UV}.

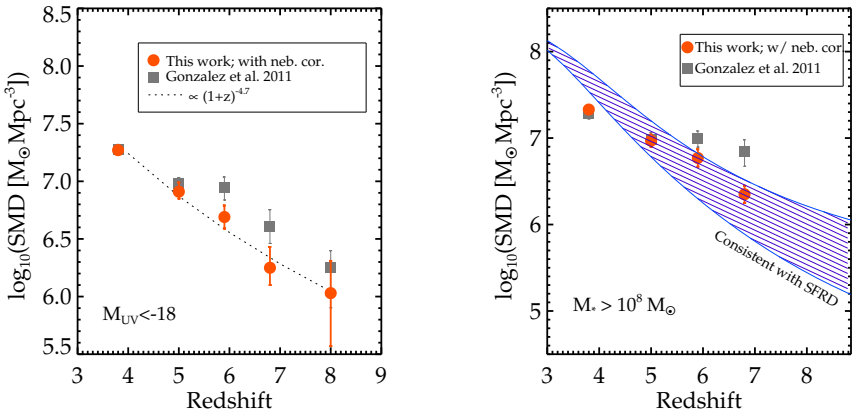

Figure 4.10 Stellar mass densities from this work, corrected for nebular emission contamination, at $4 < z < 8$ compared with uncorrected measurements from González et al. (2011). Both panels assume that the EW distribution increases with redshift from our $z \sim 4$ measurement as $(1+z)^{1.8}$, as suggested by Fumagalli et al. (2012).

include contributions from photometric noise, systematic uncertainties in the modeling, as well as the intrinsic scatter we are concerned with. We use this estimate of 0.5 for our calculations and note that should the intrinsic scatter be only 0.2, for example, our SMD measurements would decrease by a factor of 1.6-2.0.

The results of this exercise are presented in Figure 4.10, integrated both as a function of UV luminosity and stellar mass. In both cases, our stellar mass densities at $z \sim 6$ and 7 are significantly lower than the recent estimates of González et al. (2011), who do not take nebular contamination into account. At $z \sim 7$, this reduction can be up to 0.5 dex, significantly larger than the 0.1-0.2 dex uncertainties. More importantly, we can compare the resulting mass densities to those implied by integrating the star-formation rate densities derived from the UV luminosity function. We perform these calculations according to the prescription of Robertson (2010b), and find that although the old results were in significant tension with this prediction, once the nebular correction is applied, the measurements are in complete agreement at $z \sim 6 - 7$.

4.4.5 Lyα velocity offsets

Since we now possess a sample of $z \simeq 3.5$ galaxies with both optical and near-infrared spectra, we can comment briefly on the prevalence of outflows. A velocity offset is often observed between Lyα, which is easily resonantly scattered by hydrogen on its way out of a galaxy, and other nebular lines which trace directly the sites of star formation and provide a systemic redshift (e.g., Shapley et al. 2003). In particular, Lyα is often observed with a positive velocity offset, suggesting those photons are only able to escape after being scattered by an outflowing HI wind on the far side of the galaxy

and shifting out of resonance with any HI on the near side (Steidel et al. 2010).

Measures of this offset velocity at high-redshift can shed light on some outstanding issues related to cosmic reionization. Firstly, one of the major currently unknown variables that enters into reionization calculations remains f_{esc}, the escape fraction of ionizing photons from galaxies. Although recent measurements have found $f_{esc} \simeq 10\%$ at $z \sim 3$ (Nestor et al. 2013), direct measurements are impossible at higher redshifts, owing to the increased opacity of the intergalactic medium (IGM). A higher value ($\simeq 20\%$) is required to reproduce measurements of the IGM neutral fraction at high redshifts (e.g., Robertson et al. 2013; Kuhlen & Faucher-Giguère 2012). As any outflowing neutral gas will serve to extinguish ionizing radiation, an observed decrease in the velocity offset of Lyα, potentially indicating a lower covering fraction of neutral gas, would provide further support for an increased f_{esc}. The velocity offset is also of direct interest, as numerous experiments seeking to directly probe the ionization state of the IGM at $z > 6$ utilize the visibility of Lyα emission (e.g., Pentericci et al. 2011; Schenker et al. 2012; Ono et al. 2012). If Lyα escapes galaxies with a smaller velocity offset than previously believed, it is closer to resonance and more easily quenched by a neutral IGM.

To this end, we present the difference in the observed velocities of Lyα and the Hβ+[OIII] for all objects with at least a 3σ line detection in Table 4.2 and Figure 4.11. The left panel displays both stacked Hβ+[OIII] (black) and Lyα (red) profiles, demonstrating the high-fidelity velocity measurements we are able to make with MOSFIRE. In the right panel, we present a compilation of Lyα velocity offset measurements, plotted as a function of redshift and Lyα EW$_{rest}$.

As all of the 9 targets in our MOSFIRE sample show significant Lyα in emission (EW $>$ 20Å), we must be careful not to draw conclusions by blindly comparing this to the Steidel et al. (2010) sample at lower redshift, for which all objects have only modest equivalent widths. A more illuminating conclusion can perhaps be drawn by compiling the velocity offsets for other galaxies with strong Lyα emission, drawn here from McLinden et al. (2011), Finkelstein et al. (2011), and Hashimoto et al. (2013). All have quite low offsets, with $< v_{Ly\alpha} >= +149$ km s^{-1} for the entire sample of 17 objects, and $< v_{Ly\alpha} >= +157$ km s^{-1} for our own 9. As the fraction of starforming galaxies displaying strong Lyα emission increases with redshift out to at least $z \sim 6$ (Stark et al. 2010), this data implies it may become easier for ionizing photons to escape if this correlation of large EW$_{Ly\alpha}$ with $v_{Ly\alpha}$ trend is in fact caused by lower HI covering fractions.

We note here that a number of other recent papers support the association of larger Lyα equivalent widths with lower covering fractions of neutral gas at high redshift. Hashimoto et al. (2013) find that, for a stacked sample of four $z \sim 2$ Lyman alpha emitters, Lyα emerges redshifted from the systemic velocity by approximately the same amount as low ionization absorption lines are blueshifted by. This is in contrast to the theoretical predictions of Verhamme et al. (2006), which predict that such small velocity offsets will only occur for small HI column densities ($N_H < 10^{20}$). Additionally,

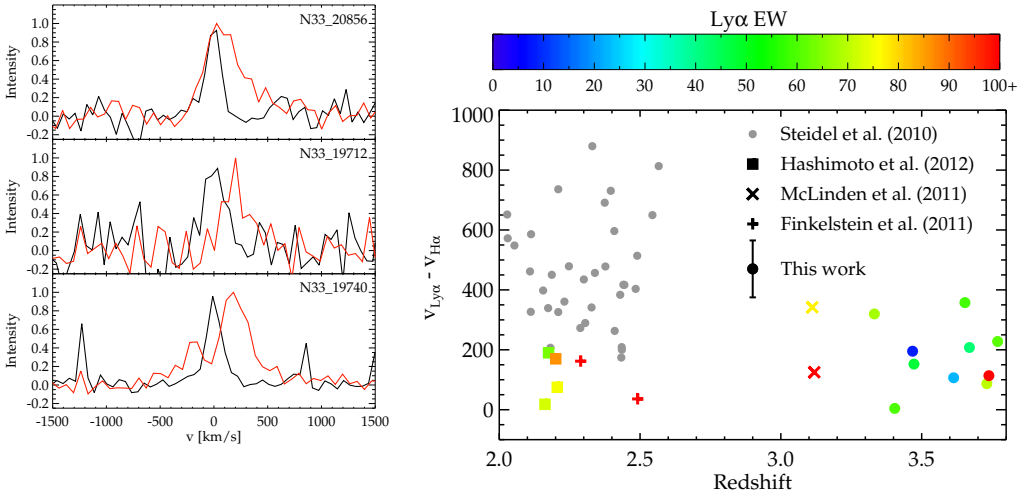

Figure 4.11 Left: The velocity structure observed by comparing MOSFIRE and DEIMOS spectra for three objects from our spectroscopic sample. Zero velocity is defined using a stack of the nebular [OIII] and H_β lines, shown in black. Lyα is overlaid in red, arbitrarily scaled in the y-axis. Right: Compilation of Lyα velocity offset measurements from various sources in the literature. The typical error bar for our sources is plotted in black. Our objects show much more modest offsets than the sample of Steidel et al. (2010), which all display only low level Lyα emission, but are more consistent with numerous LAEs from the literature, also plotted.

Jones et al. (2013) have explicitly derived the minimum covering fraction of neutral gas for a sample of lensed $z \sim 2-4$ LBGs with high resolution spectra, and found that this inversely correlates with the Lyα EW. By virtue of our vastly expanded sample here, doubling the number of LBGs for which simultaneous measurements of Lyα and rest-frame optical nebular lines are available, we have provided further evidence on the important role the neutral gas covering fraction may play in Lyα escape.

4.4.6 Lyα radiative transfer modeling

Recently, Hashimoto et al. (2014, in prep.) have attempted to model our MOSFIRE and DEIMOS spectra using a simple radiative transfer model to fit the Lyα line profiles and velocity offsets. In this section, we briefly present their results, compare them to those presented in Verhamme et al. (2008), and place them in context with the previous subsection.

This work uses the Monte Carlo radiative transfer code *MCLya* (Verhamme et al. 2006), which we briefly summarize here. To generate the output line profile and magnitude, the code assumes an idealized model of a singular clump of stars and gas surrounded by an expanding, spherical, homogenous, and isothermal shell of HI and dust, uniformly mixed. The intrinsic Lyα is calculated using SED fitting, with a FWHM set by the measured FWHM of the rest-optical nebular lines

from MOSFIRE. The model has four free parameters, which are then varied across a grid of values: the shell expansion velocity, neutral hydrogen column density, shell dust content, and shell velocity dispersion. The goodness of fit for the output spectrum is then evaluated by convolving it with the DEIMOS instrumental resolution (R $\sim$ 1560) and computing a χ^2 statistic pixel by pixel.

This fitting procedure is performed on 8 of the 9 objects for which we have both MOSFIRE and DEIMOS detections, with the remaining object, N32_23933 having Lyα too faint to fit. We list the resulting best fit parameters along with their 1σ uncertainties in Table 4.3. In particular, we focus on the three galaxies for which these parameters are particularly well-constrained N33_24311, N32_20647, and N42_7697.

To attempt to distinguish any difference between these galaxies, all of which have $\mathrm{EW_{Ly\alpha}} > 25$ Å, and a subset of LBGs without strong emission, we compare these results with a subset of three galaxies from Verhamme et al. (2008) with $\mathrm{EW_{Ly\alpha}} < 10$Å. The best fit parameters for these are also listed in Table 4.3. While it is difficult to draw any conclusions from such a small sample, the most notable difference between these two samples is certainly the difference in HI column density. While the median N_{HI} for our sample of strongly emitting LBGs is only $10^{19.1}$ cm^{-2}, for the Verhamme et al. (2008) sample it is over an order of magnitude larger, at $10^{20.7}$. In fact, all three measurements for our sample are at least an order of magnitude below those measured in the weak emitters. In contrast, both samples show shell expansion velocities with a range from $v_{exp} \sim 0-250$ km s^{-1}. This thus provides tentative evidence for the hypothesis put forth in the previous section, whereby LBGs with larger observed $\mathrm{EW_{Ly\alpha}}$ have smaller covering fractions/column densities of neutral Hydrogen. Though these results are certainly not conclusive, it is reassuring that this hypothesis holds even when full modeling of the line profile is considered.

Table 4.3. Lyα radiative transfer best-fit parameters

ID	$EW_{Ly\alpha}$Å	v_{exp} [km s^{-1}]	$\log_{10}(N_H$ / cm$^{-2})$	τ	b [km s^{-1}
N33_24311	48	14^{+49}_{-14}	$19.6^{+0.2}_{-0.3}$	0.0 ± 0.0	14^{+10}_{-4}
N32_20647	270	250^{+110}_{-70}	$18.7^{+0.2}_{-1.5}$	$1.4^{+1.7}_{-1.1}$	15^{+10}_{-5}
N42_7697	61	57^{+42}_{-35}	$19.1^{+0.4}_{-0.6}$	$0.1^{+0.3}_{-0.1}$	21^{+14}_{-11}
1337	6.7	200	20.7	1.0	20
5550	6.3	200	20.7	1.5	20
7539	6.8	25	20.7	0.5	40

Note. — Best fit parameters from the Lyα radiative transfer fitting of Hashimoto et al. (2014, in prep), using our DEIMOS + MOSFIRE data. For comparison purposes, we include the results from a subset of LBGs with significantly smaller $EW_{Ly\alpha}$ from Verhamme et al. (2008).

4.5 Discussion

We began this chapter with a study of nebular emission at $3.8 < z < 5$ using broadband photometry from the Spitzer telescope combined with spectroscopic redshfits. Knowledge of the precise galaxy redshift allowed us to isolate a sample for which the Hα emission line fell within the [3.6] filter, while the adjacent K_s and [4.5] filters remained free from any emission lines. By fitting SEDs to the photometry which include only light from the stellar continuum and measuring the difference between the synthetic and observed photometry, we derived a characteristic Hα equivalent width of ~ 280 Å. Through near-infrared spectroscopy with MOSFIRE, we then were able to verify the main conclusions of this earlier work. A significant fraction of our 20 MOSFIRE-targeted LBGs targets show intense [O III] line emission and the EW distribution is broadly comparable with that inferred for Hα from SED fitting for the $3.8 < z < 5.0$ sample. Moreover, where we can make a direct comparison for objects with line measurements (or upper limits) from MOSFIRE, the SED fitting method predicts [O III] line fluxes that are in reasonable agreement given the uncertainties, with those measured directly.

One might worry that because our DEIMOS-confirmed objects mostly display large Lyα equivalent widths (a result of following up only secure confirmations with MOSFIRE) that we are biasing our sample toward especially strong emitters. However, our additional photometric sample of 7 objects dissuades this notion. Although the samples remain modest in size, not only does the EW distribution appear similar (Figure 4.6), but our largest equivalent width object, N33_18453, is also part of this photometric sample. Without optical spectra for these objects, we cannot completely rule out that these galaxies do not all display strong Lyα, but our prior work provides a statistical argument that this is not the case. Using the probabilities derived in Stark et al. (2011) for $z \sim 4$ LBGs to exhibit strong ($\mathrm{EW}_{rest} > 25$ Å) Lyα, we only expect ~ 2.0 galaxies in our photometric sample of 7 confirmed galaxies.

We can also examine, for our present sample, how our measured line emission affects the derived physical properties. Figure 4.8 presents SEDs for a selection of our sample where the excess flux in the K_S band is clearly visible. We can fit the SEDs using both the entire photometric dataset, including the line-contaminated Ks filter, as well as that excluding the contaminated band. In both cases, we assume a stellar continuum only. In this trial, the median properties of the sample hardly change; there is no significant change in age, and the stellar mass is reduced by only 3% when correcting for line emission. This is because the IRAC [3.6] and [4.5] photometry provides a crucial measurement free from line contamination longward of the Balmer break. Thus the majority of existing measurements of SED-derived properties of LBGs at $z \sim 3$, which incorporate IRAC data, should not be significantly affected by [O III] emission, even though it is particularly intense.

A more illuminating test applies when the IRAC photometry is ignored, in which case the

K_S filter becomes the only photometric measurement beyond the Balmer break. This is a more appropriate test of how SEDs are fit at z $\sim$ 6-7, where both the [3.6] and [4.5] IRAC filters are contaminated by [OIII] and Hα, respectively. In this comparison, the implications of line emission are much more striking. The median mass for the line corrected SEDs is only 64% that of the mass determined using the contaminated photometry, and the median age is lowered by 30%. For the most intense emitters, N33_24311 and N33_18453, the masses can be reduced by factors of $\simeq$ 20.

We have demonstrated here, for the first time with both robust spectroscopy and significant sample sizes, the strength of nebular emission in $z \geq 3$ LBGs. The implications of such observations are extremely important for the high redshift universe. SED fitting at high redshifts must account for contamination of broadband filters by these strong lines to determine accurate stellar masses. To this end, we presented corrected stellar mass densities, showing that previous estimates may have overestimated these measurements by as much as $\sim$ 0.5 dex at $z \sim 7$. These lines also provide mounting evidence for a continued increase of the sSFR beyond $z = 2$, which has only recently been suggested.

Additionally, we have significantly increased the number of the $z \geq 3$ galaxies with measurements of Lyα velocity offsets. Through radiative transfer modelling, we then showed that these velocity offsets may decrease due to a decreasing column density of neutral hydrogen. The measurements of these precise offsets provide valuable input to models which seek to map out the universal neutral fraction through Lyα radiative transfer, and also bolster arguments for an increasing escape fraction with redshift. With the era of multi-object, near-infrared spectrographs just now beginning, prospects for further confirmation of these trends will be strong.

Chapter 5

An Improved Method for Estimatingthe Evolving Neutrality of the Intergalactic Medium

Abstract

The redshift-dependent fraction of color-selected galaxies revealing Lyman alpha emission, $x_{Ly\alpha}$ has become the most valuable constraint on the evolving neutrality of the early intergalactic medium. However, in addition to resonant scattering by neutral gas, the visibility of Lyman alpha is also dependent on the intrinsic properties of the host galaxy, including its stellar population, dust content and the nature of outflowing gas. Taking advantage of significant progress we have made in determining the line emitting properties of $z \simeq 4-6$ galaxies, we propose an improved method, based on using the measured slopes of the rest-frame ultraviolet continua of galaxies, to interpret the growing body of near-infrared spectra of $z > 7$ galaxies in order to take into account these host galaxy dependencies. In a first application of our new method, we demonstrate its potential via a new spectroscopic survey of $7 < z < 8$ galaxies undertaken with the Keck MOSFIRE spectrograph. Together with earlier published data our data provide improved estimates of the evolving visibility of Lyman alpha, particularly at redshift $z \simeq 8$. As a byproduct, we also present a new line emitting galaxy at a redshift $z = 7.62$, which supersedes an earlier redshift record. We discuss the improving constraints on the evolving neutral fraction over $6 < z < 8$ and the implications for cosmic reionization. We conclude by presenting a tentative detection of the CIII]λ1909 line in a $z = 7.213$ galaxy with MOSFIRE, demonstrating its potential as an alternative redshift indicator when Lyα is significantly quenched.

5.1 Introduction

The transition from a neutral intergalactic medium (IGM) to one that is ionized, and therefore transparent to ultraviolet photons, represents the latest frontier in our overall understanding of cosmic history. In addition to determining when this 'cosmic reionization' occurred, a key question is the role of star-forming galaxies in governing the process. Structure in the polarization of the cosmic microwave background suggests the reionization process occurred within the redshift interval $6 < z < 20$ (Hinshaw et al. 2013), and deep infrared imaging with Hubble Space Telescope has provided the first opportunity to conduct a census of galaxies during the latter half of this period (Ellis et al. 2013; Oesch et al. 2013). Recent progress in this area has been reviewed by Robertson et al. (2013) and Bromm (2013).

In the absence of significant numbers of high redshift QSOs or gamma ray bursts, the most immediately available probe of the evolving neutrality of the IGM beyond $z \simeq 6-7$ is the visibility of the Lyman alpha (Lyα) emission line in controlled samples of color-selected galaxies. Although a prominent line in star-forming galaxies at $z \leq 6$, as Lyα is a resonant transition, it is readily suppressed by neutral gas, both in the host galaxy and, if present, in the surrounding IGM. First proposed as a practical experiment using Lyman break galaxies (LBGs) by Stark et al. (2010), the idea followed earlier theoretical work by Miralda-Escudé et al. (2000), Santos (2004), and others.

Ground-based near-infrared spectroscopic surveys have now targeted various samples of color-selected Lyman break galaxies over $6 < z < 8$ allowing the construction of a redshift-dependent Lyα fraction, $\mathrm{x_{Ly\alpha}}$, which falls sharply from a value of $\simeq 50\%$ at $z \simeq 6$ (Stark et al. 2010) to less than 10% at and beyond $z \simeq 7$ (Pentericci et al. 2011; Schenker et al. 2012; Ono et al. 2012; Treu et al. 2012; Pentericci et al. 2014). Although converting this downturn in the visibility of the line into the volume fraction of neutral hydrogen, x_{HI}, is uncertain (Bolton & Haehnelt 2013), the prospects for improving the statistics of this test are promising given the arrival of multi-object instruments such as MOSFIRE on the Keck 1 telescope (McLean et al. 2012).

So far, this important measure of late reionization has been applied by adopting an empirical description of the demographics of Lyα emission in LBGs, parameterized according to the equivalent width (EW) distribution for various UV luminosities over the redshift range $3 < z < 6$ when the Universe is fully ionized. The trend is then extrapolated to higher redshifts in the form of a 'no evolution' prediction with the aim of rejecting this prediction at some level of significance (e.g., Schenker et al. 2012). As we discuss here, this method, now widely used, has several disadvantages. Recognizing these and noting the spectroscopic and optical and near-infrared imaging data of LBGs over $3 < z < 6$ has improved in scope and quality, in this paper we adopt a more physically-based approach to the visibility of Lyα in the vicinity of the host galaxy. Our new approach aims to predict its visibility in a high redshift galaxy on the basis of its measured UV continuum slope

that, in turn, contains information on the dust content, and stellar population, which both directly influence the strength of any Lyα emission. This approach has the distinct advantage that, for the new $z > 7$ samples being studied with MOSFIRE and other spectrographs, composite UV slopes for the population are usually available so that unnecessary extrapolation can be avoided.

The present paper is concerned with describing this improved Lyα fraction test and applying it to the first comprehensive set of spectroscopic data emerging from MOSFIRE. In addition to incorporating the earlier surveys conducted with Keck (Schenker et al. 2012; Ono et al. 2012; Treu et al. 2012) and FORS2 on the VLT (Pentericci et al. 2011), we present the first results from a survey of high quality Ultra Deep Field (UDF) targets that provides a valuable extension of the aforementioned studies. As part of this survey, we demonstrate a new Lyα-emitting galaxy at a redshift z=7.62 extending once again the frontier of spectroscopically-confirmed HST sources.

A plan of the paper follows. In Section 5.2, we introduce our new method for the Lyman alpha fraction test. Section 5.3 introduces the new compilation of $3 < z < 6$ data drawn from our now completed Keck spectroscopic survey (Stark et al. in prep.), and Section 5.4 contains an analysis of these data in the context of our new method. In Section 5.5 we introduce our new MOSFIRE data and apply our new method to both this data and that obtained earlier. Finally, we conclude with Section 5.6 in which we summarize the results of our recent search for CIII] at $z > 7$.

5.2 Lyman Alpha Fraction Test — A New Approach

Although the traditional Lyα fraction test as first proposed by Stark et al. (2010) has already provided meaningful constraints on the evolution of the IGM beyond $z \sim 6.5$, there are two limitations in the current methodology. Firstly, as inferring the presence of neutral gas in the intergalactic medium represents a differential measurement, it is necessary to assume a form of the distribution of the equivalent widths of Lyα emission *unprocessed by the IGM* for the galaxies at $z \geq 7$. Comparing this to the observed distribution allows the extinction imposed by the IGM, and through the application of theoretical models, the IGM neutrality to be derived. The current methodology splits the sample into UV-luminous and UV-faint bins, and tracks the Lyα fraction in each bin as a function of redshift. The IGM unprocessed distribution at $z \sim 7$ is then assumed to either be that observed at $z \sim 6$ for each bin, or a linear extrapolation of the $3 < z < 6$ data. However, as we cannot observe the sample at $z \geq 7$ in the absence of a neutral IGM, we can never know which, if either, of these assumptions is correct.

Secondly, the EW distribution used to predict the observable Lyα distribution has been characterized in many different ways, including an exponential (Dijkstra et al. 2011), a direct histogram (Schenker et al. 2012), a half Gaussian (Treu et al. 2012), and a half Gaussian with a constant probability tail (Pentericci et al. 2011). Though the distributions are largely similar, no detailed

comparison has been performed to determine which one optimally represents the $3 < z < 6$ data. We perform this in the context of assembling our model in Section 5.4.

The most fundamental question, however, is whether the *rest-frame UV luminosity* is the optimum parameter to predict the visibility of Lyα in the absence of any suppression by a partly neutral IGM. The approach, based on correlations first noted by Shapley et al. (2003), was adopted by Stark et al. (2010) as $M_{\rm UV}$ can be readily determined from the available photometry of distant galaxies together with a photometric redshift. However, $M_{\rm UV}$ is likely to be a coarse predictor of the Lyα EW as it ignores second order parameters such as metallicity, the stellar initial mass function, and dust content.

The *UV continuum slope* is a more natural choice as a basic variable, as it encodes each of these physical properties (Meurer et al. 1999). Lower metallicity and hotter stars produce more ionizing photons per unit UV continuum, thus driving $\rm EW_{Ly\alpha}$ upwards. Dust very efficiently absorbs Lyα photons given their large effective path lengths from the many scatterings required to escape an HII region. These changes also result in a bluer or redder UV continuum slope, respectively. Thus, as the UV slope reflects more of the parameters that likely govern $\rm EW_{Ly\alpha}$ compared to $M_{\rm UV}$, we should expect it to be a more robust predictor of the visibility of the line in high redshift samples.

Until recently, determining the UV continuum slope was only possible for a restricted subset of $z < 4$ B-dropouts. Stark et al. (2010) showed that within this subset, strong Lyα emitting galaxies have bluer UV continuum slopes than their non-emitting counterparts, but as there existed no high-quality infrared photometry in the GOODS fields at this time, it was necessary to parametrize distributions at higher redshift by their absolute magnitude. However, in addition to the now completed Keck spectroscopic survey of LBGs over $3 < z < 6$ (Stark et al. 2010, in prep.), the CANDELS HST imaging program (GO 12444-5, PI: Ferguson/Riess/Faber) provides the necessary data to explore the potential of the UV continuum slope as a predictor for $\rm EW_{Ly\alpha}$. The addition of Y_{105}, J_{125}, and H_{160} photometric data enables the derivation of accurate UV continuum slopes for catalogued galaxies, given for each source there is a minimum of 3 broad-band filters longward of the Lyman break. As such UV continuum slopes are now available for the growing body of $z > 7$ photometric galaxy samples (e.g., Dunlop et al. 2013; Bouwens et al. 2013), we can realize a Lyα fraction test that overcomes several of the issues associated with the earlier approach.

In the following, we discuss the new data for the Keck $3 < z < 6$ spectroscopic sample (Stark et al. in prep.) and analyze it in the context of a distribution function based upon the observed UV continuum slopes of the population. We then apply the method to an updated sample of near-infrared spectroscopic data beyond $z \simeq 6$.

5.3 Improved Post-Reionization Data

5.3.1 DEIMOS/FORS2 Spectroscopy

As discussed in Stark et al. (2010, 2011), the $3 < z < 6$ LBG candidates which form the basis of the post-reionization sample were targeted in the GOODS-N and S fields using the DEIMOS spectrograph on the Keck 2 telescope. The final catalog is being prepared for release by Stark et al. (in prep.). By retrospectively applying the same photometric selection criteria, a spectroscopic sample in the GOODS-S field using the FORS2 spectrograph on the ESO Very Large Telescope was added (Vanzella et al. (2009) and references therein). Full details of these spectroscopic campaigns can be found in the above referenced articles.

The GOODS-N sample consists of 393 LBG candidates targeted with DEIMOS observed over the course of 2008-2010. The targets include B-,v-, and i-drops, and the spectroscopically-confirmed sample spans a redshift range of $3.33 < z < 5.99$. Typical 10σ limiting Lyα fluxes for these targets ranged between 1.0-1.5 $\times 10^{-17}$ erg cm^{-2}s^{-1}.

The complementary FORS2 campaign (Vanzella et al. 2009) targeted 214 LBG candidates in GOODS-S between 2002 and 2006. These targets were, on average, brighter than those studied at Keck (see Stark et al. 2010, Figure 2), and the confirmed galaxies span a redshift range $3.19 < z < 6.28$. In total, the sample comprises 607 galaxies, 269 of which are spectroscopically confirmed. Further details of the sample will be presented in Stark et al. (in prep.).

5.3.2 Photometry

The primary advance in our analysis of the equivalent width distribution of Lyα in the above spectroscopic sample relates to the combination of the earlier HST ACS optical imaging data with new, deep WFC3/IR near-infrared data critical to assessing how Lyα emission correlates with the measured UV continuum slope. To reliably bring together the various imaging datasets, it is necessary to account for the significantly different point-spread functions (PSFs) between the ACS (FWHM $\sim$ 0.09") and WFC3/IR (FWHM $\sim$ 0.16") instruments. In the GOODS-S field, we utilized the published, PSF-matched catalog of Guo et al. (2013), which uses the publicly released v2.0 ACS and v1.0 WFC3 images, constructs stellar profiles to derive the PSFs in order to convolve the higher-resolution, shorter wavelength data, and performs isophotal photometry on the smoothed images.

For GOODS-N, we also utilized the publicly released v2.0 ACS images, but as no CANDELS WFC3/IR mosaic was released at the time of this analysis, we constructed our own. The first 13 (out of 18) epochs of GOODS-N observations, released as individual v0.5 mosaics, were combined using the routine SWARP (Bertin et al. 2002) with individual weights assigned according to the exposure time. PSF matching was implemented using the *ColorPro* program (Coe et al. 2006). A PSF was constructed for each filter by shifting and stacking $\sim$ 20 bright unsaturated stars. All objects were

detected using the H_{160} image, and colors were determined using matched isophotal apertures after degrading the resolutions of all other images to that of the H_{160} image.

5.4 Analysis

5.4.1 Lyman alpha and the UV continuum

The basis of our analysis relies on accurate determinations of both the Lyα equivalent widths ($\mathrm{EW_{Ly\alpha}}$), and ultraviolet slopes of our sample. Thus, we detail here the methodology used in determining both these quantities for use in our analysis.

In order to measure the UV slope for each object in our sample, we first used a custom photometric redshift code to determine the approximate redshifts of those galaxies without spectroscopic confirmation. The code fits a suite of synthetic fluxes from the Bruzual-Charlot (BC03, Bruzual & Charlot 2003) spectra to the available photometry. To determine the best-fit redshift, we marginalized across all other parameters (mass, dust extinction, and age), and used the maximum likelihood value.

We measure the UV continuum slope using the β formalism first introduced by Calzetti et al. (1994), where the flux is parametrized as $f_\lambda \propto \lambda^\beta$. In our fitting process, we include photometric filters with central rest wavelengths within the range defined by Calzetti et al. (1994), $1350 < \lambda/\text{Å} < 2600$. This range is also similar to that used previously in the literature (Bouwens et al. 2013; Rogers et al. 2013). As in Bouwens et al. (2013), we use the effective filter wavelengths appropriate for a $\beta = -2$ spectrum, since the measured UV slopes in our sample generally populate the $-2.5 < \beta < -1.5$ range, and an error floor of 0.05 mag, or 5%, for all filters.

A grid of power law slopes with $-3.5 < \beta < 0.5$ and $\Delta\beta = 0.01$ was fit to the observed photometry, and the relative likelihood of each computed using $p(\beta_i) \propto \exp(-\chi^2/2)$, appropriate for Gaussian distributed errors. This allows us to construct a likelihood curve for the UV slope of each galaxy, central to the fitting method we describe later. After the fitting, the image cutouts, photometry, and resulting $p(\beta)$ were manually inspected for each galaxy, flagging and removing objects with clearly deviant photometry or incorrect solutions. After this process, 297 of our sample of 393 galaxies in GOODS-N, and 154 of our 214 galaxies in GOODS-S remained. Galaxies removed were typically those adjacent to bright objects, for which accurate photometry could not be assured, and faint, distant $z \geq 5$ galaxies that appeared in the shallower CANDELS-Wide field for which accurate UV slopes could not be determined.

Measurements of the Lyα EW were taken from Stark et al. (in prep.), with errors computed using both the 1σ flux errors in the spectrum as well as errors in M_{UV}added in quadrature to produce a likelihood curve for $p(\mathrm{EW_{Ly\alpha}})$. For cases where Ly$\alpha$ was not spectroscopically detected, we assume one of three cases: (1) the line flux falls below the 10σ limit (typically 1.0-1.5 $\times 1.0^{-17}$ erg cm^{-2}s^{-1}),

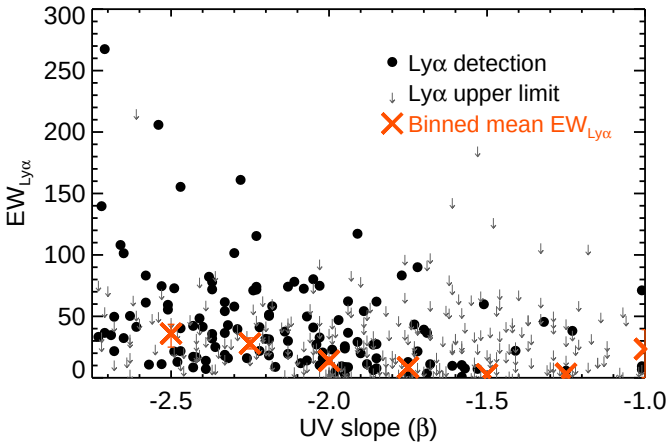

Figure 5.1 Compilation of our entire GOODS catalog of Lyα equivalent widths as a function of UV slope, β. Red triangles show the average EW, binned in steps of 0.25 in β, displaying a strong increase toward bluer slopes. This dataset forms the basis of our predictive model for Lyα emission incidence as a function of UV slope.

(2) the line emission, though brighter than the 10σ limit is missed, due to poor sky subtraction or obscuration by skylines, or (3) the object is a contaminant outside the expected redshift range. We discuss the implementation of this approach in Section 5.4.2.1.

With these results in hand, we now provide the basic evidence that the UV continuum slope of a galaxy, β, is a reliable predictor of its Lyα EW. In Figure 5.1, we plot the best fit β for each galaxy in our final sample against either its EW$_{\rm Ly\alpha}$, or its 10σ upper-limit, if a line is not detected. The red crosses denote the mean EW$_{\rm Ly\alpha}$in bins spanning $\Delta\beta = 0.25$, where undetected objects are set to have a value of 0. Error bars for each bin are calculated by bootstrap sampling.

As shown from earlier work by Shapley et al. (2003) and Stark et al. (2010), a clear trend of increasing mean EW$_{\rm Ly\alpha}$ with bluer (more negative) UV slopes is visible. With our large spectroscopic sample, this can be seen directly through the measures of individual objects, rather than via stacked spectra or consideration of average β values. Encouraged by this trend, we now develop a model that can predict the probability distribution of EW$_{\rm Ly\alpha}$ given a measured value of β, for example for a $z > 7$ galaxy. At the end of this section, we will also use this model to show that the UV slope is a more reliable predictor of EW$_{\rm Ly\alpha}$ than the absolute UV magnitude.

It is worth addressing why in Figure 5.1 so many of our galaxies appear to have $\beta < -2.0$. Although some groups have measured values of average $\beta \sim -2.3$ (e.g., Finkelstein et al. 2012b; Bouwens et al. 2013) at $z \sim 3$, the bluest slopes observed spectroscopically only $\beta \sim -2.0$ (Stiedel, personal communication 2014). To explore whether our measured values of β are reasonable given the population sampled, we compare them with the results from Bouwens et al. (2013), who conduct comprehensive measurements of β as a function of M_{UV} at $z = 4$, 5, and 6. Since all galaxies in

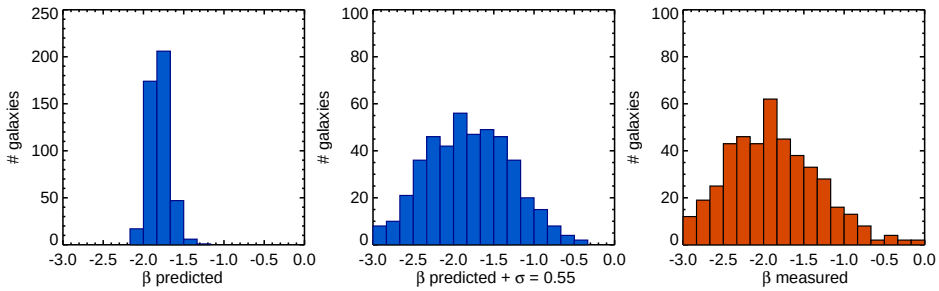

Figure 5.2 Left: Histogram of UV slopes expected for our DEIMOS sample using the observed absolute UV magnitude and the M_{UV} - β relationship derived in Bouwens et al. (2013). Since this relationship only accounts for the mean β in each UV magnitude bin, its scatter about the mean will be much lower than observed. The rightmost panel shows a histogram of actual observed β from our sample, while the center panel denotes the best fit to the observed value, which adds a scatter of $\sigma_\beta = 0.55$ to the relationship in the leftmost panel.

our sample have well-constrained absolute UV magnitudes and either photometric or spectroscopic redshifts, we then interpolate these M_{UV} - β relationships to predict values of β for our sample and compare them to our measurements.

We display the results in Figure 5.2. The leftmost panel displays a histogram of the predicted values of β for our sample, using our UV magnitudes and the M_{UV} - β relationships from Bouwens et al. (2013), while the rightmost panel shows our actual measurements. The median values of both samples lie at a diffrence of only $\delta\beta = 0.1$, with the predicted median at $\beta = -1.8$, and the observed median at -1.9. Immediately noticable is that the spread in the prediction is far lower than the spread in our actual observations, as the predictions only account for the average β at a given M_{UV}. Since the median error of the β of a typical galaxy in our sample is only 0.1, this variation may be due to an intrinsic spread in the values of β. To examine this, we conduct a Monte Carlo simulation where we add noise to the prediction shown in the leftmost panel to determine what total spread in β is needed to account for our observations. The middle panel shows the best-fit result, with $\sigma_\beta \simeq 0.55$. Studies have estimated the intrinsic scatter for UV-bright galaxies at $\sigma_\beta \sim 0.35 - 0.4$ (Bouwens et al. 2012a; Rogers et al. 2013), so our result is not unreasonable.

5.4.2 The UV slope-dependent EW distribution

We now seek to establish a formalism to predict the probability distribution for $\mathrm{EW_{Ly\alpha}}$ given a particular measured UV slope. As our goal is to improve the accuracy of the Lyman alpha fraction test, we first consider those galaxies with blue UV slopes likely to have strong Lyα emission before processing through the IGM.

5.4.2.1 Equivalent Width Distributions for a Fixed UV Continuum Slope

As an illustration of our new method we begin by examining the distribution of the Lyα EW for a fixed UV continuum slope, β. A natural choice is $\beta = -2.3$ given that Bouwens et al. (2013) found that faint ($M_{\rm UV} \geq -19$), high-redshift ($z \geq 6$) galaxies have slopes that asymptote to this value. Near-IR spectrographs such as MOSFIRE have begun to target these galaxies in earnest (this work; Finkelstein et al. 2013; Treu et al. 2013), and it is becoming increasingly important to characterize their expected IGM unprocessed Lyα emission. To construct a sample of galaxies for this task, we limit our overall sample of 468 galaxies with $3.19 < z < 6.28$ to those galaxies with a best fit value within $\Delta\beta = 0.25$ of -2.3, resulting in a total of 131 objects.

We now require a model to represent the IGM unprocessed EW distribution. In Appendix A, we review four such options using the methodology outlined here, and find that a lognormal distribution provides a significantly better fit than any of the others. In this case the natural logarithm of $\rm EW_{Ly\alpha}$ obeys a normal distribution. The two relevant parameters of the distribution, μ and σ, are typically referred to as the *location parameter* and *scale parameter*, respectively. They denote the mean of the natural log of $\rm EW_{Ly\alpha}$ and its variance. However, while the median of the distribution is given, as might be expected, by $\exp(\mu)$, the mean is slightly larger at $\exp(\mu + \sigma^2/2)$. A third parameter, A_{em}, determines the fraction of galaxies that have $\rm EW_{Ly\alpha} > 0$, as there is no reason a priori to expect all galaxies to display Lyα in emission. The resulting distribution can be written as:

$$\begin{aligned} p(EW) &= A_{em} \times \frac{1}{\sqrt{2\pi}\sigma \rm EW} \exp(-\frac{(\ln(\rm EW) - \mu)^2}{2\sigma^2}) \\ &+ (1.0 - A_{em}) \times \delta(EW) \end{aligned} \tag{5.1}$$

In Figure 5.3, we illustrate how the $\rm EW_{Ly\alpha}$ probability distribution function, p(EW), and the Lyα fraction, $\rm x_{Ly\alpha}$, change as these parameters are varied.

We now describe the Bayesian formalism we developed to evaluate the likelihood of the underlying parameters for our lognormal distribution, and determine which provides the best fit to the data. The entire set of spectroscopic Lyα observations is denoted as **Obs**; this contains the information for observations of each individual galaxy, $\rm Obs_i$. We can then denote the parameters for the model being fit as $\theta \equiv [\mu, \sigma, A_{em}]$. Our overall goal is to determine the probability distributions for the underlying parameters of each model, given our observations, i.e., $p(\theta|\mathbf{Obs})$. Using Bayes' theorem, we can rewrite this as:

$$p(\theta|\mathbf{Obs}) \propto p(\theta) \times p(\mathbf{Obs}|\theta) \tag{5.2}$$

Here, $p(\theta)$ represents our uniform priors for the underlying parameters, while the term on the

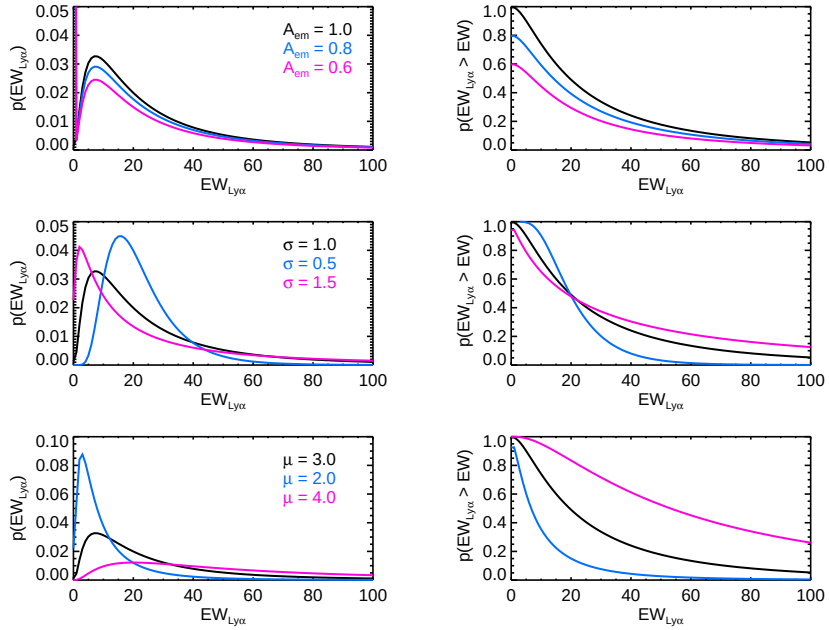

Figure 5.3 Example curves for how our lognormal model of $\mathrm{EW_{Ly\alpha}}$ distribution varies with each parameter. Left: Probability distributions for $\mathrm{EW_{Ly\alpha}}$. In each panel, the black curve has the same parameter values: $\mu = 3.0$, $\sigma = 1.0$, $A_{em} = 1.0$. From top to bottom, the two colored curves each display the effect of a change in a single parameter on the distribution. Right: Complementary cumulative distribution functions for the same parameters used in each left panel. This method of display is especially useful, as the Lyman alpha fraction, $\mathrm{x_{Ly\alpha}}$, for any $\mathrm{EW_{Ly\alpha}}$ can simply be read off the plot by finding the value of the curve at the desired $\mathrm{EW_{Ly\alpha}}$ along the x-axis.

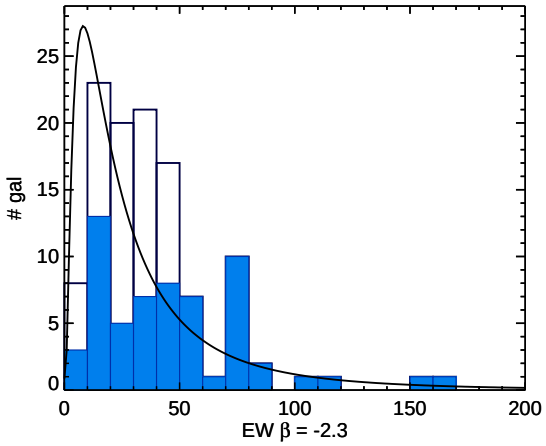

Figure 5.4 Histogram of our observed $\mathrm{EW}_{\mathrm{Ly}\alpha}$ detections (solid blue) and upper limits (unfilled black) for galaxies with best fit $\beta = -2.3 \pm 0.25$. Overplotted in solid black is our best fit lognormal model as described in Section 5.4.2.1

right hand side represents the probability of our observations given the model parameters. For any single object in which we measure a definite $\mathrm{EW}_{\mathrm{Ly}\alpha}$, this posterior probability can be expressed as:

$$p(Obs_i|\theta) = \int_0^\infty p(EW_{Obs,i})p(EW|\theta)dEW \tag{5.3}$$

In the case of an object for which Lyα remains undetected above our (10σ) limit, we compute the posterior probability as:

$$\begin{aligned} p(Obs_i|\theta) &= p(EW < EW_{10\sigma}|\theta) \\ &+ p(EW > EW_{10\sigma}|\theta) \times C_1 + C_2 \end{aligned} \tag{5.4}$$

Here, the first term represents the probability that the object intrinsically possesses an $\mathrm{EW}_{\mathrm{Ly}\alpha}$ below our detection limits, while the C_1 term takes into account incompleteness in the sample (caused by skylines or, in some cases, poor background subtraction). Contamination by low redshift sources is taken into account through the final term, C_2. We assume modest values for our contamination terms of $C_1 = C_2 = 0.05$, motivated by the completeness simulations of Stark et al. (2010), and the lack of low-redshift interlopers found in other spectroscopic follow-up surveys (Pentericci et al. 2011). The full posterior distribution for the parameters can then be computed by multiplying the individual posterior probabilities for each object. This allows us to infer the most likely values on parameters, as well as their marginalized and un-marginalized errors.

We display the best-fit distribution for our sample of 131 galaxies with $3.19 < z < 6.28$, over-

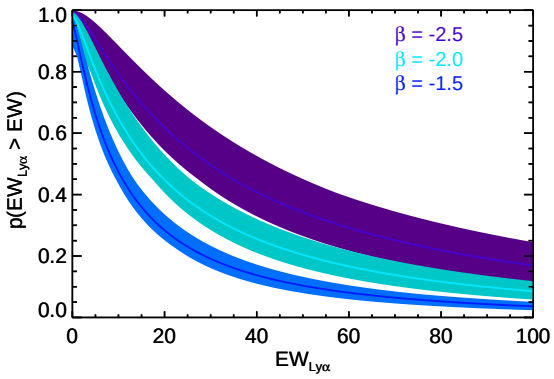

Figure 5.5 Inverse cumulative distribution functions of $\mathrm{EW_{Ly\alpha}}$ for our best fit model, plotted as a function of β. For a desired β, the Lyman alpha fraction, $\mathrm{x_{Ly\alpha}}$, for an arbitrary equivalent width is defined by the y-value of the curve at the given $\mathrm{EW_{Ly\alpha}}$.

plotted on a histogram of their $\mathrm{EW_{Ly\alpha}}$ detections and upper limits in Figure 5.4. The best fit parameters are $\mu = 2.7 \pm 0.7$, $\sigma = 1.4^{+0.9}_{-0.5}$, and $A_{em} = 1.0^{+0.0}_{-0.4}$. As we show in Appendix A, this formalism is the best fit to our post-reionization data.

5.4.2.2 A Generalized Approach

Now that we have determined the distribution which best fits the data at the key UV slope value of $\beta \sim -2.3$, we proceed with a more appropriate goal of determining the EW distribution across all values of β. Although faint galaxies at $z \geq 6$ may asymptote to $\beta \sim -2.3$, the UV-bright galaxies almost certainly do not (Bouwens et al. 2013). In order to fully leverage the $\mathrm{x_{Ly\alpha}}$ test for the more luminous objects, we must use a model that determines the EW distribution across a wide range of β.

To achieve this goal, we extend the Bayesian formalism introduced above. The differences are twofold. Firstly, we now include our entire sample of spectroscopically observed galaxies when fitting, rather than just those narrowly clustered around a particular value of β. Secondly, we must reconsider the nature of Equation 1 since it is clear that the EW distribution varies as a function of β from Figure 5.1.

It is most reasonable to consider that the *location parameter*, μ, varies with β since it is this parameter that governs the redistribution of EWs (see Figure 5.3). For convenience we assume that μ varies linearly with β, whence $\mu(\beta) = \mu_a + \mu_s \times (\beta + 2)$, where μ_a represents the location parameter at $\beta = -2.0$. Prior to selecting this model, we performed similar fits to a narrow range in β as in the above section, with different ranges in β, and found that while the best fit for μ varied strongly with the UV slope, both σ and A_{em} did not.

Figure 5.5 shows a representation of the product of the resulting formalism, while we detail the

full results in Appendix B. Because our model treats the *location parameter* as a linear function of β, we can generate an EW probability distribution function for any UV slope, although our sample only provides meaningful constraints in the observed range $-2.5 < \beta < -1.25$. In this figure, we plot 3 examples and their associated errors. Of course, a measured UV slope for a high redshift galaxy has some error uncertainty, and thus its own probability distribution, $p(\beta)$. To obtain $p(EW)$ given our model and an observation of β, we can marginalize over β for each galaxy in the sample:

$$p(EW_i) = \int p(EW|\beta)p(\beta_i)d\beta \tag{5.5}$$

5.4.3 UV Slope versus UV Luminosity

We now return to one of the assumptions motivating this paper. Does parametrizing the likelihood of Lyα emission via the UV slope represent a statistically better option than the combination of absolute UV magnitude and redshift used in previous high-redshift Lyα studies? Since we can measure β, $M_{\rm UV}$, $\rm EW_{Ly\alpha}$, and a photometric or spectroscopic redshift for 451 objects in our spectroscopic sample, we can directly address this question.

In the widely-used UV luminosity method, the dependence on $M_{\rm UV}$ is handled in a discrete manner, assigning galaxies into one of two bins, depending on whether they are greater or less than $M_{\rm UV} = -20.25$. $\rm x_{Ly\alpha}$ is also calculated in discrete bins at $z = 4, 5$, and 6. For the purposes of comparison, we use the Bayesian formalism developed in this paper to generalize this to a continuous model. To do so, we alter the definition of μ from $\mu(\beta) = \mu_a + \mu_s \times (\beta + 2.0)$ to $\mu(M_{\rm uv}, z) = \mu_a + \mu_{s,M_{\rm uv}} \times (M_{\rm uv} + 19.5) + \mu_{s,z} \times (z - 4.0)$. This thus replaces the linear dependence of the location parameter, μ, on UV slope, with a bivariate linear dependence on UV magnitude and redshift. We then use the same fitting process to determine the optimal values for all parameters in the model.

To compare how well each of these two models fits the available data, we use the Bayesian evidence ratio, or Bayes factor. The evidence is a measure of how likely the data are, given the model, and can be expressed as an integration of the likelihood function over all possible values for each parameter in the model

$$E = \int p(\theta|\mathbf{Obs})d\theta \tag{5.6}$$

Evaluating this for both models yields a significant gain via a ratio of $E_\beta / E_{M_{\rm uv},z} = 29$, showing convincing preference for the model based on β compared to the earlier method.

5.5 First Application to Data within the Reionization Era

Although the body of spectroscopic data targeting galaxies beyond $z \simeq 6$ in the reionization era remains sparse, it is growing rapidly, particularly through the advent of multi-slit near-infrared spectrographs such as MOSFIRE. Thus we are encouraged to apply our new method to such data. In addition to collating earlier relevant data available in the literature, we also present the first results from our new survey using MOSFIRE.

5.5.1 A New MOSFIRE Survey

As part of a long term survey targeting $z > 7$ galaxies using the MOSFIRE spectrograph on the Keck I telescope, we have secured deep spectroscopic observations in both November 2013 and March 2014 targeting two different fields. One represents distant sources in a deep HST blank field with accurate photometric redshifts and the other targeted gravitationally-lensed sources with extensive multi-band photometry.

Table 5.1. Summary of MOSFIRE survey for Lyα

Name	RA	Dec	J_{125}	z_{phot}	t_{exp} [hr]	5σ EW limit
A611-0193	8:01:00.32	36:04:24.3	26.0	7.9	2.6	12.9
MACS0647-1411	6:47:40.91	70:14:41.6	26.1	7.6	1.0	20.7
RXJ1347-0943	13:47:33.90	-11:45:09.4	26.4	7.5	1.0	27.7
CANDY-2272447364	3:32:27.24	-27:47:36.4	27.1	9.1	2.35	60
CANDY-2243349150	3:32:24.33	-27:49:15.0	27.2	8.5	2.35	57
GS-2098-8535	3:32:20.98	-27:48:53.5	27.2	9.7	2.35	64
GS-2533-8541	3:32:25.33	-27:48:54.1	26.4	7.6	2.35	30
GS-2779-5141	3:32:27.79	-27:45:14.1	27.2	9.6	2.35	64
GS-4402-7273	3:32:44.02	-27:47:27.3	26.9	7.4	2.35	50
UDF12-3313-6545	3:32:33.13	-27:46:54.5	28.5	7.4	2.35	200
UDF12-3722-8061	3:32:37.22	-27:48:06.1	27.8	7.7	2.35	110
UDF12-3846-7326	3:32:38.46	-27:47:32.6	29.0	7.0	2.35	330
UDF12-3880-7072	3:32:38.80	-27:47:07.2	26.9	7.5	2.35	220
UDF12-3939-7040	3:32:39.39	-27:47:04.0	28.6	7.7	2.35	180
UDF12-3762-6011	3:32:37.62	-27:46:01.1	28.4	8.1	2.35	150
UDF12-3813-5540	3:32:38.13	-27:45:54.0	28.2	8.2	2.35	70
UDF12-4256-7314	3:32:42.56	-27:47:31.4	27.3	7.1	2.35	50

Table 5.1—Continued

Name	RA	Dec	J_{125}	z_{phot}	t_{exp} [hr]	5σ EW limit
UDF12-4308-6277	3:32:43.08	-27:46:27.7	28.5	8.0	2.35	200
UDF12-4470-6443	3:32:44.70	-27:46:44.3	27.3	7.7	2.35	70

Note. — MOSFIRE survey targets. 5σ limiting sensitivities are calculated using the median limiting flux limit between skylines, and assuming a spectroscopic redshift of $z = 7.7$.

5.5.1.1 The GOODS-South / Ultra Deep Field

On the night of Nov 5, 2013, we secured a total of 3.5 hours exposure in the Hubble Ultra Deep Field region of GOODS-South. Observations were taken using 0.7" slits through intermittent high cirrus cloud and ~ 0.8" seeing. A total of 16 $z > 7$ candidates were included on this mask selected from an initial list of $z > 6.5$ targets from our UDF12 campaign and the GOODS-S field (Schenker et al. 2013b; McLure et al. 2013), augmented with two additional Y-drops outside the UDF proper from Oesch et al. (2012). We used the photometric redshift code, described in Section 5.4, to compute a redshift probability distribution for each object.

The UDF 2012 dataset (Koekemoer et al. 2013) (GO 12498, PI; Ellis) offers many distinct advantages for this first application of our method. Foremost, by virtue of the extraordinarily deep optical and F105W data available, contamination by foreground objects, as determined by the photometric scatter simulations in Schenker et al. (2013b) is $\sim 3\%$, down to the $J_{125} = 28.6$ limit of our targets. This contrasts with the $\geq 10\%$ contamination rate affecting galaxies in the CANDELS fields (Oesch et al. 2012). Secondly, as a result of a strategic deployment of near-infrared filters, our UDF 2012 candidates have better defined redshift probability distributions, allowing us to more confidently exclude the possibility of Lyα emission in the event of a non-detection. The median 68% confidence interval in photometric redshift for the UDF 2012 objects on our MOSFIRE mask is smaller by $\Delta z = 0.2$ compared to our GOODS-S targets (and most likely to earlier published blank field surveys — see §5.3).

The final target selection for this aspect of our survey was arranged to formally maximize the expected number of detected lines, and thus our leverage in calculating $\mathrm{x_{Ly\alpha}}$. As a first attempt, we used the $z \sim 6$ histograms of Stark et al. (2011) to predict the distribution of $\mathrm{EW_{Ly\alpha}}$for each object, as a function of its UV magnitude. The fractional number of expected detections was calculated for each object, taking into account the photometric redshift distribution (as our spectral coverage is incomplete), UV magnitude, and expected limiting flux for a likely MOSFIRE exposure. This exercise resulted in the final list of 16 candidates presented in Table 5.1.

5.5.1.2 CLASH Lensing Sample

Over the course of our November and March observations, we also targeted 3 candidates with a photometric redshift $z \geq 7.5$ from the CLASH HST survey (GO 12065-12791 PI; Postman) as collated in Bradley et al. (2013). Although these targets can only be surveyed individually, limiting our efficiency, as each is sampled with 8 HST filters at or longward of $\lambda = 7750$ Å , they have sharp redshift probability distributions and well-determined UV slopes, making them ideally suited for our new method.

We first targeted the $z \sim 7.9$ candidate in Abell 611 on November 5, 2013, securing 1.1 hours

of on-source integration in 0.8" seeing. A further 1.5 hours of integration was possible on March 5, 2014. In our March 2014 run, we also targeted candidates in RXJ-1347 and MACS-0647 for 1.0 hours each. Typical seeing conditions for the March nights were 0.60-0.65". For all data, we used a 2.5" AB dither pattern. Full details of the 3 targets are presented along with our GOODS-S/UDF 2012 sample in Table 5.1.

5.5.1.3 Data reduction

The data was reduced using the publicly available MOSFIRE data reduction pipeline[1]. This pipeline first creates a median, cosmic-ray subtracted flat field image for each mask. Wavelength solutions for each slit are fit interactively for the central pixel in each slit, then propagated outwards to the slit edges to derive a full wavelength grid for each slit. Background subtraction is handled as a two stage procedure. First, individual stacks of all A frames and all B frames, which are then used to produce A-B and B-A stacks. As the A and B frames are temporally interleaved, this provides a first level of subtraction. Secondly, a 2-D b-spline model is fit to the residuals in each of these stacks, in a method similar to that described by Kelson (2003). The two stacks are then shifted, rectified, and combined, producing a positive source signal flanked by two negative signals at approximately half strength, separated by the dither length.

Examination of our GOODS-S data revealed a gradual 0.6" ($\sim$ 3 pixel) drift in the spatial direction over the course of our integration, which needed to be corrected for. The drift was tracked using a $J_{125}\sim$ 19 star conveniently placed on one slit. The intensity of the star allowed us to follow the extinction for each frame, and after eliminating those frames affected by significant extinction or drift, we secured 2.35 hours of useful exposure. Due to this drift, the star on our original reduction displayed a somewhat greater FWHM of $\sim$ 1.2" than any of our individual exposures, which typically had a FWHM $\sim$ 0.8". To correct this, we registered the relative positions of all frames by fitting a Gaussian profile to star along the spatial axis. Given the drift over the entire exposure, we then arranged the frames into three separate groups, with the spatial positions in all frames consistent to within $\sim$ 1 pixel. Each of the three frame groups was reduced individually using the same procedure described above. To produce our final science stack, the three reductions were then shifted by the appropriate integer number of pixels and coadded, weighting by exposure time. Using this method, we were able to reduce the observed stellar FWHM to $\sim$ 1.0". Our final mask reaches a median 5σ limiting sensitivity between skylines of $\sim 7.0 \times 10^{-18}$ erg cm^{-2}s^{-1}. We note that approximately $\sim$ 33% of the Y-band spectral range is obscured by skylines at the MOSFIRE resolution of R $\sim$ 3380 given our 0.7" slit width.

[1] https://code.google.com/p/mosfire/

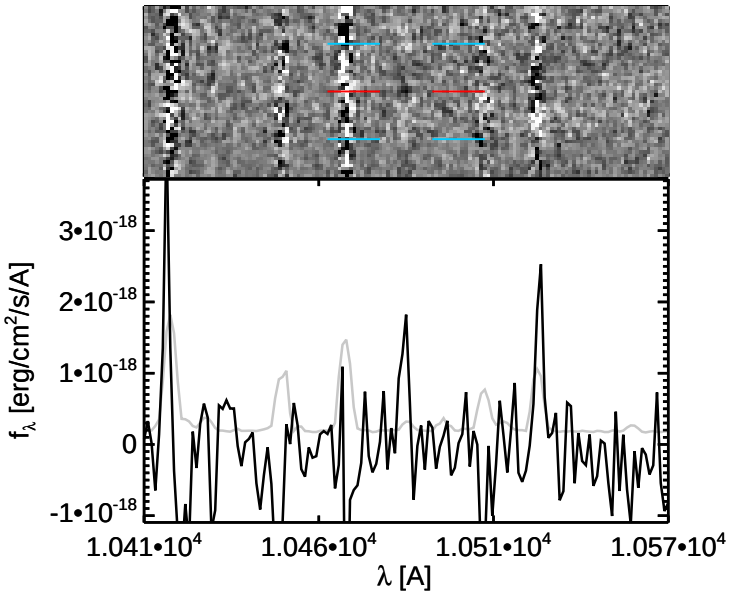

Figure 5.6 MOSFIRE observations of our lone target with visible line emission, UDF12 40242. The full two dimensional spectrum is shown at top, with the one dimensional spectrum plotted at the bottom, along with the error spectrum in grey. Given our A−B reduction strategy (described in Section 5.5.1.3), our 2D spectrum shows the expected positive signal (red line) flanked by two negative signals (blue lines), each separated by the amplitude of the dither pattern.

5.5.2 A New z=7.62 Lyman Alpha Emitting Galaxy

We inspected the reduced, two-dimensional spectra of all 16 objects by eye to search for Lyα emission. From this, we were able to locate only a single candidate emission line. Surprisingly, this emission line is located in one of our faintest targets, UDF12-3313-6545 (first identified by McLure et al. 2010, Bouwens et al. 2011), with a measured flux of 5.6×10^{-18} erg cm^{-2}s^{-1}. If the line is indeed Lyα, the galaxy lies at a spectroscopic redshift of $z = 7.62$, making it a promising candidate for the most distant spectroscopically-confirmed galaxy to date. We present the relevant details and HST cutouts of this galaxy in Figure 5.7.

Given the faintness (the emission line is detected at 4.0σ), line asymmetry, commonly used to distinguish Lyα, is not detectable. However, the fact that the line displays a clear positive signal flanked by two negative peaks indicates that the signal was present in both the A and B exposure positions. Although the line has a surprisingly large rest-frame equivalent width of 160 ± 40 Å, this is comparable to some discovered in $z \sim 6$ Lyα emitting galaxies (Ouchi et al. 2010). Notably, the spectroscopic redshift lies well within to the 1σ confidence interval of our derived photometric redshift distribution when line emission is accounted for, instilling further confidence in the redshift.

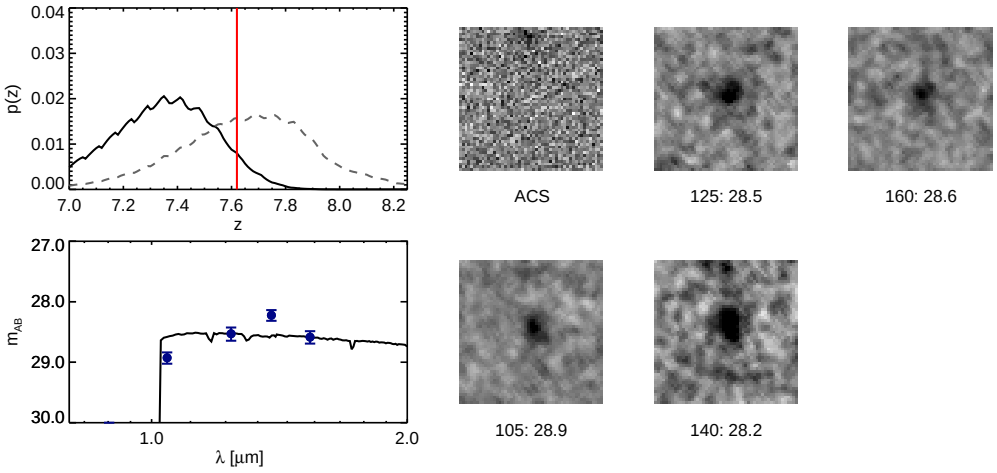

Figure 5.7 Right: 1.5 arcsecond diameter cutouts and total magnitudes (see data section) of our MOSFIRE target, UDF12 40242. As expected for a $z > 7$ candidate, the object is not formally detected in a stack of the optical data. Left, Top: Photometric redshift probability distribution function (pdf) for our target, with the actual spectroscopic redshift, $z = 7.62$, denoted in red. The solid black curve displays the pdf from the raw photometry, while the dashed grey curve shows the pdf after the observed MOSFIRE line flux has been subtracted from the Y_{105} data point. Left, Bottom: Best fitting SED for the galaxy, along with HST WFC3 Photometry.

5.5.3 Additional Data from Published Surveys

In order to achieve the most up-to-date and precise measurement of the Lyα opacity at $z \geq 6.5$, we have compiled a comprehensive sample of other near-infrared surveys for Lyα at high redshift, which we will utilize in our analysis. This includes our own prior work with Keck's NIRSPEC (Schenker et al. 2012), as well as a number of other surveys, using red-sensitive optical detectors on the VLT and Keck (Fontana et al. 2010; Pentericci et al. 2011; Ono et al. 2012; Pentericci et al. 2014), as well as independent work by Treu and collaborators using NIRSPEC (Treu et al. 2012) and MOSFIRE (Treu et al. 2013).

In total, this literature sample comprises 83 $z \geq 6.5$ galaxies for which follow-up spectroscopy at various depths has been attempted, plus an additional 19 from this work. To apply our method, we split this sample into two redshift bins centered at $z \sim 7$ and $z \sim 8$. The manner in which targets were assigned to each bin required careful consideration given the limited wavelength response of each instrument with respect to the photometric redshift likelihood distribution $P(z)$. Rather than binning on photometric redshift alone, we carefully considered the redshift range within which a null detection could be determined. If the median redshift for which a null detection could be determined was less than (greater than) $z = 7.5$, we place the object in the $z \sim 7(8)$ bin.

5.5.3.1 Monte Carlo simulation

To predict the number of detections expected in an IGM with no additional opacity to Lyα, we use a similar Monte Carlo method to that developed in Schenker et al. (2012). This simulation has three key inputs for each object: flux limits as a function of wavelength from the spectroscopic observations, which also take into account the night sky emission, a photometric redshift probability distribution, and a prediction for the IGM unprocessed $\mathrm{EW_{Ly\alpha}}$ (and thus $f_{Ly\alpha}$) distribution.

For objects observed in either this paper, or Schenker et al. (2012), flux limits as a function of wavelength were calculated directly from the reduced spectra by computing the variance in an aperture of 10 Å spectral extent. For the data in Treu et al. (2012) and Treu et al. (2013) we rescaled our flux limits from NIRSPEC and MOSFIRE, respectively, to match the quoted limits in the paper for each object. For Pentericci et al. (2011); Ono et al. (2012); Pentericci et al. (2014), we did the same with our LRIS limits, as presented in Schenker et al. (2012).

We used the published photometry from each paper (and our own here) in conjunction with our photometric redshift code described previously to determine a photometric redshift distribution for each object. The only exceptions are for the samples from Pentericci et al. (2011) and Ono et al. (2012), for which either photometry or coordinates were not available. For these objects, we used the photometric redshift distribution for ground-based z-drops from Ouchi et al. (2009).

Finally, for the objects in our new MOSFIRE survey, we generated the prediction for the IGM unprocessed $\mathrm{EW_{Ly\alpha}}$ distribution using the observed UV slope, as described in Section 5.4. Ideally, we would prefer to use this new method for all objects in the combined sample, in order to eliminate the potential bias of simply using M_{UV} as a predictor. However, with the exception of galaxies in the UDF 2012 field and CLASH lensed sample, the requisite 3 infrared photometric data points longward of the Lyman break essential for achieving an accurate measure of β are not available. Thus, for all other objects, we must predict $\mathrm{EW_{Ly\alpha}}$ as a function of M_{UV} from Treu et al. (2012), using the data presented in Stark et al. (2011). As an illustrative exercise, we also generated a prediction for the IGM unprocessed $\mathrm{EW_{Ly\alpha}}$ distribution of these objects using their M_{UV} to calculate a β derived from the M_{UV}-β relation at $z \sim 7$ from Bouwens et al. (2013). Though not plotted, these results are available in Table 5.2.

With these inputs, we conduct a Monte Carlo simulation. In each trial for a given object, we draw a redshift from the photometric redshift distribution, and a Lyα equivalent width from the $\mathrm{EW_{Ly\alpha}}$ distribution. From the observed photometry, this $\mathrm{EW_{Ly\alpha}}$ is converted to a flux. We then sample the spectroscopic flux limit at the redshift drawn to determine if the emission line would be observed at $\geq 5\sigma$. This process is then repeated with $N = 10000$ trials for each object.

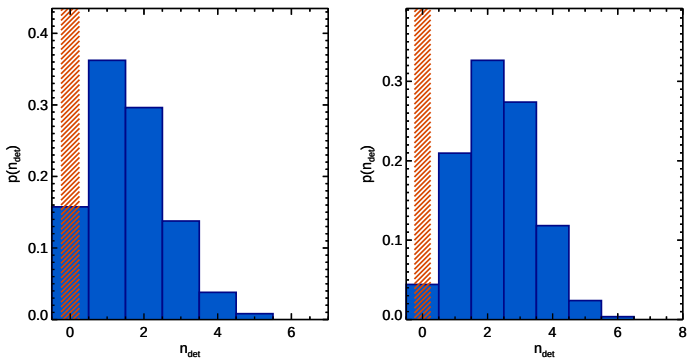

Figure 5.8 Left: Predicted number of detections for our MOSFIRE survey using the $EW_{Ly\alpha}$ probability distribution from Treu et al. (2012), which uses M_{UV} as the predictor. The observed number of 0 detections is indicated by the red crosshatch. Right: Predicted number of detections for same survey, but using β as the predictor for $EW_{Ly\alpha}$, as outlined in Section 5.4. In this case, the average number of expected detections is increased by a factor of 1.4, highlighting the importance of using a model that accurately predicts the IGM unprocessed equivalent width distribution. The equivalent upper limit on the transmission fraction is also decreased by a factor of 1.23.

5.5.3.2 Comparison between UV slope and UV luminosity predictions

Before considering the total sample (i.e., including previous data from the literature), we compare the difference in the expected Lyα statistics for the high redshift sample using either M_{UV} or β as the basis for predicting the IGM unprocessed $EW_{Ly\alpha}$ distribution. Since only the UDF 2012 and CLASH surveys currently have accurate individual measurements of β, this comparison can only be done for the 13 targets from our recent MOSFIRE survey.

The number of expected detections is compared in Figure 5.8. Although hampered by limited statistics, the difference is still significant. Using β as a basis, we predict an average of 1.4 more detections than using M_{UV}. This difference represents an important correction of a systematic error in the prior $x_{Ly\alpha}$ tests. Our new results show that the M_{UV} method, for this specific sample of 13 targets, significantly underpredicts the incidence of IGM unprocessed Lyα emission, which results in an overestimate of the IGM transmission. The difference in predicted detections is dependent upon the properties of the sample considered but, as the objects probed from the both the UDF and CLASH are intrinsically faint, with blue UV slopes it is not surprising that the difference is so great.

This change in predicted Lyα emission has important consequences for the transmission fraction of the IGM implying a lower limit on the neutral fraction that is a factor 1.16 larger. Clearly, for a given survey, our new β method for predicting the IGM unprocessed $EW_{Ly\alpha}$ distribution has significant advantages, and reduces a key systematic error. This will be especially relevant for spectroscopic follow-up of the HST Frontier Fields (GO:13496, PI: Lotz), and their parallels, given

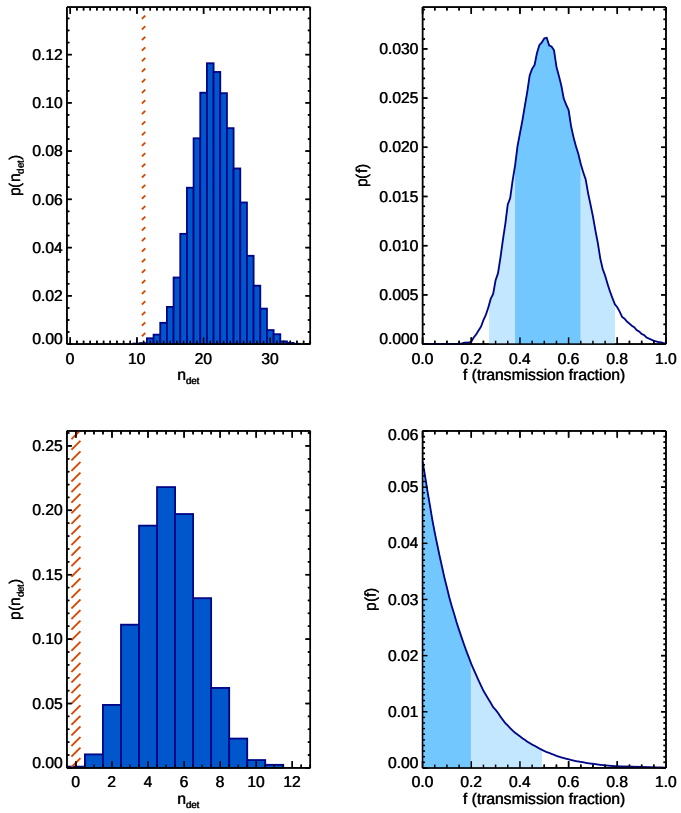

Figure 5.9 Results from our new MOSFIRE campaign, combined with data from the literature. Top left: Histogram of expected 5σ detections of Lyα, computed using the Monte Carlo method described in the text for our $z \sim 7$ sample. The red crosshatches denote the combined number of detections observed in all surveys. Top right: Given our predicted and observed number of detections, the constraints on the average extinction fraction of Lyα, assuming a patchy opacity. Dark blue and light blue shading encompass the 1σ and 2σ confidence intervals, respectively. Bottom left and right: Same as above, but for our $z \sim 8$ sample.

these fields will have full coverage with the same four WFC3/IR filters used for the UDF.

5.5.3.3 Analysing the entire sample

We can now combine the various data, including both our own MOSFIRE survey and various literature sources. The net result is a histogram of the number of 5σ detections overall. These histograms are displayed, both for the $z \sim 7$ and $z \sim 8$ samples in Figure 5.9; our new MOSFIRE survey is, by design, more effective in constraining the higher redshift limits. We see evidence for a moderate decline in the Lyman alpha fraction at $z \sim 7$ and a continued sharper decline at higher redshift. Note that our new spectroscopic confirmation at $z = 7.62$ is not included as a detection as it lies below the a priori 5σ flux limit.

As an illustration, we can convert these observational-based results to an IGM extinction of Lyα

Table 5.2. $x_{\mathrm{Ly}\alpha}$ target compilation and results

Survey	Observed	5σ Detections	Transmission fraction (f)	x_{HI}
This work MOSFIRE M_{UV}	19	0	< 0.47	> 0.43
This work MOSFIRE β	19	0	< 0.36	> 0.50
Composite $z \sim 7$	72	11	$0.51^{+0.14}_{-0.11}$	$0.40^{+0.08}_{-0.10}$
Composite $z \sim 8$	27	0	< 0.19	> 0.65
Composite $z \sim 7$[a]	72	11	$0.34^{+0.13}_{-0.06}$	$0.51^{+0.05}_{-0.09}$
Composite $z \sim 8$[a]	27	0	< 0.15	> 0.68

[a]For these results, where individual UV slopes are not available, we instead use individual values of M_{UV} to predict a value of β, which in turn is used to generate the IGM unprocessed $\mathrm{EW}_{\mathrm{Ly}\alpha}$ distribution.

Note. — Monte Carlo results for transmission fraction, f, and x_{HI}.

by adopting the model used in Schenker et al. (2012) appropriate for patchy reionization. In this model, the IGM is partially opaque, such that Lyα escapes to the observer unattenuated from a fraction, f, of galaxies, while it is completely extinguished by the IGM in a fraction $1 - f$. Given the histogram of expected detections and the number actually observed, we infer a probability distribution for this transmission fraction, f. At $z \sim 7$, we find $f = 0.6 \pm 0.15$, and at $z \sim 8$, a 1σ upper limit of $f < 0.19$. The full results can be found in Table 5.2 and are plotted along with the lower redshift data on $x_{\mathrm{Ly}\alpha}$ in Figure 5.10.

Discussing the uncertainties in the transformation from transmission fraction to x_{HI} is beyond the scope of the present paper. However, clearly this conversion is dependent upon a number of physical parameters, some internal to the galaxy, and others from the IGM state itself. These include the velocity offset of Lyα from the galaxy's systemic velocity (e.g., Hashimoto et al. 2013; Schenker et al. 2013a), the ionizing photon escape fraction (Dijkstra et al. 2014), as well as the possible presence of optically thick absorption systems (Bolton & Haehnelt 2013). Until the theoretical models converge, and/or observations of these key quantities are available, absolute measures of the neutral fraction will still be subject to systematic errors. Nonetheless, we have demonstrated substantial observational progress with our new survey and improved methodology, reducing one of the key systematic errors. Using the models of McQuinn et al. (2007) here to provide an estimate of x_{HI}, we find $x_{HI} = 0.34^{+0.09}_{-0.12}$ at $z \sim 7$, and $x_{HI} > 0.65$ at $z \sim 8$.

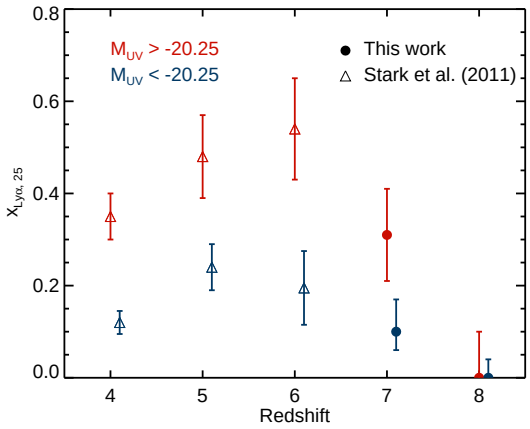

Figure 5.10 The fraction of Lyman break galaxies that display Lyα in emission at an EW $\geq$ 25 Å, plotted as a function of redshift. The values at $z = 7$ and 8 reflect differential measurements with the data at $z = 6$, as described in the text. Thus, these data points and errors are simply the convolution of the $x_{Ly\alpha}$ PDF at $z = 6$ and the transmission fraction PDF at $z = 7$ and 8.

5.6 Spectroscopy with the CIII] 1907/1909 doublet

The absence of the Lyα emission line at $z \geq 7$, while of great interest for its implications regarding reionization, presents a problem. At redshifts $z \leq 6$, this line has proved the most valuable tool for confirming color selected Lyman break galaxies via direct spectroscopy. In the rest UV, no other emission line has proved to be nearly as bright, and the common asymmetric line profile with a sharp blue cutoff and extended red tail helps to provide an unambiguous identification. This becomes especially important at $z \geq 3.8$, above which all of the typical strong rest-optical nebular lines (Hα, Hβ, and [OIII]) are no longer available through ground-based spectroscopy due to the atmospheric opacity longward of 2.4 μm. For galaxies fainter than $m_{AB} \sim 24.5$, where continuum spectroscopy is out of reach even for 10 meter class telescopes, this line currently provides the most useful redshift indicator.

The lack of any visible lines besides Lyα also prevents us from measuring the velocity offset of Lyα from a galaxy's systemic velocity, critical for accurate measurements of x_{HI}. Although we have already presented work in Chapter 4 which measures this quantity for $z \leq 3.8$ galaxies with strong Lyα in emission and reduces a key systematic uncertainty in the $x_{Ly\alpha}$ test, we would ideally like to measure this quantity much closer to the epoch of reionization in order to most accurately reduce any systematic uncertainty.

Spectroscopy of the CIII] 1907/1909 doublet provides an interesting option to overcome the above issues. These two closely spaced lines consist of a forbidden magnetic quadrupole transition at $\lambda = 1906.68$ Å and a semi-forbidden electric dipole transition at $\lambda = 1908.73$ Å[2] . Previously, these

[2]From herein, when referring to the combined observation of both lines, we simply use CIII]

lines have not received much attention because in well-studied, normal $z \sim 2-3$ star-forming galaxies, they appears quite weak; Shapley et al. (2003) measure a combined rest-frame EW of only 1.6 ± 0.6 Å in a composite $z \sim 3$ spectrum. As UV spectroscopy in the local universe must be completed from space, measurements of this line are still sparse, however, the catalog compiled in Leitherer et al. (2011) demonstrates that this line can have significant equivalent widths at metallicities at $12 + \log(O/H) \lesssim 8.1$. There also exists additional evidence that this line strength increases in low mass, high-redshift galaxies from studies of lensed $z \sim 2-3$ arcs, three of which find a CIII] equivalent width of ~ 10 Å (Fosbury et al. 2003; Erb et al. 2010; Bayliss et al. 2013).

However, the most comprehensive study of the potential of the CIII] doublet for studies in the reionization era, and which provides the impetus for the current discussion, is that of Stark et al. (2014, in prep.). This work conducted a spectroscopic study of lensed, low-mass, star-forming galaxies at $0.9 < z < 2.5$ discovered in SDSS by targeting wide-separation galaxy-lens candidates (Stark et al. 2013b). Many of these galaxies have the similar physical properties to the population at high-redshift: low stellar masses, blue UV slopes, and large observed Lyα equivalent widths. Most important, however, is the unambiguous positive correlation uncovered betweeen the equivalent widths of Lyα and CIII]. As we know from earlier in this thesis and Stark et al. (2010, 2011), the ubiquity of large Lyα equivalent widths at high redshift indicates that CIII] may provide a promising alternative probe, especially at $z \sim 7$, where the intergalactic medium severely attenuates any emission from Lyα.

The CIII] doublet is well-placed to explore our current redshift frontiers, given that it is visible in the H-band at redshifts $6.6 < z < 8.5$, and again in the K-band at $z > 9.1$. Given the measured equivalent widths in low mass, $z \sim 2-3$ galaxies, with current instrumentation, these lines should be visible in galaxies down to $m_{AB} \sim 26$. More importantly, the NIRSPEC instrument on JWST will push these detection limits down by another order of magnitude, providing an even greater impetus to understand the characteristics of this doublet at high redshift prior to the telescope's 2018 launch.

To both test the viability of CIII] as an alternative redshift indicator, and to attempt to acquire a measurement of the Lyα velocity offset in the midst of the epoch of reionization, we chose to follow-up a $z > 7$ LBG previously confirmed with Lyα. After considering both the flux limits achievable with MOSFIRE and the skyline location in the likely region of CIII], we made a decision to observe the $z = 7.213$ Lyman break galaxy, GN-108036, first discovered in Ono et al. (2012) with H_{160}= 25.8.

5.6.1 Data

We secured spectroscopic observations of GN-108036 with MOSFIRE on the Keck I telescope on the nights of March 6 and April 11, 2014. During our March run, we compiled a total of 3.1 hours of

exposure in the H band with a 0.8 arcsecond slit. Conditions were generally clear, but with slight cloud during the first half of the observations. The median FWHM of a reference star included on the mask was 0.6 arcseconds. On our April night, we secured an additional 1.1 hours, with a median seeing FWHM of 0.5 arcseconds and clear conditions.

The data was reduced using the offical MOSFIRE data reduction pipeline (DRP) and a procedure similar to that described in Section 5.5.1.3. However, in order to better account for the variation in conditions during our March run, we split the data into three segments of ~ 1 hour each, which were then run through the DRP separately. To produce a final science stack, the resulting three images plus the single reduced image from our April data were then stacked using inverse-variance weighting. The final stack has a 5σ flux limit of 1.8×10^{-18} erg cm^{-2}s^{-1}, consistent with the expectation produced from the MOSFIRE exposure time calculator.

5.6.2 Results

Our spectrum in the vicinity of CIII] is displayed in Figure 5.11. We find a tentative detection of an emission line with a formal significance of 4.8σ in an aperture of 1.1 arcseconds in the spatial direction and 13 Å in the spectral direction. The centroid is consistent with the expected position of our high-redshift target along the slit to within 3 pixels, or 0.55 arcseconds, and is located in a region free from skyline contamination.

As any detection of an emission line other than Lyα at $z > 7$ would represent a significant advance, it is important to verify the reality of our detection. We first do this by measuring the fluxes at the expected positions of the two negative images flanking the line detection. As our final stack is the sum of an A-B image and a shifted B-A image, for a real line we expect two negative images, each of approximately half the total flux, offset above and below the positive image by the dither length of 2.5 arcseconds. Reassuringly, this is the case; we measure significances of -1.8σ above the line, and -3.0σ below. If the entirety of the negative signal appeared in one location, this could indicate that the line originates either solely from either the A or B exposures, and may be an artifact.

We also further evaluate the line significance in the four separate subsets of the data discussed earlier, each with an exposure time of ~ 1 hr. The four two-dimensional spectra are displayed in Figure 5.12. This figure demonstrates that the composite stack is not dominated by a single epoch, indicating that our detection is not due to a rogue cosmic ray or artifact. Additionally, even in each subset, we measure a positive signal to noise ratio in the same aperture used to measure the composite line flux.

As mentioned previously, the CIII] line observed at ~ 1908 Å is a blend of two components at $\lambda = 1906.68$ and and 1908.73. In $z \sim 2$ sample of Stark et al. (2014, in prep) this line appears blended, but at $z = 7.213$ the observed separation between the two components is ~ 17 Å, which is

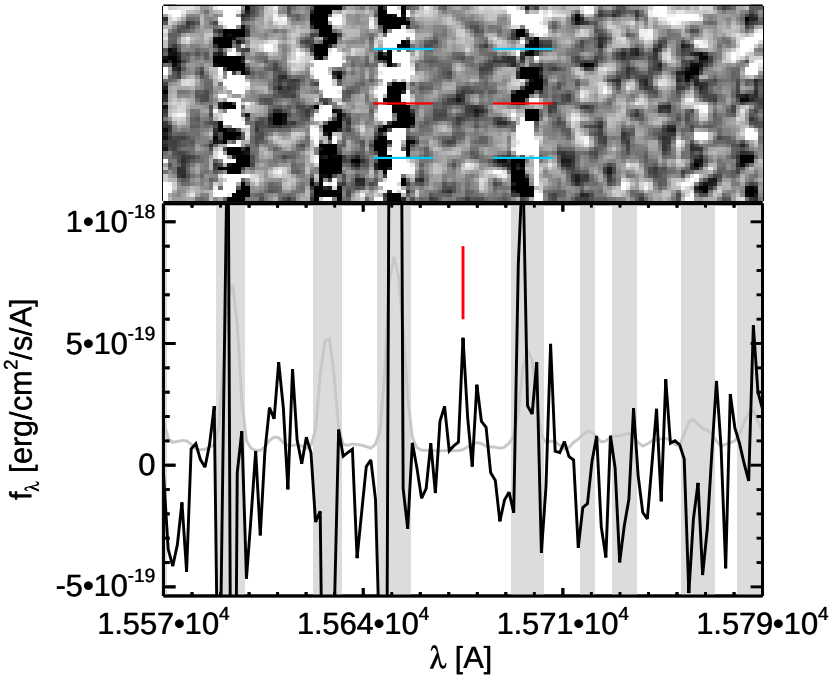

Figure 5.11 One and two dimensional extractions of our tentative detection of CIII]. Formally, the line has a detection significance of 4.8σ, giving it a flux of 1.6×10^{-18} erg cm^{-2}s^{-1}. The red line denotes the location of the emission line, while the blue lines denote expected positions of the flanking negative signals as a result of the A-B dither pattern and subtraction.

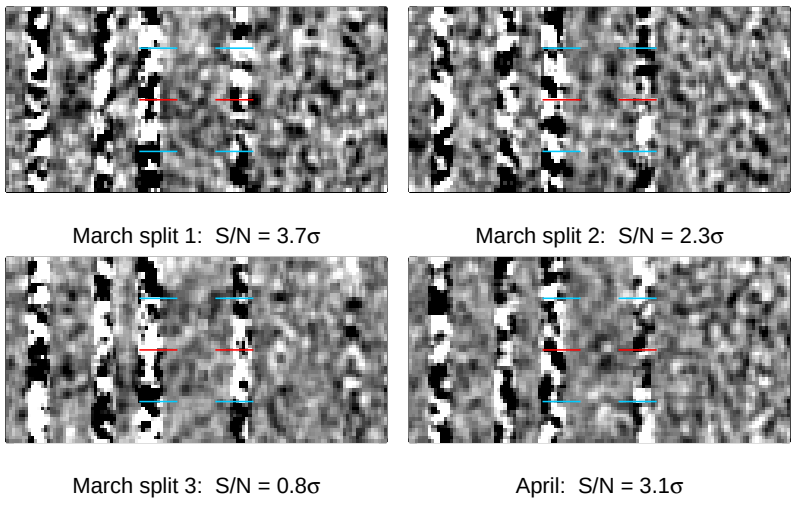

Figure 5.12 Cutouts of our spectrum of GN-108036 in the vicinity of CIII] broken down by epoch. The formal signal to noise at the position of the line is listed below each image.

well-resolved by MOSFIRE. Although our detection is marginal, we see no evidence for the presence of a second component, so we must consider the ramifications if our line detection is either [CIII]λ1907 or CIII]λ1909, and whether the other component should be visible given the skyline proximity.

With our observed centroid at $\lambda = 15679.1 \pm 0.5$ Å, the leading edges of the nearest skylines are located ~ 17 Å distant toward the blue end of the spectrum and ~ 19 Å toward the red end. Thus, the lack of visibility of a second line should not be a major cause for concern, as we would expect $\sim 1/2$ the flux of the component to be obscured, since even on the skyline edges our signal to noise ratio drops by a factor of ~ 3.

In regions with low electron densities $n_e < 10^3$ cm^{-3}, the two lines have a constant flux ratio of $I_{1907}/I_{1909} = 1.53$, while as the density increases, this ratio will gradually drop. Even at $n_e = 10^4$ cm^{-3}, the flux ratio has only dropped to ~ 1.2, so given the electron densities of $\lesssim 10^3$ observed in $z \sim 2$ galaxies (Lehnert et al. 2009), a ratio of ~ 1.5 is likely.

However, we also have the observed velocity offset from Lyα to guide our analysis. If our observed line is the semi-forbidden CIII]λ1909 component, the velocity offset for Lyα would be -50 ± 75 km s^{-1}, while if it represents the forbidden [CIII]λ1907 component, the offset would be -370 ± 75 km s^{-1}. From the work of Steidel et al. (2010) and our own results in Chapter 4, we have seen that Lyα is invariably redshifted with respect to the systemic velocity as traced by nebular lines such as CIII]. A blueshift of nearly 400 km s^{-1} would require a contrived scenario, such as Lyα scattering off an inflowing cloud of neutral gas on the far side of the galaxy. As such, we consider the most likely scenario to be that we have measured the CIII]λ1909 line. However, whichever case is true, the measured Lyα velocity offset is smaller than the $\langle v_{Ly\alpha} \rangle = +149$ km s^{-1} measured in Chapter 4, providing, for the first time, a measurement of this quantity within the epoch of reionization.

Finally, we place this measurement into the context of the derived relationship between the Lyα and CIII] equivalent width from Stark et al. (2014, in prep.). Solely considering the measured line flux and neglecting any flux from a potential obscured emission line, we derive a rest-frame equivalent width of 9 ± 2 Å. Given the best estimate for the Lyα EW as 50 Å (Ono, private communication), this places the object slightly above the relation, which we display in Figure 5.13. However, including the expected contribution of [CIII] 1907 would increase the EW to ~ 22 Å, given the flux ratio for reasonable electron densities. This is close to, but still less than the maximum thusfar observed in the local universe at EW$_{CIII]} = 27$ Å (Leitherer et al. 2011), and could possibly be a sign of an extreme ionizing spectrum. In either case, our measured [CIII]λ1907 + CIII]λ1909 equivalent width provides a first demonstration of the potential of these lines as method for spectroscopically confirming Lyman break galaxies in an era where Lyα emission is significantly quenched.

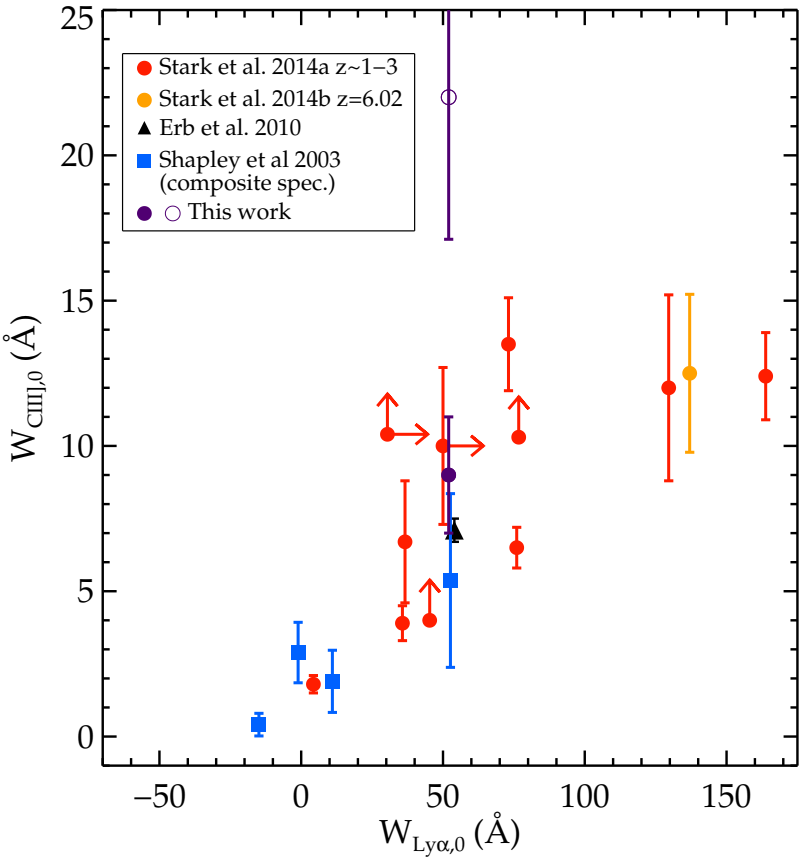

Figure 5.13 Adopted from Stark et al. (2014, in prep.). Observed correlation between Lyα and CIII] equivalent widths. We add to this plot our CIII] equivalent width, both solely accounting for the observed line flux (solid purple), and assuming that the [CIII]λ1907 line is fully obscured by a skyline at the typical flux ratio of 1.5 (outlined purple).

5.7 Conclusions

Using our sample of 451 $3 < z < 6$ spectroscopically followed-up Lyman break galaxies, we demonstrate an improved correlation between the ultraviolet continuum slope of a galaxy, β, and its Lyα emission strength. Given the availability of deep WFC3 photometry for both the GOODS-N and S fields, this progress follows measurements for many individual galaxies in this redshift range, rather than via stacked or averaged UV slopes, as in earlier work (Shapley et al. 2003; Stark et al. 2010).

We demonstrate that this correlation with the presence of Lyα is stronger and more physically-motivated than that based on the UV luminosity and thus provides a natural basis for an improved model for the Lyα fraction test, now widely used to measure the evolving neutrality of the $z > 6.5$ IGM. We demonstrate the benefits of this new model using a new MOSFIRE spectroscopic survey of $7 < z < 8$ targets from the Ultra Deep Field 2012 catalog and CLASH lensing survey, and combine this with data at these redshifts already published in the literature. As a result, we present the implications of the most comprehensive search for Lyα emission at $z \simeq 8$ to date, confirming once again important evidence that cosmic reionization ended at redshifts $z \simeq 6.5$.

As a byproduct we also present the 4.0σ confirmation of Lyα in a galaxy at $z = 7.62$, likely the most distant spectroscopically-confirmed galaxy. Finally, we demonstrate the utility of two new near-UV emission lines, [CIII]λ1907 and CIII]λ1909, in providing an alternative method of spectroscopic confirmation in the heart of the reionization era by recording a tentative detection in a $z = 7.213$ galaxy.

5.8 Appendix

5.8.1 A. Models for p(EW—β)

The maximum likelihoods inferred from each of the four distributions are noted in Table 5.3. These results demonstrate that the lognormal distribution provides the best fit to the available data — its likelihood surpasses that of any other model by two orders of magnitude. Thus, we use this distribution as the basis for the more general form of $p(EW|\beta)$ we consider next.

Table 5.3. Lyα functional forms

Distribution name	Equation	Free parameters	Reference	Log_{10} max likelihood
Lognormal	$A_{em}\frac{1}{\sqrt{2\pi}\sigma \mathrm{EW}}exp(-(\ln(\mathrm{EW})-\mu)^2/2\sigma^2)$	A_{em}, μ, σ	This work	-75.4
Half-Gaussian	$\frac{1}{\sqrt{2\pi}\sigma}exp(-(\mathrm{EW}-\mu)^2/2\sigma^2)$	A_{em}, σ	Treu et al. (2012)	-80.7
' w/ high-EW tail	$A_{em,g}\frac{1}{\sqrt{2\pi}\sigma}exp(-(\mathrm{EW}-\mu)^2/2\sigma^2)+A_{em,c}$	$A_{em,g}$, $A_{em,c}$, μ, σ	Pentericci et al. (2011)	- 80.8
Declining exponential	$A_{em}exp(-EW/EW_0)$	A_{em}, EW_0	Dijkstra et al. (2011)	-77.9

Note. — List of the mathematical distributions used to fit the $\mathrm{EW}_{\mathrm{Ly}\alpha}$distribution at $\beta \sim -2.3$, and the calculated maximum likelihoods. Having a maximum likelihood two orders of magnitude greater than any other distribution considered demonstrates the lognormal distribution provides the best fit.

5.8.2 B. Results of full modeling procedure

For reference, and such that they are available for use in future work, we list here the final values for our generalized lognormal fit to the $\mathrm{EW}_{\mathrm{Ly}\alpha}$ distribution at $3 < z < 6$. They are $\mu_a = 3.0^{+0.125}_{-0.25}$, $\mu_s = -1.125 \pm 0.25$, $\sigma = 1.3 \pm 0.1$, and $A_{em} = 1.0^{+0.0}_{-0.05}$. We also provide a plot of the posterior probability distribution below so the reader is able to appreciate the sometimes non-negligible covariances between parameters.

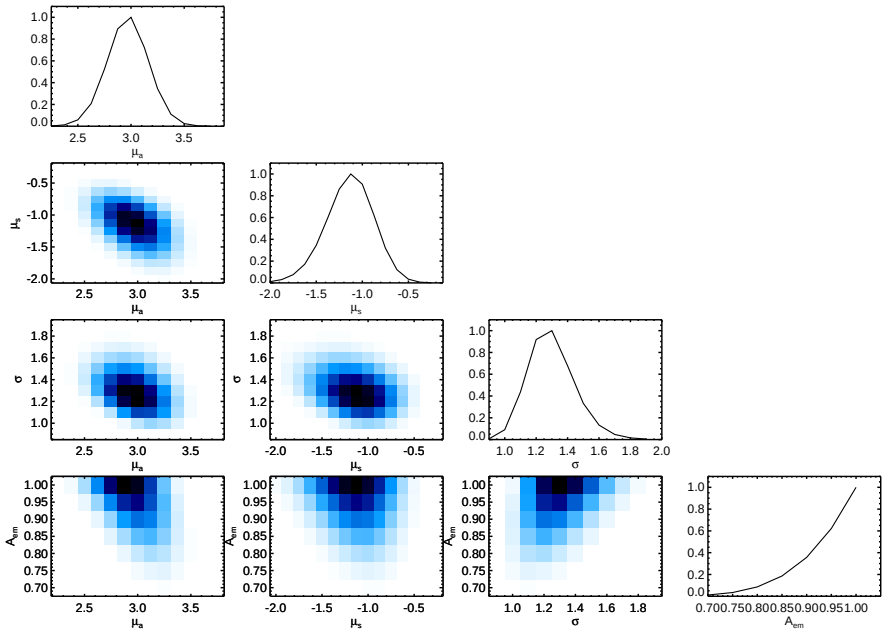

Figure 5.14 Posterior probability distribution for our full model, $p(\mathrm{EW}_{\mathrm{Ly}\alpha}|\beta)$. Shaded plots represent the posterior PDF marginalized over all but the two variables labeling the axes, while line plots are marginalized over all but one variable. Thus, the one dimensional PDFs for each variable, from which we quote our error bars, can be read off along the diagonal.

Chapter 6

Synthesis and future prospects

The work presented in this thesis represents a major step forward, both in our understanding of the cosmic reionization history, and the early star-forming galaxies that drove this process. However, there remains much still to uncover about this formative era. In this chapter, I will both summarize the progress made in this work, as well as highlight the ongoing and future research directions that will address some of the open questions that still remain.

6.1 Charting cosmic reionization

A full understanding of cosmic reionization and the events that drove it requires a detailed measurement of the neutral fraction as a function of redshift, $x_{HI}(z)$. Although there are a number of complementary techniques that have thusfar been used to probe the ionization state of the early IGM, most have significant difficulties in providing such a measurement.

Quasar absorption spectroscopy has provided evidence of complete Gunn-Peterson absorption troughs, but lacks sensitivity to even moderate neutral fractions of $x_{HI} > 10^{-3}$ (Fan et al. 2006). More recently, the Lyα damping wing shape of the $z \sim 7$ quasar discovered by Mortlock et al. (2011) has been modeled to imply $x_{HI} \simeq 0.1$ (Bolton et al. 2011), but quasars at $z \geq 7$ have proven so elusive that more have yet to be found.

WMAP measurements of the cosmic microwave background polarization and temperature power spectrum have provided a measurement of the Thomson optical depth to the surface of last scattering, with the most recent being $\tau_e = 0.089 \pm 0.014$ (Hinshaw et al. 2013). However, much greater effort will be required to place any constraints on the evolution of reionization using CMB data. Such a measurement from may be possible from either the structure of the reionization-induced large scale power spectrum bump (e.g., Holder et al. 2003), or the small scale temperature power spectrum (McQuinn et al. 2005). Currently, there only exists an upper limit on the duration of the patchy phase of reionization using temperature measurements from the South Pole Telescope of $\Delta z < 7.2$ (Zahn et al. 2012). Kaplinghat et al. (2003) estimate that to produce a full $X_{HI}(z)$ curve would

require an instrument with 25× the sensitivity of Planck, pushing such possible results far into the future.

Studies of Lyman alpha emitting galaxies (LAEs) have also begun to provide meaningful constraints on the neutral fraction during reionization. By comparing the observed LAE luminosity function at $z = 6.5$ to the $z = 5.7$ LAE LF, when the universe was known to be fully ionized, both Ouchi et al. (2010) and Kashikawa et al. (2011) have detected a significant decline (30% and 24%, respectively) in total abundance, but only place an upper limit on the neutral fraction of $x_{HI} < 0.2 \pm 0.2$. More recently, Konno et al. (2014) detect a steep drop in the $z = 7.3$ LF, ruling out a no-evolution scenario at $> 90\%$, and implying a neutral fraction of $x_{HI} = 0.3 - 0.8$. However, these measurements remain degenerate with an intrinsic decline in the population of Lyman alpha emitters themselves such as expected from the star-formation history.

In this thesis, I have both presented and significantly refined a technique to measure the neutrality of the intergalactic medium that has not only provided some of the first constraints on the neutral fraction in the heart of reionization, but has been taken up by numerous other groups (e.g., Treu et al. 2012; Caruana et al. 2012; Bunker et al. 2013; Schmidt et al. 2014). The initial application of the method is detailed in Chapter 2. This test uses color-selected star-forming galaxies in the reionization epoch, which are then observed with intermediate resolution spectroscopy to search for Lyα in emission. Stark et al. (2010) and Stark et al. (2011) laid the groundwork for this test by performing extensive rest-UV spectroscopy of LBGs at $4 < z < 6$. Dividing the sample into UV-bright ($M_{\rm UV} < -20.25$) and UV-dim bins as a function of redshift showed that all galaxies displayed an increase in Lyα emission strength with redshift, with 54% of the dim galaxies displaying $\rm EW_{Ly\alpha} > 25$Å at $z \sim 6$. As quasar absorption studies have shown the universe to be uniformly highly ionized ($x_{HI} < 10^{-3}$) at this redshift (Fan et al. 2006), this value of the Lyman alpha fraction, $\rm x_{Ly\alpha}$, is then taken as the baseline value, intrinsic to galaxies at higher redshift.

In Chapter 2, we detail one of the first efforts to use this relationship to measure the neutrality of the high-redshift IGM. In total, we surveyed 19 galaxies spectroscopically: 8 with LRIS on Keck I (sensitive to $z < 7.2$), and an additional 11 with NIRSPEC on Keck II, sensitive to $6.8 < z < 8.2$ and $8.0 < z < 9.6$ for the higher redshift targets. Despite the large number of targets surveyed, we were only able to secure two detections of Lyα at a significance $\geq 5\sigma$, indicating a large decrease in the incedence of emission from what was expected given the $z \sim 6$ predictions. To assess the significance of this drop, we used a Monte Carlo simulation for which only $< 1\%$ of the realizations resulted in so few detection. Though we considered other possibilities, we found the most likely explanation for such a steep drop in emission is an increase in IGM neutrality. While an increase in dust could cause such an effect, this conflicts with the measurement of blue UV slopes found at $z \sim 7$ (e.g., Dunlop et al. 2012; Bouwens et al. 2012a). To fully account for the drop in observed Lyα emission, the contamination fraction from lower redshift sources would need to be $\simeq 50\%$ at $z \geq 7$, while

estimates from simulations put this at a much more modest value of $\leq 10\%$ (e.g., Bouwens et al. 2011; Schenker et al. 2013b). An increase in HI in the surrounding CGM of the galaxy could also serve to extinguish this emission, but low ionization absorption lines, which should trace similar gas, in the composite spectra of Jones et al. (2012) actually decrease in strength with redshift. Finally, a significant increase in the escape fraction of ionizing photons could also quench Lyα emission, but recently both Finkelstein et al. (2013) and Smit et al. (2014) have shown evidence for strong [OIII] nebular line emission at $z \gtrsim 6.8$, providing evidence against this scenario. Having reason to rule out all these alternative possibilities leaves an increase in x_{HI} as the preferred scenario.

6.1.1 Systematic errors in the $\mathbf{x_{Ly\alpha}}$ test

Although the Lyman alpha fraction test has seen substantial progress over the last few years, it is not without its drawbacks. Here, I will delineate the systematic errors present in this test and, where applicable, the work I have done as part of my thesis to help take these into account.

6.1.1.1 Intrinsic Lyα distribution at $z \geq 7$

This specific uncertainty can be divided into two related components, both of which have been addressed through the work in this thesis. Firstly, prior to the work detailed in Chapter 5, there existed no thorough analysis concerning the shape of the lower redshift $\mathrm{EW_{Ly\alpha}}$ distribution function, critical to deriving an unbiased measurement of the extinction of Lyα from neutral hydrogen. In fact, previous works used no less than than four different models for the $\mathrm{EW_{Ly\alpha}}$ distribution function (e.g., Dijkstra et al. 2011; Pentericci et al. 2011; Schenker et al. 2012; Treu et al. 2012). Although these could each provide adequate fits to the data, no investigation had been undertaken to compare the goodness-of-fit between these. Secondly, by assuming that the predicted $\mathrm{EW_{Ly\alpha}}$ distribution, binned by absolute UV magnitude, did not evolve from $z = 6$ to $z > 6$, another systematic error is introduced. Since Stark et al. (2011) demonstrated that this quantity evolves significantly from $4 < z < 6$, we can reasonably expect similar evolution at $z > 6$.

In Chapter 5, we described how to reduce both these sources of error. We first reparameterized the $\mathrm{EW_{Ly\alpha}}$ distribution as a function of the UV slope, β, rather than one of UV magnitude and redshift. This has the considerable advantages that the UV slope is a directly observable quantity for $z > 6$ galaxies, and given that it represents a combination of the stellar population and dust content, is physically related to the emission of Lyα. Thus, when determining the intrinsic $\mathrm{EW_{Ly\alpha}}$ distribution of a $z > 6$ sample in a given survey, the need for extrapolation is eliminated, as this distribution is simply determined given the observed UV slopes and an application of our calibrated model. Of course, it is possible that the UV slope is not a completely reliable predictor of the $\mathrm{EW_{Ly\alpha}}$ distribution, and that other parameters that systematically vary with redshift but are not reflected in the UV slope could affect this relation. However, as we have statistically demonstrated that our

new model provides a much-improved fit to the available data compared to using a combination of $M_{\rm UV}$ and redshift to predict Lyα emission, it is certainly the preferred choice. In the process of producing this model, we also considered various functional forms, and for the first time evaluated their goodness of fit in a statistically meaningful manner. In doing so, we have significantly reduced a systematic offset that skewed derived neutral fractions up to $\sim 3\%$ (Treu et al. 2012).

6.1.1.2 Lyα velocity offset

Just as Lyα can be easily scattered by neutral Hydrogen in the intergalactic medium, it is also strongly affected by neutral gas within the emitting galaxy and its circumgalactic medium. In typical LBGs, Lyα is often observed redshifted with respect to low ionization absorption lines (Shapley et al. 2003), as well rest-optical nebular emission lines which trace the cites of star formation. Steidel et al. (2010) offers a model able to explain these three independent observations whereby galaxies are surrounded by spherical outflows of cool gas accelerating radially outward. For Lyα to escape toward the observer through an optically thick shell, it must be backscattered off the side of the shell away from the observer, where it acquires a large enough velocity to shift out of resonance and pass through the front end of the shell unperturbed. At $2 < z < 2.6$, this results in a typical Lyα velocity offset with respect to systemic of $v_{Ly\alpha} \sim 400$ km s^{-1} in LBGs (Steidel et al. 2010), which was used to predict the IGM transparency at $z \geq 7$ in early simulations (e.g. Bolton & Haehnelt 2013). We note that although Dijkstra et al. (2011) calculate a Lyα velocity profile and offset using their radiative transfer code, their preferred model used to infer an IGM neutral fraction also peaks at $v_{Ly\alpha} \sim 400$ km s^{-1}.

In Section 4.4.5, using MOSFIRE to observe rest-optical [OIII] lines, we showed that the velocity offset is much lower, typically $v_{Ly\alpha} \sim 150$ km s^{-1}, in our sample of $z \sim 3.5$ LBGs, many of which display strong Lyα. Two potential causes are either a decrease in the HI column density of the shell, or a decrease in the covering fraction of neutral gas; our complementary work in Jones et al. (2013) appears to support the latter. Regardless of the cause, this decreased offset will result in Lyα being more readily absorbed by a neutral IGM, as the emission now requires a larger ionized bubble to shift out of resonance. Although our work has brought attention to this important effect, we must now await updated models from the theorists to take this into account. Future directions may also involve using CIII] 1909 or other rest-UV lines to get a measurement of this velocity offset in galaxies closer to the epoch of reionization.

6.1.1.3 Ionizing photon escape fraction

As recently pointed out by Dijkstra et al. (2014), an evolution in the escape fraction of ionizing photons will also affect the visibility of Lyα during the epoch of reionization. All other variables being equal, an increase in the escape fraction will result in less ionizing photons reprocessed into

nebular emission, and less Lyα. However, as the intensity of nebular emission is proportional to $(1 - f_{esc})$, if the escape fraction remains small, the change in Lyα emission strength will only be marginal. For example, a doubling of f_{esc} from 0.1 to 0.2 will only decrease the Lyα emission strength by 11%. Given the reasonably low escape fractions inferred where observations are possible (Nestor et al. 2013) and the presence of already strong nebular emission (e.g., Smit et al. 2014), we believe this is not likely to be a dominant source of uncertainty.

6.2 Understanding reionization in the context of observations

In addition to the direct measurements of reionization provided in this thesis through the $x_{\mathrm{Ly}\alpha}$ test, we have also provided valuable measurements of quantities directly related to reionization. In Chapter 3, we provided the deepest available constraints on the abundance of star-forming galaxies at $z \sim 7$ and 8, and in Chapter 4, we provided crucial corrections to the stellar mass density at the end of the reionization era. While these measurements are interesting in their own right in the context of early galaxy formation, they also play an important role in understanding the evolution of cosmic reionization and the role of galaxies in driving this process. In this section, we briefly review the results of Robertson et al. (2013), incorporating both these and other available constraints into a holistic model for cosmic reionization.

We begin by describing the equations that govern the reionization process, such that the reader can get an appreciation for the quantities, both measurements and estimates, that enter into our model to determine the evolution of reionization. We denote the volume-averaged ionized filling fraction of hydrogen as Q_{HII}. As reionization is governed by a balance of ionizing photons breaking apart neutral atoms and free electrons and protons recombining, its evolution is expressed by the differential equation:

$$\dot{Q}_{HII} = \frac{\dot{n}_{ion}}{\langle n_H \rangle} - \frac{Q_{HII}}{t_{rec}} \tag{6.1}$$

Here, the first term represents the comoving production rate of ionizing photons available to the IGM, $\dot{n}_{ion}$, normalized by the comoving density of hydrogen. As we cannot directly measure $\dot{n}_{ion}$, we express it as a product

$$\dot{n}_{ion} = f_{esc} \xi_{ion} \rho_{\mathrm{UV}} \tag{6.2}$$

Here, ρ_{UV} denotes the UV luminosity density, which we are able to readily measure by integrating our luminosity function from Chapter 3. ξ_{ion} then provides the conversion from M_{UV}, measured at 1500 Å, to a production rate of ionizing photons within the galaxy. The escape fraction, f_{esc}

denotes the fraction of these photons that are able to leave the confines of galaxies, rather than being absorbed by dust or hydrogen within the galaxy itself.

Next, we can express the recombination time, t_{rec} as

$$t_{rec} = [C_{HII}\alpha_B(T)(1 + Y_P/4X_P)\langle n_H\rangle(1+z)^3]^{-1} \tag{6.3}$$

The first term, C_{HII} denotes the so-called clumping factor, which takes into account the fact that we use the average comoving density in this equation, but the recombination rate will depend upon the square of the local density, which will vary throughout the IGM. $\alpha_B(T)$ denotes the Case B recombination coefficient and Y_P and X_P the primordial mass fractions of hydrogen and helium, respectively.

For completeness, we include the expression used to calculate the Thomson scattering optical depth as

$$\tau_e(z) = \int_0^z c\langle n_H\rangle\sigma_T f_e Q_{HII}(z')H(z')(1+z')^2 dz', \tag{6.4}$$

where c is the speed of light, σ_T is the Thomson cross section, and $H(z)$ is the redshift-dependent Hubble parameter. Having detailed the simple set of equations that govern the model, we will now describe both the observational inputs and assumptions that enter before moving on to an analysis of the results.

6.2.1 Observational constraints

6.2.1.1 UV luminosity densities

For any reionization scenario driven by star-forming galaxies, the most obvious input is a measurement of galaxy abundance. In Chapter 3, using the deepest near-infrared images from UDF12, we completed such a measurement. To incorporate these results into the model, we chose to utilize the integrated constraints on Schechter function parameters, rather than individual abundances as a function of luminosity from the stepwise maximum likelihood function. With this formalism, we can easily extend the UV luminosity density below our observable limit of $M_{\rm UV} = -17.0$, and compute errors on this utilizing the uncertainties on Schechter parameters. We choose to consider three limits: $M_{\rm UV}= -17, -13$, and -10. The first limit is motivated by understanding whether currently observed galaxies are capable of driving the reionization process, while the third represents an extreme scenario, perhaps near the limit at which star formation will be suppressed (Read et al. 2006). The intermediate value of $M_{\rm UV} = -13$ represents a compromise between these extremes, and is well matched by the observable limit of the luminosity function at $z \sim 2$ from studies of lensed LBGs (Alavi et al. 2014). In addition to our measurements at $z \sim 7$ and 8, we augment the UDF12

luminosity functions with measurements at $4 < z < 6$ from Bouwens et al. (2007).

6.2.1.2 Stellar mass densities

As mentioned in Chapter 4, the stellar mass density of the universe provides an integral measurement of prior star formation, and thus an independent constraint on the production of ionizing photons. Thus, we use the nebular emission-corrected stellar mass densities from $z = 4, 5, 6$, and 7 as an additional constraint, with measurements integrated down to the same three limits as the UV luminosity density. We assume that 28% of stellar mass is returned to the ISM, appropriate for a Salpeter (1955) IMF from $M = 0.1 - 100 M_{\odot}$.

6.2.1.3 Thomson scattering optical depth

Our final observational constraint arises as an integral measurement from the cosmic microwave background. Through the EE polarization spectrum, one can measure the integrated optical depth to the surface of last scattering, τ_e, caused by free electrons in the intergalactic medium. In the context of our model this number is easily calculable for any given reionization history, though it is important to note that it is not unique. An early, extended reionization can yield the same value for τ_e as a reionization that is late and rapid. Four our constraint, we use the full marginalized likelihood curve from the 9-year WMAP data (Hinshaw et al. 2013).

6.2.2 Other inputs

Despite the observational data presented above, to arrive at a complete picture of the reionization process, it is necessary to make an additional number of well-justified estimates, which we detail here.

The first of these is the UV continuum to ionizing photon ratio. To arrive at our estimate for this quantity, we utilize a combination of the measurements of UV spectral slopes from Dunlop et al. (2012), discussed above, and the Bruzual & Charlot (2003) population synthesis models. Dunlop et al. (2012) found faint galaxies at both $z \sim 7$ and 8 have UV slopes consistent with $\beta = -2.0$, where $f_{\lambda} \propto \lambda^{\beta}$. However, this UV slope will not directly translate to an ionizing photon conversion rate, as a degeneracy between metallicity and reddening exists. A mature, metal-poor, but dusty population with $\beta = -2.0$ can yield a value of $\log_{10}(\xi_{ion})$ as low as 24.75 [s^{-1} / erg s^{-1} hz^{-1}], while a young, metal-rich population can produce $\log_{10}(\xi_{ion}) \sim 25.35$ (see Figure 6.1). Given that metals and dust should be produced somewhat in concert with each other, we disregard the low values produced by the metal-poor an dusty combination, and assume a value of $\log_{10}(\xi_{ion}) \sim 25.2$, bracketed by the remaining models.

The final number needed to convert to the rate of ionization in the intergalactic medium is the

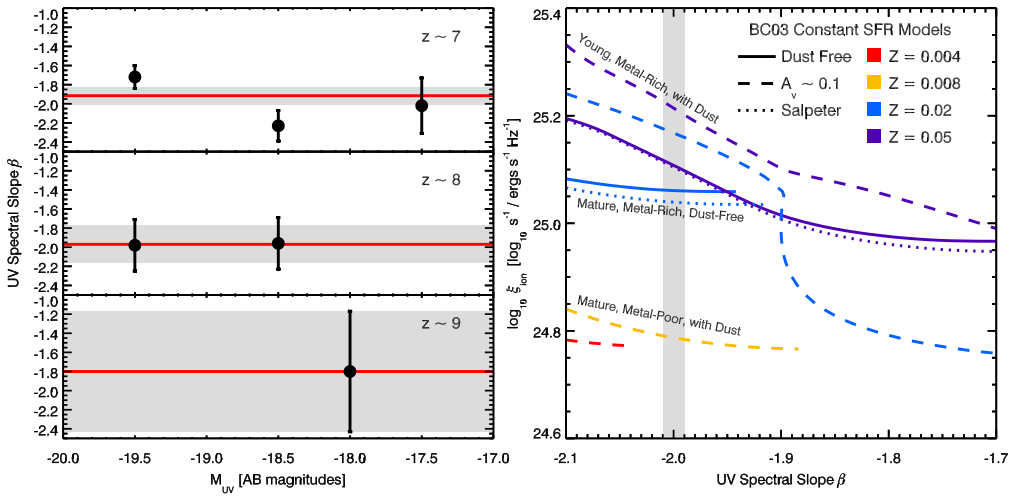

Figure 6.1 Left: Constraints on the ultraviolet spectral slope, β, for galaxies from the UDF12 imaging campaign at $z \sim 7$, 8, and 9 (Dunlop et al. 2013). While the error bars are still large, Dunlop et al. (2013) showed that at all of these redshifts, the population of $M_{UV} > -20$ galaxies are consistent with an intrinsic UV slope of $\beta = -2.0$. Right: Curves of ξ_{ion} versus UV slope from the Bruzual & Charlot (2003) population synthesis models with a constant star formation rate. The shaded area at $\beta = -2.0$ denotes the measured UV average slope of galaxies from out UDF12 campaign. Our assumed value of $\log_{10}(\xi_{ion}) \sim 25.2$ falls between the remaining models, once the mature, metal-poor but dusty models are excluded.

escape fraction of ionizing photons from within galaxies themselves, f_{esc}. Here, were are guided by observation, though at significantly lower redshifit. Due to the opacity of the IGM, this measurement can only be made at $z \leq 3.5$, and even then it is fraught with difficulty as it requires deep narrowband exposures and careful control of foreground contamination. Nonetheless, as this measurement is so crucial to an understanding of reionization, great effort has been put forth recently at $z \sim 0.8 - 3.5$. At $z \sim 0.8 - 1.3$ surveys have found tight upper limits on the population as a whole of $f_{esc} \lesssim 0.02$ (Siana et al. 2010; Bridge et al. 2010). In constrast, at $z \sim 3$ recent estimates put $f_{esc} \sim 0.05 - 0.07$ for LBGs and $\sim 0.1 - 0.3$ for LAEs (Nestor et al. 2013). Given this general upward trend with redshift, we assume a constant value of f_{esc}= 0.20 for our investigation, and discuss current and future constraints on this in Section 6.3.

Finally, we need a a value for the clumping factor of ionized hydrogen, defined as $C_{HII} = \langle n_H^2 \rangle / \langle n_H \rangle^2$, and the IGM temperature. These factors both affect the average recombination time of hydrogen in the universe, as denser gas will recombine at a more rapid rate given a higher rate of collisions between protons and electrons, and the recombination coefficient decreases with increasing temperature due to the importance of Coulomb focusing. We assume a value $C_{HII} = 3$, in the range of values derived from theoretical modeling in the literature (e.g., Pawlik et al. 2009; McQuinn et al. 2011; Finlator et al. 2012), and an IGM temperature of $T = 20,000$ K (Hui & Haiman 2003).

6.2.3 Results

We now discuss the model's most salient results. We begin by considering the integral UV luminosity density, ρ_{UV}, at redshifts $5 < z < 8$ as a function of $M_{\rm UV}$. At each redshift we consider, given our assumptions on the conversion to ionizing emissivity and the clumping factor, how far down the luminosity function we need to integrate such that galaxies can maintain reionization. Given Equation 6.1, this can be solved for by setting $\dot{Q}_{HI} = 0$, but note that as the recombination time decreases as $(1+z)^3$, the required ionizing emissivity increases correspondingly with redshift.

At $z \sim 5$ and 6, the population of galaxies down to the UDF12 limit of $M_{\rm UV}= -17$ is sufficient to maintain reionization, but we see that these photons quickly fall short. At $z \sim 7$, the observed population falls short by 0.3 dex, while by $z \sim 8$ this shortfall has increased to 0.6 dex. This is a key result of the UDF12 project - if our assumptions on the ionizing photon production rate and escape fraction of $z \geq 7-8$ galaxies are correct, the observed population cannot reionize the universe.

We now turn to an analysis of the best fitting model taking into account all constraints. As mentioned previously, this model fits to the measured star formation rate densities, stellar mass densities (both functions of redshift), and the optical depth due to Thomson scattering. To model the star formation rate density of the universe, we use a double power law, anchored by the UV luminosity densities at $z \sim 4$ and $z \sim 7$. We express this as:

$$\rho_{\rm UV}(z) = \rho_{{\rm UV},z=4}(\frac{z}{4})^{-3} + \rho_{{\rm UV},z=7}(\frac{z}{7})^{\gamma} \tag{6.5}$$

Both simpler and more complex models were explored, but any single power-law model tends to be dominated by the low-redshift decline in star-formation and has difficulty producing the Thomson optical depth, while generic broken double power laws are disfavored based on their Bayesian information relative to the model used here.

We show the results of the full modeling procedure in Figure 6.2. The upper left panel confirms that our model provides a generally good fit to the UV luminosity data. The low-redshift data points are well fit, with the most salient features being an extended tail of star formation out to $z > 12$, and a slight oveprediction of our preliminary $\rho_{\rm UV}$ measurement at $z \sim 9$. Both these are driven by a need to match the Thomson scattering optical depth. As seen in the lower right panel, even with our extended low level of star-formation, our model is just barely reaches the WMAP 1σ error contour. Additionally, our stellar masses are well matched, but with the measurements at $z \sim 7$ slightly overpredicted by the models. We note that an increase in the ionizing efficiency at $z > 7$, caused by either more metal-poor, less dusty stellar populations, or an increase in f_{esc} would assist in resolving this tension.

Our full model indicates that under our assumptions, the currently observed population down to $M_{\rm UV} = -17$ cannot reionize the universe. This model severely underpredicts the Thomson optical

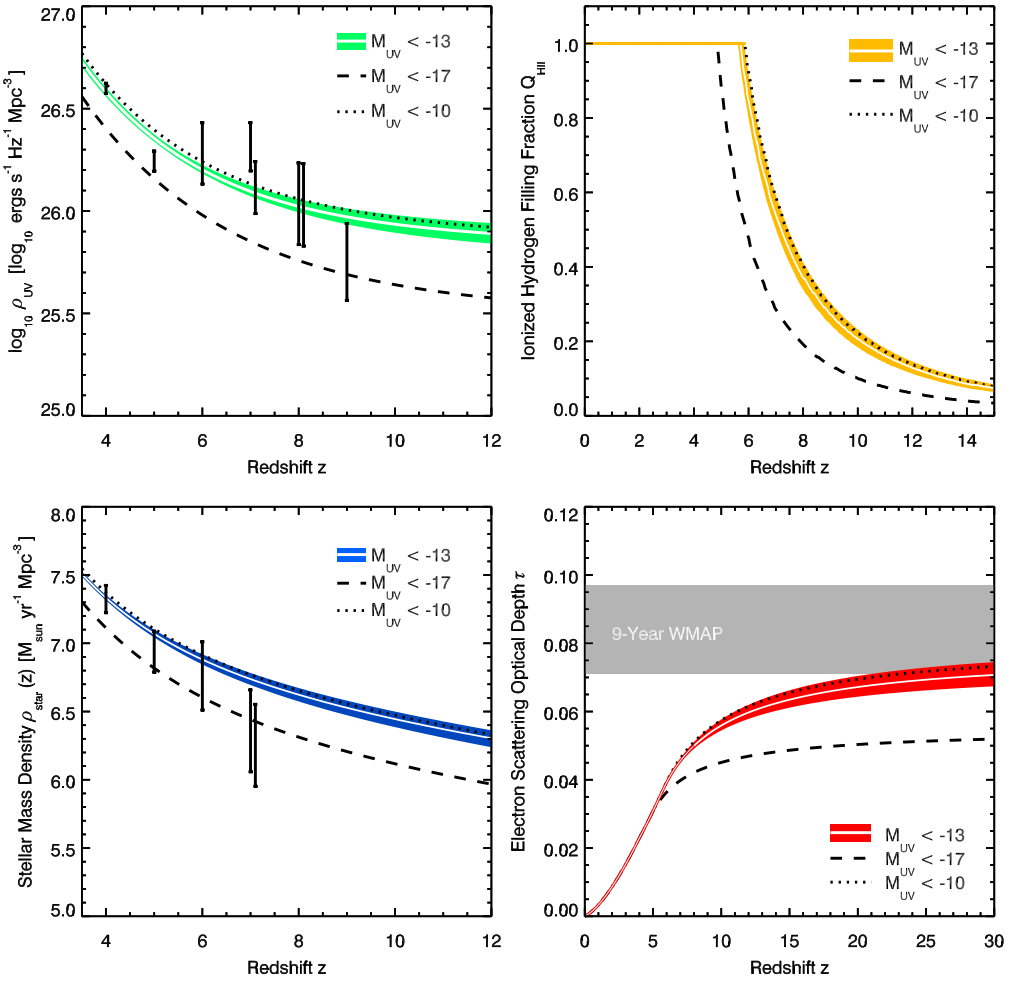

Figure 6.2 Best-fitting models for reionization along with associated observational constraints. Note that although we only plot the UV luminosity density and stellar mass density constraints appropriate for $M_{\rm UV}< -13$, each model is fit with data integrated to the appropriate limit. Clockwise from upper right: Ionized hydrogen filling fraction, Thomson scattering optical depth, τ_e, stellar mass density, $\rho_{star}(z)$, and UV luminosity density $\rho_{UV}(z)$. Note that although $\rho_{star}(z)$ and $\rho_{UV}(z)$ are constraints at various redshifts which must all be matched, the Thomson scattering optical depth is an integral constraint that must only be matched integrating out to the surface of last scattering at $z \sim 1100$.

depth, and as a result favors a late reionization that does not conclude until $z \sim 5$, well after we have evidence of the universe being highly ionized. Extrapolating to $M_{\rm UV} = -10$ provides little change in the derived predictions, and a reionization that completes slightly earlier. Thus, perhaps the most important synthesis from the UDF12 project is that, provided our assumptions on the escape fraction, ionizing photon production rate, and clumping factor and an extension of the luminosity function to $M_{UV} \sim -13$ are reasonable, galaxies can reionize the universe without the need for extreme stellar populations.

We conclude this section by considering the results of our reioniziation mode, $Q_{HII}(z)$ against various observational probes of reionization, none of which were included in the fitting process of our model. The model, its associated errors, and the various other data are summarized in Figure 6.3. Remarkably, our results are consistent with nearly every independent probe, with the exception of the Lyα-forest transmission constraints at the tail end of reionization from Fan et al. (2006). This failure should be expected, however, since our simplistic model does not account for the increase in the clumping factor which occurs at the tail end of reionization, when only the most dense pockets of neutral gas that have the highest recombination rates remain (Furlanetto & Oh 2005). More importantly, our model successfully reproduces the upper limits on the neutral fraction from quasar dark gap statistics (McGreer et al. 2011), GRB damping wing absorption (McQuinn et al. 2008), Lyα galaxy clustering (McQuinn et al. 2007), and Lyα emitters (Ouchi et al. 2010). We add to this the latest results from our survey in Chapter 5, a value of $(1 - Q_{HII}) = 0.51^{+0.05}_{-0.09}$ at $z \sim 7$ and $(1 - Q_{HII}) > 0.68$ at $z \sim 8$. These results too compare favorably to the model, with the error bars overlapping at $z \sim 7$, and a prediction of $(1-Q_{HII}) = 0.63$ at $z \sim 8$. Altogether, these results which perhaps would have been surprising a few years ago, point to a rapid increase in the neutral fraction at $z > 6.5$ with an extended period of low-level ionization necessary to reproduce the Thomson optical depth.

6.3 Future directions

I will now consider the current and future developments that will further shape our view of this early era. I have chosen to divide this section into a discussion of high redshift galaxy searches and detailed studies followed by the prospects for improved measurements of the IGM neutral fraction during the epoch of reionization.

6.3.1 High redshift galaxies

With observations already underway, the HST Frontier Fields (GO/DD 13495, PI: Lotz) are set to significantly advance our view of the $z > 7$ universe. This program will take advantage of gravitational lensing to observe $4-6$ cluster-blank field pairs with 70 orbits each of ACS and WFC3

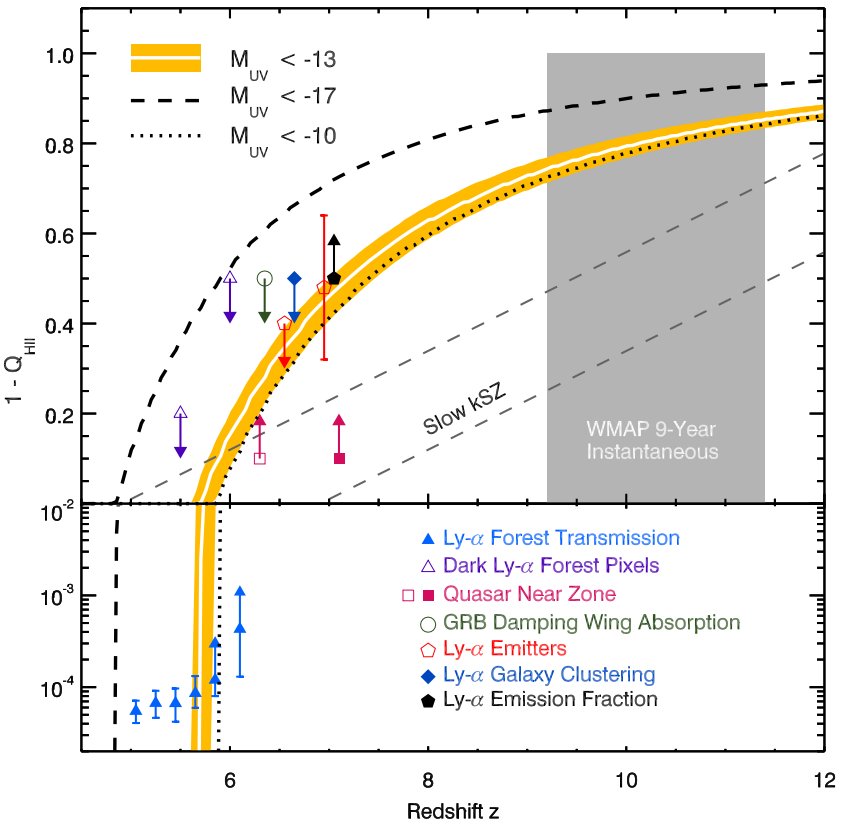

Figure 6.3 Evolution of the volume-averaged neutral fraction, $(1 - Q_{HII})$ for our best fit models, along with various observational constraints on reionization. Citations for each constraint are given in the text.

imagin, roughly following the observational strategy our team developed for UDF12 with a deep Y_{105} filter for $z > 8.5$ rejection and uniform depths in J_{125}, J_{140}, and H_{160}. Altogether, this will increase the existing search area for faint ($m_{obs} \sim 29$) high-redshift galaxies $3-4\times$. Even more importantly, through the lensing boost provided, the HST FF program may detect $\gtrsim 100$ new galaxies at $z \sim 7-8$ with intrinsic brightnesses below the UDF12 blank field limit of $M_{\rm UV}= -17$. This will both help pin down the faint end slope of the luminosity function to even greater precision, as shown in Figure 6.4, and decrease the contribution of cosmic variance providing $4-6$ fully independent new sightlines. Additionally, numerous detections would help rule out a possible turnover in the luminosity function faint end slope for low-mass halos unable to shield their own molecular hydrogen (e.g., Kuhlen & Faucher-Giguère 2012), thereby verifying or otherwise the extrapolation of the faint-end slope used in our model. Unfortunately, the first results from A2744 have been somewhat underwhelming, with the discovery of only one $z \sim 8$ object (Atek et al. 2014), and have resulted in questions about whether the program will reach the proposed goals.

Nonetheless, the frontier fields should still clarify numerous other open problems at high redshift. These will include a much improved measurement of the star-formation rate density at $z \sim 9-10$ as well as improved estimates of the UV slopes (and thus stellar properties) of $z \sim 7$ galaxies given that prior to the program, the UDF was the only field with requisite deep imaging in the J_{140} filter.

Ground-based surveys will also play a large role in adding to our view of the universe at $z \sim 7$, the highest redshift for which the infrared sky does not render photometry prohibitively difficult. Already, the UltraVISTA survey (McCracken et al. 2012) has produced tentative evidence that the bright end of the $z \sim 7$ luminosity function may follow a power law decline, rather than a Schechter function exponential cutoff (Bowler et al. 2014). This provides valuable input for galaxy formation scenarios, potentially indicating that feedback at the bright end of the luminosity function was not effective during this early area. In the coming years, UltraVISTA will devote another 2000 hours to continue their broadband, near-infrared survey, which should verify or otherwise this key result, and provide further bright ($Y < 25.5$) sources for spectroscopic follow up.

Recent breakthroughs in instrumentation will also assist in the spectroscopic confirmation of these galaxies in the coming years. The arrival of MOSFIRE, the near-infrared, multi-object spectrograph on the Keck I telescope, and the commissioning of KMOS, a similar instrument on the VLT, have significantly expanded our capability to search for Lyα at $z \geq 7$. Although we presented exciting spectroscopic progress from the MOSFIRE extension of our Keck survey in Chapter 5, this represented a total of only ~ 7 hours of on-sky integration. Given the new $z \geq 7$ targets that should be discovered in the Frontier Fields as well as ground based searches, the prospect of pushing back the redshift barrier is great. Tantalizingly, a number of bright $z \sim 10$ candidates within the reach of spectroscopy with 10m-class telescopes were recently discovered in GOODS-N (Oesch et al. 2014).

New avenues of investigation will also be opened in the sub-mm with ALMA. Rotational tran-

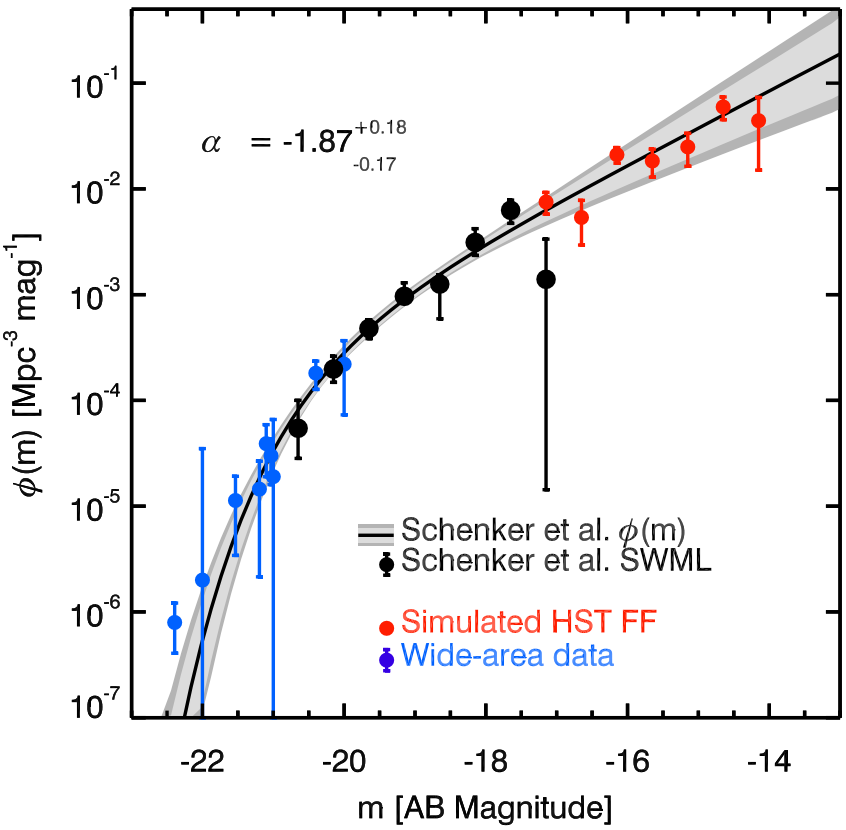

Figure 6.4 Simulated $z \sim 7$ UV luminosity function from the completed 6 HST frontier fields. Light and dark grey regions show the current 68% confidence intervals from our study in Chapter 3 neglecting and including a contribution from cosmic variance, respectively. As seen from the simulated (red) data points, the continuation of the faint end slope should be easily testable with these powerful new observations.

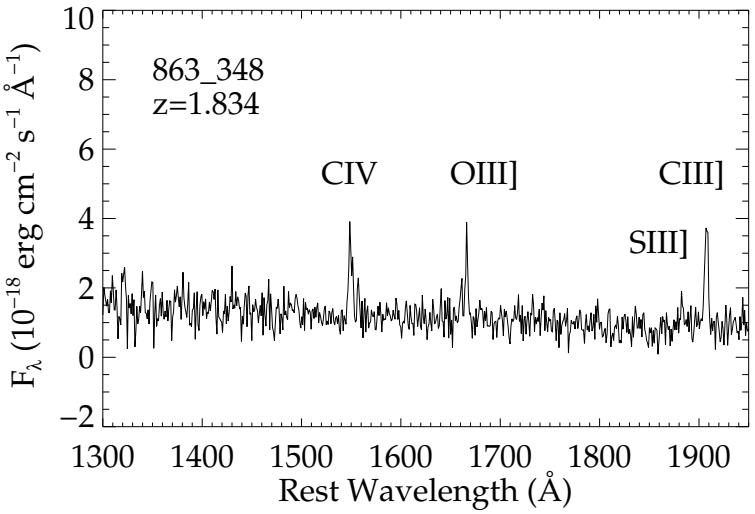

Figure 6.5 Rest-UV tpectrum of a lensed low mass galaxy from the CASSOWARY sample (Stark et al. 2013b). No less than four UV emission lines are visible, demonstrating the potential for using these lines to understand physical conditions in lensed galaxies at $z \sim 6$ with the new generation of infrared spectrographs.

sitions of the CO line have the potential to both measure spectroscopic redshifts, and for the first time, give us information on the gas content of early galaxies. The [CII] 158 μm line, originating in photodissociation regions (PDRs) and tightly correlated with star-formation rates in the local universe also provides a promising avenue for spectroscopic confirmation. However, within the last year both Ouchi et al. (2013) and Ota et al. (2014) have searched for this line in $z \sim 7$ LAEs, only to find upper limits to the luminosity over an order of magnitude below the brightness expected from the low-redshift relationship. Possibilities include low metallicities or increased PDR densities that collisionally de-excite [CII], though the true cause remains unknown.

In addition to mere source discovery, the prospects of observing rest-UV emission lines in order to understand the nebular environments of high-redshift galaxies is also excellent. Already, our detection of CIII] 1909 Å presented in Chapter 5 represents the first emission line detection from a $z \geq 7$ galaxy other than Lyα. To demonstrate the prospect of further progress, in Figure 6.5, we show the rest-UV spectrum of a low mass $z \sim 2$, lensed galaxy from the CASSOWARY survey (Stark et al. 2013b). Combined with photonioization modeling, we can hope to extract a wealth of information from similar spectra: metallicies by comparing metal line strengths to HeII 1640, ionization parameters from CIII] to CIV ratios, and density constraints by looking at doublet emission line ratios. With the selection of bright $z \sim 6$, lensed galaxies from CLASH and spectroscopy with NIRSPEC, and soon NIRES, there is great potential for learning about nebular conditions in typical high-redshift galaxies for the first time.

The past few years have also seen significant progress in terms of narrowing down the escape fraction of ionizing photons for high redshift galaxies, a key assumption for our calculations in Section 6.2. As mentioned previously, Nestor et al. (2013) found an escape fraction for $z \sim 3$ LAEs of $\sim 0.1-0.3$, roughly three times greater than that seen in LBGs at the same redshift. Additionally, Stark et al. (2010) and Stark et al. (2011), the showed Ly$\alpha-$emitting fraction of LBGs steadily increases from $3 < z < 6$, where $> 50\%$ of faint LBGs would be classified as LAEs ($\mathrm{EW_{Ly\alpha}} > 25$ Å) at $z \sim 6$, thus implying that the typical LBG escape fraction increases with redshift. Jones et al. (2013) find that the covering fraction of low-ionization absorption lines, which should trace neutral hydrogen as well, decreases with increasing $\mathrm{EW_{Ly\alpha}}$, providing further circumstantial evidence for an increase in f_{esc}. More recently, through modelling of the Lyα forest, Becker & Bolton (2013) estimate that the ionizing to rest-UV emissivity of galaxies increases approximately threefold from $z \sim 3.25$ to 4.75. Bracketing the other side of our estimate, we know that the escape fraction must still be significantly below unity from observations of intense rest-optical nebular emission using Spitzer/IRAC photometry in $z \sim 6.8$ galaxies (Smit et al. 2014). In terms of future prospects, narrowband imaging with HST, coupled with Spitzer photometry may also help isolate the escape fractions and stellar populations of individual star-forming clumps within $z \sim 3$ galaxies, but direct progress is still a difficult undertaking (Nestor et al. 2013).

In the longer term, JWST is set to revolutionize the both search for, and our understanding of high-redshift galaxies. NIRCam will provide simultaneous photometry in separate short- and long-wavelength channels, covering a spectral range from 0.6-5.0 μm, and able to reach a limit of $m_{AB} \sim 31$ in deep, blank fields, 1.5 mag deeper than our UDF12 limits. This will significantly boost our rest-UV search capability for galaxies at $z \geq 7$, and more importantly at $z \geq 9$, where currently we are only able to uncover the rapidly declining bright end of the luminosity function. Perhaps more importantly, at $\lambda > 1.7\mu$m JWST will feature a $\sim 100\times$ gain in collecting area over Spitzer, enabling stellar masses to be precisely determined.

NIRSpec should prove just as informative. As a multi-object spectrograph with a microshutter array, it will be able to observe ~ 100 targets simultaneously. In $R \sim 100$ prism mode, NIRSpec will be able to verify high-redshift candidates using continuum breaks down to $m_{AB} \sim 29$, only 0.5 mag brighter than the current UDF12 photometric limit. With a wavelength range of $0.6 - 5.0\mu$m, simultaneous coverage of rest-UV and rest-optical emission lines will be possible to $z \sim 10$, providing glimpses of nebular conditions in galaxies near our photometric detection thresholds today.

6.3.2 Neutral fraction measurements

We begin our discussion of future prospects of measuring the ionization state of the IGM with the Lyman alpha fraction test, already discussed at length in Chapters 2 and 5. Only over the last 2 years have observers had access to the MOSFIRE instrument, but already three groups including

our own have come out with measurements of this fraction at $z \sim 8$, proving the first evidence for a continued increase in x_{HI} with redshift from $z \sim 7$ to $z \sim 8$ (Treu et al. 2013; Tilvi et al. 2014). However, even with this effort, there have still been only 36 galaxies surveyed at $z \sim 8$, roughly half of the sample accumulated at $z \sim 7$, leaving room for progress.

Performing the $\mathrm{x_{Ly\alpha}}$ test with space telescopes also represents another exciting prospect in the coming years. This method has the obvious advantage of being above the atmosphere, eliminating the effects of infrared skylines, atmospheric transmission, and background. The elimination of skylines and transmission concerns also eliminates the need for complex Monte Carlo simulations using objects' redshift probability distributions, as the limiting sensitivity is now a smooth function of wavelength across the entire spectral range. However, the low spectral resolution of prism/grism surveys, which will not allow identification of the typical asymmetric Lyα profile, presents a potential drawback. The GLASS survey is already undertaking such studies with WFC3 on HST, but first results have yielded limiting sensitivities of only $\sim 2.5 \times 10^{-17}$ erg cm^{-2}s^{-1}, roughly 5$\times$ larger than those achievable from the ground, severely limiting the utility of these observations (Schmidt et al. 2014). The continuous $0.6 - 5.0\mu$m spectral coverage and order of magnitude sensitivity increase that will become available with NIRSpec on JWST, however, make this an exciting prospect.

The new infrared-sensitive Hyper Suprime-cam on the Subaru telescope will complement efforts on the $\mathrm{x_{Ly\alpha}}$ test by undertaking searches for Lyman alpha emitters at $z = 7.3$. Plans for a 6 night LAE survey are already in place, which will increase the area covered in the recent Suprime-cam $z = 7.3$ LAE survey (Konno et al. 2014) by nearly a factor of 10. Such a wide area survey has the potential to, for the first time, detect the presence of LAE clustering caused by ionized bubbles in the IGM, and thus break the degeneracy between an increasing neutral fraction and intrinsic decrease in the LAE population.

With the upcoming data release of Planck, we can expect improved CMB-derived constraints on the reionization era. Projections for the errors on the Thomson scattering optical depth, τ_e, measurement are only a third as large as those realized by the WMAP 9-year results (Efstathiou et al. 2005), as Planck should be cosmic variance limited for polarization on large angular scales. Perhaps more importantly, Zaldarriaga et al. (2009) points out that with principal component analysis of the Planck polarization data, it should be possible to decompose the contributions to τ_e from different coarse redshift intervals, i.e., measurements of $\tau_{e,6<z<10}$ and $\tau_{e,z>10}$. Such measurements would provide a powerful probe of early star formation prior to the launch of JWST. Additionally, there remains potential for measurements of the duration of patchy reionization through the kinetic Sunyaev-Zel'dovich effect from CMB experiments concentrating on small angular scales, such as the South Pole Telescope (Carlstrom et al. 2011) and the Atacama Cosmology Telescope (Kosowsky 2006).

Finally, we summarize the prospects of 21 cm experiments, which have yet to place meaningful

constraints on reionization, but hold great promise in the coming years. This technique, reviewed in detail by Furlanetto et al. (2006), attempts to map out the epoch of reionization by directly measuring the brightness temperature of the hyperfine 21 cm transition of hydrogen in the ground state at these times. As this is a spectral feature with a discrete wavelength, it has the potential to produce a full three dimensional map of the neutral regions during the epoch of reionization. However, such measurements will not be achievable until far in the future, as there are still many hurdles to be overcome. The brightness temperature of galactic foregrounds is roughly four orders of magnitude greater than that expected from the 21 cm reionization signal, creating enormous issues in background subtraction. In addition, other technical challenges must be dealt with, such as contamination from terrestrial sources and ionospheric distortion of the incoming signal (Furlanetto et al. 2006).

In the meantime, a number of groups are embarking on attempts to measure the statistical signal from the latter stages of reionization in the 21 cm power spectrum, including PAPER/HERA (Parsons et al. 2010), the Murchison Wide field Array (Tingay et al. 2012), and the Low Frequency Array (Yatawatta et al. 2013). An additional group is also attempting to measure this signal during the earliest stages of reionization at $z \geq 15$ (Greenhill & Bernardi 2012). As an integral measurement of the power as a function of scale, the sensitivity requirements are far less than that of direct detection, while still being able to inform us about the neutral fraction and ionized bubble size during this crucial era. Additionally, it has recently been realized that galactic foregrounds are confined to a definite region in two-dimensional Fourier space, and thus measuring the reionization power spectrum in the uncontaminated region can obviate the need for background subtraction (Pober et al. 2013).

Progress in the last decade has transformed our knowledge of this early era, providing substantial evidence for a rapid conclusion to reionization at $z \sim 6.5$, as well as measurements of early galaxy abundance all the way back to $\sim 5\%$ of the present age of the universe. I consider myself truly fortunate to have been able to contribute to this knowledge with the projects I have presented here, and await the exciting results sure to come from this next generation of instruments and experiments.

Bibliography

Adelberger, K. L., Steidel, C. C., Giavalisco, M., et al. 1998, ApJ, 505, 18

Alavi, A., Siana, B., Richard, J., et al. 2014, ApJ, 780, 143

Anders, P., & Fritze-v. Alvensleben, U. 2003, A&A, 401, 1063

Atek, H., Siana, B., Scarlata, C., et al. 2011, ApJ, 743, 121

Atek, H., Richard, J., Kneib, J.-P., et al. 2014, ApJ, 786, 60

Bayliss, M. B., Rigby, J. R., Sharon, K., et al. 2013, ArXiv e-prints, arXiv:1310.6695

Becker, G. D., & Bolton, J. S. 2013, MNRAS, 436, 1023

Becker, R. H., Fan, X., White, R. L., et al. 2001, AJ, 122, 2850

Beckwith, S. V. W., Stiavelli, M., Koekemoer, A. M., et al. 2006, AJ, 132, 1729

Bertin, E., Mellier, Y., Radovich, M., et al. 2002, in Astronomical Society of the Pacific Conference Series, Vol. 281, Astronomical Data Analysis Software and Systems XI, ed. D. A. Bohlender, D. Durand, & T. H. Handley, 228

Bolton, J. S., & Haehnelt, M. G. 2013, MNRAS, 429, 1695

Bolton, J. S., Haehnelt, M. G., Warren, S. J., et al. 2011, MNRAS, 416, L70

Bouwens, R. J., Illingworth, G. D., Franx, M., & Ford, H. 2007, ApJ, 670, 928

—. 2008, ApJ, 686, 230

Bouwens, R. J., Thompson, R. I., Illingworth, G. D., et al. 2004, ApJ, 616, L79

Bouwens, R. J., Illingworth, G. D., Oesch, P. A., et al. 2010a, ApJ, 709, L133

—. 2010b, ApJ, 708, L69

—. 2011, ApJ, 737, 90

—. 2012a, ApJ, 752, L5

—. 2012b, ApJ, 754, 83

—. 2013, ArXiv e-prints, arXiv:1306.2950

Bowler, R. A. A., Dunlop, J. S., McLure, R. J., et al. 2012, MNRAS, 426, 2772

—. 2014, MNRAS, 440, 2810

Bradley, L. D., Trenti, M., Oesch, P. A., et al. 2012a, ApJ, 760, 108

Bradley, L. D., Bouwens, R. J., Zitrin, A., et al. 2012b, ApJ, 747, 3

Bradley, L. D., Zitrin, A., Coe, D., et al. 2013, ArXiv e-prints, arXiv:1308.1692

Brammer, G. B., van Dokkum, P. G., & Coppi, P. 2008, ApJ, 686, 1503

Brammer, G. B., van Dokkum, P. G., Illingworth, G. D., et al. 2013, ApJ, 765, L2

Bridge, C. R., Teplitz, H. I., Siana, B., et al. 2010, ApJ, 720, 465

Broadhurst, T. J., Ellis, R. S., & Shanks, T. 1988, MNRAS, 235, 827

Bromm, V. 2013, Reports on Progress in Physics, 76, 112901

Bruzual, G., & Charlot, S. 2003, MNRAS, 344, 1000

Bruzual A., G., & Kron, R. G. 1980, ApJ, 241, 25

Bunker, A. J., Caruana, J., Wilkins, S. M., et al. 2013, MNRAS, 430, 3314

Bunker, A. J., Stanway, E. R., Ellis, R. S., & McMahon, R. G. 2004, MNRAS, 355, 374

Bunker, A. J., Stanway, E. R., Ellis, R. S., McMahon, R. G., & McCarthy, P. J. 2003, MNRAS, 342, L47

Bunker, A. J., Wilkins, S., Ellis, R. S., et al. 2010, MNRAS, 409, 855

Calzetti, D., Armus, L., Bohlin, R. C., et al. 2000, ApJ, 533, 682

Calzetti, D., Kinney, A. L., & Storchi-Bergmann, T. 1994, ApJ, 429, 582

Carlstrom, J. E., Ade, P. A. R., Aird, K. A., et al. 2011, PASP, 123, 568

Caruana, J., Bunker, A. J., Wilkins, S. M., et al. 2012, MNRAS, 427, 3055

Casertano, S., de Mello, D., Dickinson, M., et al. 2000, AJ, 120, 2747

Castellano, M., Fontana, A., Paris, D., et al. 2010, A&A, 524, A28

Chabrier, G. 2003, PASP, 115, 763

Coe, D., Benítez, N., Sánchez, S. F., et al. 2006, AJ, 132, 926

Colless, M., Ellis, R. S., Broadhurst, T. J., Taylor, K., & Peterson, B. A. 1993, MNRAS, 261, 19

Colless, M., Ellis, R. S., Taylor, K., & Hook, R. N. 1990, MNRAS, 244, 408

Cowie, L. L., & Hu, E. M. 1998, AJ, 115, 1319

Cowie, L. L., Hu, E. M., & Songaila, A. 2011, ApJ, 735, L38

Crampton, D., Cowley, A. P., & Hartwick, F. D. A. 1987, ApJ, 314, 129

Davé, R., Oppenheimer, B. D., & Finlator, K. 2011, MNRAS, 415, 11

Davis, M., & Wilkinson, D. T. 1974, ApJ, 192, 251

de Barros, S., Schaerer, D., & Stark, D. P. 2014, A&A, 563, A81

Dickinson, M., Stern, D., Giavalisco, M., et al. 2004, ApJ, 600, L99

Dijkstra, M., Mesinger, A., & Wyithe, J. S. B. 2011, MNRAS, 414, 2139

Dijkstra, M., Wyithe, S., Haiman, Z., Mesinger, A., & Pentericci, L. 2014, MNRAS, 440, 3309

Djorgovski, S., Spinrad, H., McCarthy, P., & Strauss, M. A. 1985, ApJ, 299, L1

Dunlop, J. S., McLure, R. J., Robertson, B. E., et al. 2012, MNRAS, 420, 901

Dunlop, J. S., Rogers, A. B., McLure, R. J., et al. 2013, MNRAS, 432, 3520

Edge, D. O., Shakeshaft, J. R., McAdam, W. B., Baldwin, J. E., & Archer, S. 1959, MmRAS, 68, 37

Efstathiou, G., Ellis, R. S., & Peterson, B. A. 1988, MNRAS, 232, 431

Efstathiou, G., Lawrence, C., Tauber, J., & et al. 2005, PLANCK - The Scientific Programme, ESA-SCI(2005)1, PLANCK Bluebook (ESA-SCI(2005)1)

Eisenstein, D. J., & Hu, W. 1998, ApJ, 496, 605

Ellis, R. S., & Allen, D. A. 1983, MNRAS, 203, 685

Ellis, R. S., Colless, M., Broadhurst, T., Heyl, J., & Glazebrook, K. 1996, MNRAS, 280, 235

Ellis, R. S., McLure, R. J., Dunlop, J. S., et al. 2013, ApJl, 763, L7

Erb, D. K., Pettini, M., Shapley, A. E., et al. 2010, ApJ, 719, 1168

Erb, D. K., Steidel, C. C., Shapley, A. E., et al. 2006, ApJ, 647, 128

Eyles, L. P., Bunker, A. J., Ellis, R. S., et al. 2007, MNRAS, 374, 910

Eyles, L. P., Bunker, A. J., Stanway, E. R., et al. 2005, MNRAS, 364, 443

Fan, X., White, R. L., Davis, M., et al. 2000, AJ, 120, 1167

Fan, X., Narayanan, V. K., Lupton, R. H., et al. 2001, AJ, 122, 2833

Fan, X., Strauss, M. A., Becker, R. H., et al. 2006, AJ, 132, 117

Fazio, G. G., Hora, J. L., Allen, L. E., et al. 2004, ApJS, 154, 10

Feroz, F., & Hobson, M. P. 2008, MNRAS, 384, 449

Feroz, F., Hobson, M. P., & Bridges, M. 2009, MNRAS, 398, 1601

Finkelstein, S. L., Papovich, C., Giavalisco, M., et al. 2010, ApJ, 719, 1250

Finkelstein, S. L., Hill, G. J., Gebhardt, K., et al. 2011, ApJ, 729, 140

Finkelstein, S. L., Papovich, C., Ryan, R. E., et al. 2012a, ApJ, 758, 93

Finkelstein, S. L., Papovich, C., Salmon, B., et al. 2012b, ApJ, 756, 164

Finkelstein, S. L., Papovich, C., Dickinson, M., et al. 2013, Nature, 502, 524

Finlator, K., Oh, S. P., Özel, F., & Davé, R. 2012, MNRAS, 427, 2464

Fontana, A., Vanzella, E., Pentericci, L., et al. 2010, ApJ, 725, L205

Fosbury, R. A. E., Villar-Martín, M., Humphrey, A., et al. 2003, ApJ, 596, 797

Fukugita, M., & Kawasaki, M. 2003, MNRAS, 343, L25

Fumagalli, M., Patel, S. G., Franx, M., et al. 2012, ApJ, 757, L22

Furlanetto, S. R., & Oh, S. P. 2005, MNRAS, 363, 1031

Furlanetto, S. R., Oh, S. P., & Briggs, F. H. 2006, Phys. Rep., 433, 181

Giavalisco, M., Ferguson, H. C., Koekemoer, A. M., et al. 2004, ApJl, 600, L93

Glazebrook, K., Ellis, R., Colless, M., et al. 1995, MNRAS, 273, 157

Gonzalez, V., Bouwens, R., llingworth, G., et al. 2012, ArXiv e-prints, arXiv:1208.4362

González, V., Labbé, I., Bouwens, R. J., et al. 2011, ApJl, 735, L34

—. 2010, ApJ, 713, 115

Grazian, A., Castellano, M., Fontana, A., et al. 2012, A&A, 547, A51

Greenhill, L. J., & Bernardi, G. 2012, ArXiv e-prints, arXiv:1201.1700

Grogin, N. A., Kocevski, D. D., Faber, S. M., et al. 2011, ApJs, 197, 35

Gruzinov, A., & Hu, W. 1998, ApJ, 508, 435

Gunn, J. E., & Peterson, B. A. 1965, ApJ, 142, 1633

Guo, Y., Ferguson, H. C., Giavalisco, M., et al. 2013, ApJS, 207, 24

Hainline, K. N., Shapley, A. E., Kornei, K. A., et al. 2009, ApJ, 701, 52

Hall, P., & Mackay, C. D. 1984, MNRAS, 210, 979

Hashimoto, T., Ouchi, M., Shimasaku, K., et al. 2013, ApJ, 765, 70

Hathi, N. P., Ryan, Jr., R. E., Cohen, S. H., et al. 2010, ApJ, 720, 1708

Hayes, M., Laporte, N., Pelló, R., Schaerer, D., & Le Borgne, J.-F. 2012, MNRAS, 425, L19

Hayes, M., Schaerer, D., Östlin, G., et al. 2011, ApJ, 730, 8

Hinshaw, G., Larson, D., Komatsu, E., et al. 2013, ApJS, 208, 19

Holder, G. P., Haiman, Z., Kaplinghat, M., & Knox, L. 2003, ApJ, 595, 13

Hui, L., & Haiman, Z. 2003, ApJ, 596, 9

Jones, T., Stark, D. P., & Ellis, R. S. 2012, ApJ, 751, 51

Jones, T. A., Ellis, R. S., Schenker, M. A., & Stark, D. P. 2013, ApJ, 779, 52

Kaplinghat, M., Chu, M., Haiman, Z., et al. 2003, ApJ, 583, 24

Kashikawa, N., Shimasaku, K., Matsuda, Y., et al. 2011, ApJ, 734, 119

Kelson, D. D. 2003, PASP, 115, 688

Kennicutt, Jr., R. C. 1998, ARA&A, 36, 189

King, C. R., & Ellis, R. S. 1985, ApJ, 288, 456

Koekemoer, A. M., Fruchter, A. S., Hook, R. N., & Hack, W. 2003, in HST Calibration Workshop : Hubble after the Installation of the ACS and the NICMOS Cooling System, ed. S. Arribas, A. Koekemoer, & B. Whitmore, 337

Koekemoer, A. M., Faber, S. M., Ferguson, H. C., et al. 2011, ApJs, 197, 36

Koekemoer, A. M., Ellis, R. S., McLure, R. J., et al. 2013, ApJs, 209, 3

Konno, A., Ouchi, M., Ono, Y., et al. 2014, ArXiv e-prints, arXiv:1404.6066

Kosowsky, A. 2006, New Astronomy Reviews, 50, 969

Kriek, M., Labbé, I., Conroy, C., et al. 2010, ApJ, 722, L64

Kron, R. G. 1980, ApJS, 43, 305

Kroupa, P. 2001, MNRAS, 322, 231

Krueger, H., Fritze-v. Alvensleben, U., & Loose, H.-H. 1995, A&A, 303, 41

Krumholz, M. R., & Dekel, A. 2012, ApJ, 753, 16

Kuhlen, M., & Faucher-Giguère, C.-A. 2012, MNRAS, 423, 862

Labbé, I., Bouwens, R., Illingworth, G. D., & Franx, M. 2006, ApJ, 649, L67

Labbé, I., González, V., Bouwens, R. J., et al. 2010, ApJ, 708, L26

Labbé, I., Oesch, P. A., Bouwens, R. J., et al. 2013, ApJl, 777, L19

Landsman, W. B. 1993, in Astronomical Society of the Pacific Conference Series, Vol. 52, Astronomical Data Analysis Software and Systems II, ed. R. J. Hanisch, R. J. V. Brissenden, & J. Barnes, 246

Lee, J. C., Kennicutt, R. C., Funes, José G., S. J., Sakai, S., & Akiyama, S. 2007, ApJ, 671, L113

Lee, J. C., Ly, C., Spitler, L., et al. 2012, PASP, 124, 782

Lehnert, M. D., Nesvadba, N. P. H., Le Tiran, L., et al. 2009, ApJ, 699, 1660

Leitherer, C., Tremonti, C. A., Heckman, T. M., & Calzetti, D. 2011, AJ, 141, 37

Lorenzoni, S., Bunker, A. J., Wilkins, S. M., et al. 2013, MNRAS, 429, 150

—. 2011, MNRAS, 414, 1455

Lowenthal, J. D., Hogan, C. J., Leach, R. W., Schmidt, G. D., & Foltz, C. B. 1990, ApJ, 357, 3

Ly, C., Lee, J. C., Dale, D. A., et al. 2011, ApJ, 726, 109

Madau, P. 1995, ApJ, 441, 18

Madau, P., Ferguson, H. C., Dickinson, M. E., et al. 1996, MNRAS, 283, 1388

Maiolino, R., Nagao, T., Grazian, A., et al. 2008, A&A, 488, 463

Malhotra, S., & Rhoads, J. E. 2004, ApJ, 617, L5

McCracken, H. J., Milvang-Jensen, B., Dunlop, J., et al. 2012, A&A, 544, A156

McGreer, I. D., Mesinger, A., & Fan, X. 2011, MNRAS, 415, 3237

McLean, I. S., Becklin, E. E., Bendiksen, O., et al. 1998, in Society of Photo-Optical Instrumentation Engineers (SPIE) Conference Series, Vol. 3354, Infrared Astronomical Instrumentation, ed. A. M. Fowler, 566–578

McLean, I. S., Steidel, C. C., Epps, H. W., et al. 2012, in Society of Photo-Optical Instrumentation Engineers (SPIE) Conference Series, Vol. 8446, Society of Photo-Optical Instrumentation Engineers (SPIE) Conference Series

McLinden, E. M., Finkelstein, S. L., Rhoads, J. E., et al. 2011, ApJ, 730, 136

McLure, R. J., Cirasuolo, M., Dunlop, J. S., Foucaud, S., & Almaini, O. 2009, MNRAS, 395, 2196

McLure, R. J., Dunlop, J. S., Cirasuolo, M., et al. 2010, MNRAS, 403, 960

McLure, R. J., Dunlop, J. S., de Ravel, L., et al. 2011, MNRAS, 418, 2074

McLure, R. J., Dunlop, J. S., Bowler, R. A. A., et al. 2013, MNRAS, 432, 2696

McQuinn, M., Furlanetto, S. R., Hernquist, L., Zahn, O., & Zaldarriaga, M. 2005, ApJ, 630, 643

McQuinn, M., Lidz, A., Zahn, O., et al. 2007, MNRAS, 377, 1043

McQuinn, M., Lidz, A., Zaldarriaga, M., Hernquist, L., & Dutta, S. 2008, MNRAS, 388, 1101

McQuinn, M., Oh, S. P., & Faucher-Giguère, C.-A. 2011, ApJ, 743, 82

Meiksin, A. 2006, MNRAS, 365, 807

Mesinger, A. 2010, MNRAS, 407, 1328

Meurer, G. R., Heckman, T. M., & Calzetti, D. 1999, ApJ, 521, 64

Miralda-Escudé, J., Haehnelt, M., & Rees, M. J. 2000, ApJ, 530, 1

Mortlock, D. J., Warren, S. J., Venemans, B. P., et al. 2011, Nature, 474, 616

Muñoz, J. A., & Loeb, A. 2011, ApJ, 729, 99

Neistein, E., & Dekel, A. 2008, MNRAS, 383, 615

Nestor, D. B., Shapley, A. E., Kornei, K. A., Steidel, C. C., & Siana, B. 2013, ApJ, 765, 47

Oesch, P. A., Stiavelli, M., Carollo, C. M., et al. 2007, ApJ, 671, 1212

Oesch, P. A., Bouwens, R. J., Illingworth, G. D., et al. 2010, ApJ, 709, L16

—. 2012, ApJ, 759, 135

—. 2013, ArXiv e-prints, arXiv:1309.2280

—. 2014, ApJ, 786, 108

Oke, J. B., & Gunn, J. E. 1983, ApJ, 266, 713

Oke, J. B., Cohen, J. G., Carr, M., et al. 1995, PASP, 107, 375

Ono, Y., Ouchi, M., Shimasaku, K., et al. 2010, ApJ, 724, 1524

Ono, Y., Ouchi, M., Mobasher, B., et al. 2012, ApJ, 744, 83

Ono, Y., Ouchi, M., Curtis-Lake, E., et al. 2013, ApJ, 777, 155

Ota, K., Walter, F., Ohta, K., et al. 2014, ArXiv e-prints, arXiv:1405.5387

Ouchi, M., Mobasher, B., Shimasaku, K., et al. 2009, ApJ, 706, 1136

Ouchi, M., Shimasaku, K., Furusawa, H., et al. 2010, ApJ, 723, 869

Ouchi, M., Ellis, R., Ono, Y., et al. 2013, ApJ, 778, 102

Papaderos, P., Izotov, Y. I., Fricke, K. J., Thuan, T. X., & Guseva, N. G. 1998, A&A, 338, 43

Papovich, C., Finkelstein, S. L., Ferguson, H. C., Lotz, J. M., & Giavalisco, M. 2011, MNRAS, 412, 1123

Parsons, A. R., Backer, D. C., Foster, G. S., et al. 2010, AJ, 139, 1468

Partridge, R. B. 1974, ApJ, 192, 241

Partridge, R. B., & Peebles, P. J. E. 1967, ApJ, 147, 868

Pawlik, A. H., Schaye, J., & van Scherpenzeel, E. 2009, MNRAS, 394, 1812

Pentericci, L., Fontana, A., Vanzella, E., et al. 2011, ApJ, 743, 132

Pentericci, L., Vanzella, E., Fontana, A., et al. 2014, ArXiv e-prints, arXiv:1403.5466

Penzias, A. A., & Wilson, R. W. 1965, ApJ, 142, 419

Pober, J. C., Parsons, A. R., Aguirre, J. E., et al. 2013, ApJ, 768, L36

Postman, M., Coe, D., Benítez, N., et al. 2012, ApJS, 199, 25

Pritchet, C. J., & Hartwick, F. D. A. 1987, ApJ, 320, 464

—. 1990, ApJ, 355, L11

Read, J. I., Pontzen, A. P., & Viel, M. 2006, MNRAS, 371, 885

Reddy, N. A., & Steidel, C. C. 2009, ApJ, 692, 778

Rees, M. J. 1968, ApJ, 153, L1

Retzlaff, J., Rosati, P., Dickinson, M., et al. 2010, A&A, 511, A50

Richard, J., Stark, D. P., Ellis, R. S., et al. 2008, ApJ, 685, 705

Richard, J., Smith, G. P., Kneib, J.-P., et al. 2010, MNRAS, 404, 325

Robertson, B. E. 2010a, ApJ, 716, L229

—. 2010b, ApJ, 713, 1266

Robertson, B. E., Ellis, R. S., Dunlop, J. S., McLure, R. J., & Stark, D. P. 2010, Nature, 468, 49

Robertson, B. E., Furlanetto, S. R., Schneider, E., et al. 2013, ApJ, 768, 71

Rogers, A. B., McLure, R. J., & Dunlop, J. S. 2013, MNRAS, 429, 2456

Salpeter, E. E. 1955, ApJ, 121, 161

Santini, P., Fontana, A., Grazian, A., et al. 2009, A&A, 504, 751

Santos, M. R. 2004, MNRAS, 349, 1137

Sargent, W. L. W., & Searle, L. 1970, ApJl, 162, L155

Schaerer, D., & de Barros, S. 2009, A&A, 502, 423

—. 2010, A&A, 515, A73

Schechter, P. 1976, ApJ, 203, 297

Schenker, M. A., Ellis, R. S., Konidaris, N. P., & Stark, D. P. 2013a, ApJ, 777, 67

Schenker, M. A., Stark, D. P., Ellis, R. S., et al. 2012, ApJ, 744, 179

Schenker, M. A., Robertson, B. E., Ellis, R. S., et al. 2013b, ApJ, 768, 196

Schiminovich, D., Ilbert, O., Arnouts, S., et al. 2005, ApJ, 619, L47

Schmidt, K. B., Treu, T., Brammer, G. B., et al. 2014, ApJ, 782, L36

Schmidt, M. 1965, ApJ, 141, 1295

Shapley, A. E., Steidel, C. C., Pettini, M., & Adelberger, K. L. 2003, ApJ, 588, 65

Shim, H., Chary, R.-R., Dickinson, M., et al. 2011, ApJ, 738, 69

Siana, B., Teplitz, H. I., Ferguson, H. C., et al. 2010, ApJ, 723, 241

Smit, R., Bouwens, R. J., Labbé, I., et al. 2014, ApJ, 784, 58

Songaila, A., Hu, E. M., Cowie, L. L., & McMahon, R. G. 1999, ApJ, 525, L5

Stanway, E. R., Bunker, A. J., McMahon, R. G., et al. 2004, ApJ, 607, 704

Stark, D. P., Bunker, A. J., Ellis, R. S., Eyles, L. P., & Lacy, M. 2007, ApJ, 659, 84

Stark, D. P., Ellis, R. S., Bunker, A., et al. 2009, ApJ, 697, 1493

Stark, D. P., Ellis, R. S., Chiu, K., Ouchi, M., & Bunker, A. 2010, MNRAS, 408, 1628

Stark, D. P., Ellis, R. S., Jones, T. A., & Schenker, M. A. in prep.

Stark, D. P., Ellis, R. S., & Ouchi, M. 2011, ApJl, 728, L2

Stark, D. P., Schenker, M. A., Ellis, R., et al. 2013a, ApJ, 763, 129

Stark, D. P., Auger, M., Belokurov, V., et al. 2013b, MNRAS, 436, 1040

Steidel, C. C., Adelberger, K. L., Giavalisco, M., Dickinson, M., & Pettini, M. 1999, ApJ, 519, 1

Steidel, C. C., Erb, D. K., Shapley, A. E., et al. 2010, ApJ, 717, 289

Steidel, C. C., Giavalisco, M., Pettini, M., Dickinson, M., & Adelberger, K. L. 1996, ApJ, 462, L17

Steidel, C. C., Pettini, M., & Hamilton, D. 1995, AJ, 110, 2519

Steidel, C. C., & Sargent, W. L. W. 1987, ApJ, 318, L11

Tacchella, S., Trenti, M., & Carollo, C. M. 2013, ApJ, 768, L37

Taniguchi, Y., Shioya, Y., & Trump, J. R. 2010, ApJ, 724, 1480

Tilvi, V., Papovich, C., Finkelstein, S. L., et al. 2014, ArXiv e-prints, arXiv:1405.4869

Tingay, S., Goeke, R., Hewitt, J. N., et al. 2012, in Resolving The Sky - Radio Interferometry: Past, Present and Future

Tinker, J., Kravtsov, A. V., Klypin, A., et al. 2008, ApJ, 688, 709

Tinker, J. L., Robertson, B. E., Kravtsov, A. V., et al. 2010, ApJ, 724, 878

Tinsley, B. M. 1980, ApJ, 241, 41

Trenti, M., Stiavelli, M., Bouwens, R. J., et al. 2010, ApJ, 714, L202

Trenti, M., Bradley, L. D., Stiavelli, M., et al. 2011, ApJ, 727, L39

Treu, T., Schmidt, K. B., Trenti, M., Bradley, L. D., & Stiavelli, M. 2013, ApJl, 775, L29

Treu, T., Trenti, M., Stiavelli, M., Auger, M. W., & Bradley, L. D. 2012, ApJ, 747, 27

Trump, J. R., Weiner, B. J., Scarlata, C., et al. 2011, ApJ, 743, 144

Tyson, J. A. 1988, AJ, 96, 1

Vanzella, E., Giavalisco, M., Dickinson, M., et al. 2009, ApJ, 695, 1163

Vanzella, E., Pentericci, L., Fontana, A., et al. 2011, ApJ, 730, L35

Verhamme, A., Schaerer, D., Atek, H., & Tapken, C. 2008, A&A, 491, 89

Verhamme, A., Schaerer, D., & Maselli, A. 2006, A&A, 460, 397

Wang, W.-H., Cowie, L. L., Barger, A. J., Keenan, R. C., & Ting, H.-C. 2010, ApJs, 187, 251

Webb, J. K., Barcons, X., Carswell, R. F., & Parnell, H. C. 1992, MNRAS, 255, 319

Weinmann, S. M., Neistein, E., & Dekel, A. 2011, MNRAS, 417, 2737

Wilkins, S. M., Bunker, A. J., Ellis, R. S., et al. 2010, MNRAS, 403, 938

Wilkins, S. M., Bunker, A. J., Lorenzoni, S., & Caruana, J. 2011, MNRAS, 411, 23

Windhorst, R. A., Cohen, S. H., Hathi, N. P., et al. 2011, ApJS, 193, 27

Wyithe, J. S. B., & Loeb, A. 2006, Nature, 441, 322

Yan, H., Yan, L., Zamojski, M. A., et al. 2011, ApJ, 728, L22

Yan, H.-J., Windhorst, R. A., Hathi, N. P., et al. 2010, Research in Astronomy and Astrophysics, 10, 867

Yatawatta, S., de Bruyn, A. G., Brentjens, M. A., et al. 2013, A&A, 550, A136

Zahn, O., Reichardt, C. L., Shaw, L., et al. 2012, ApJ, 756, 65

Zaldarriaga, M., Colombo, L., Komatsu, E., et al. 2009, in American Institute of Physics Conference Series, Vol. 1141, American Institute of Physics Conference Series, ed. S. Dodelson, D. Baumann, A. Cooray, J. Dunkley, A. Fraisse, M. G. Jackson, A. Kogut, L. Krauss, M. Zaldarriaga, & K. Smith, 179–221